UCC

University College Cork, Ireland
Coláiste na hOllscoile Corcaigh

Ollscoil na hÉireann,

National University of Ireland

Manipulation of magnetic anisotropy in nanostructures

A thesis undertaken

at the

Tyndall National Institute

And presented to the

National University of Ireland,

University College Cork

In partial fulfillment of the

requirements for the degree of **Doctor of Philosophy (PhD)**

by

Tuhin Subhra Maity BSc, MSc.

Supervisor: Dr. Saibal Roy

Co-Supervisor: Prof. John McInerney

2015

Contents

I dedicate this work,

to my wonderful parents Narayan and Anima Maity

and to my teachers.

Acknowledgements

After working for four years on this project I would like to take this opportunity to express my gratitude to several individuals. Firstly I would like to thank my supervisor Dr. Saibal Roy for giving me the opportunity to undertake a PhD programme of study in Tyndall National Institute and for his constant guidance in four years of this project. I am so deeply grateful for his encouragement, professionalism, valuable advice and financial support throughout this project and my entire program of study. I am also thankful to my co-supervisor Prof. John McInerney for his valuable inputs. I would like to appreciate whole heartedly the help and initial training I received from Dr. Sunphu Li, Dr. Brice Jamieson, Dr. Santosh Kulkarni and Dr. Jeffrey F. Godsell. I would like to sincerely express my gratitude to Dhiman Mallick, Pranay Poddar and other group members for their help and encouragement. I would like to thank our collaborators Dr. Tandra Ghoshal (UCC), Dr. Sudipta Goswami (CGCRI-India), Dr. Dipten Bhattacharya (CGCRI-India), Prof M. A. Morris (UCC), Prof. Quentin Ramasse (SuperSTEM, UK) and Dr. Lynette Kenney (Tyndall). I thank them all for their support, advice, inputs and encouragements.

I would also like to acknowledge Dr. Peter Parbrook as the mentor of this thesis, and I am gratefully indebted to him for his very valuable comments on this thesis.

I wish a big thank to Cristina Agualusa, Preethi Balaji, Gangotri Dey, Anjana Kulkarni, Ricky Anthony, Nitin Deepak, Yasin Mamat, Natascia Lamparelli, Smita Thakur, Shatabdi Choudhury, Anjena Daswani, Bishwamitra Thakur, Subhajit Biswas, Romika Saini and other friends in Cork for their support over the years.

Finally, I must express my very profound gratitude to my parents and family for providing me with unfailing support and continuous encouragement throughout my years of study and through the process of researching and writing this thesis. This accomplishment would not have been possible without them.

<div align="right">Thank you.</div>

<div align="center">ধন্যবাদ</div>

List of figures

List of tables

Decleration

I, Tuhin Maity, declare that the thesis titled 'Manipulation of magnetic anisotropy in nanostructures' and the work presented in it are my own work for the dissertation purpose. I further confirm that:

- ❖ This work was done entirely by me for a research degree at the University.
- ❖ Any part of this thesis has previously not been submitted for a degree or any other qualification at this University or any other institution, if there is any overlap that has been clearly stated.
- ❖ Where I have consulted the published work of others, is clearly attributed with proper references.
- ❖ Where I have quoted from the work of others, the source is always given.
- ❖ With the exception of such quotations, this thesis is entirely my own work.
- ❖ I have acknowledged all main sources of help.
- ❖ Where the thesis is based on work done by myself jointly with others, I have made clear exactly what was done by others and what I have contributed myself.
- ❖ Most parts of this work have been published as several international journal papers.

Signature

Date:

Abstract

The magnetic properties of micro/nano-structure have attracted intense research interest in relation to geometrically-induced magnetism to delineate fundamental magnetic phenomena as well as focus the technological aspects in areas such as magnetic sensors, storage devices, integrated inductive components and a number of novel magnetic devices. Depending on the device applications, materials with high, medium or low magnetic anisotropy and their potential manipulation are required. The elements like geometry, crystal structure, magnetic spin configuration at the surfaces and interfaces are the basic ingredients for this manipulation. The most dramatic manifestation in this respect is the chance to manipulate the magnetic anisotropy over the intrinsic preferential direction of the magnetization, commonly observed in all ferromagnetic materials, thus opening up further possibility and functionality of ferromagnetic materials for device applications.

In this thesis various types of magnetic anisotropy of different nanostructured materials and their manipulation are investigated. As a first approach detailed experimental and analytical methods for the qualitative and quantitative determination of magnetic anisotropy in nanomodulated $Ni_{45}Fe_{55}$ thin film are studied. In-plane magnetic field rotations in modulated $Ni_{45}Fe_{55}$ revealed various rotational symmetries of magnetic anisotropy due to dipolar interaction with a crossover from lower to higher fold as a function of modulation geometry. The tendency to form vortex is in fact found to be very small, which highlights that the strong coupling between metastable dipoles is more favorable than vortex formation to minimize energy in this nanomodulated structure. Derived mathematical expressions based on magnetic dipolar interaction and results obtained from Object Oriented Micromagnetic Framework (OOMMF) simulation are found to be in good agreement with our results.

Further a second approach was investigated to control exchange anisotropy mostly known as excahneg bias at ferromagnetic (FM) – aniferomagnetic (AFM) interface in multifferoic nanocomposite materials where two different phase/types of materials have been simultaneously synthesized. Apart from the strong multiferroic coupling at room temperature, $BiFeO_3$, with a long wavelength (~62 nm) cycloidal magnetic structure and

canted antiferromagnetism, exhibits an additional functionality of switching the magnetic anisotropy of a ferromagnetic layer via exchange bias coupling in a $BiFeO_3$ antiferromagnetic – $Bi_2Fe_4O_9$ ferromagnetic layer composite. The switching can be triggered both by a magnetic as well as an electric field because of strong multiferroicity. Magnetic field, temperature and measurement protocol dependence of magnetic anisotropy of nanoscale multiferroic materials are presented.

The third parallel aspect of this work was to electroplate thin films of metal alloy nanocomposite for enhanced exchange anisotropy. In this work an unique observation of positive (anti clock wise) and negative (clock wise) hysteresis loop formation in the Ni,Fe solid solution with very low coercivity and large positive exchange anisotropy/exchange bias are investigated. These two opposite (positive/negative) hysteresis loop formation occur depending upon the field range used in hysteresis loop measurement and thus can potentially be manipulated. Hence, controllable positive and negative exchange bias is observed which has high potential application such as in MRAM devices.

In this thesis, the current state of the art has been described in **_chapter one._** In **_chapter two_** a broad literature review on the area of research has been reviewed.

Different experimental techniques used in this work are discussed in details in **_chapter three_**.

Micromagnetic simulation has been carried out to understand further the mechanism of magnetic materials. This has been discussed in **_chapter four_**.

In **_chapter five_** the magnetic anisotropy control by 3D nanomodulation including how to avoid vortex formation in a continuous film are discussed.

Chapter six introduces giant exchange anisotropy in multiferroic nanocomposite ($BiFeO_3$-$Bi_2Fe_4O_9$) including the effect of temperature and magnetic field on it.

Chapter seven examines how the exchange anisotropy can be used to manipulate hysteresis loop direction in alloy composites with low coercivity (H_C).

Chapter eight concludes with the summary of the key findings of the study, potential application of them and possible future scope of the present research.

List of Publications

Journal Papers

Published in 2015

1.   Reply to the comment on "Superspin glass mediated giant spontaneous exchange bias in a nanocomposite of $BiFeO_3$-$Bi_2Fe_4O_9$"
Tuhin Maity, Sudipta Goswami, Dipten Bhattacharya, and Saibal Roy
Physical Review Letter 114 (9), 099704 (2015)

Published in 2014

2.   "Large Magnetoelectric Coupling in Nanoscale $BiFeO_3$ from Direct Electrical Measurements"
Sudipta Goswami, Dipten Bhattacharya, Lynette Keeney, Tuhin Maity, S.D. Kaushik, V. Siruguri, Gopes C. Das, Haifang Yang, Wuxia Li, C.-Z. Gu, M.E. Pemble, and Saibal Roy
Physical Review B 90 (10), 104402 (2014)

3.   "Origin of the asymmetric exchange bias in $BiFeO_3$/$Bi_2Fe_4O_9$ nanocomposite"
Tuhin Maity, Sudipta Goswami, Dipten Bhattacharya, and Saibal Roy
Physical Review B 89 (14), 1404112014 (2014)

Published in 2013

4.   "Size and space controlled hexagonal arrays of superparamagnetic iron oxide nanodots: magnetic studies and application"
T Ghoshal, T Maity, R Senthamaraikannan, MT Shaw, P Carolan, Justin D Holmes, Saibal Roy, Michael A Morris
Scientific Reports 3, 2013

5.   "Magnetic Field-Induced Ferroelectric Switching in Multiferroic Aurivillius Phase Thin Films at Room Temperature"
L Keeney, T Maity, M Schmidt, A Amann, N Deepak, N Petkov, S Roy, Martyn E Pemble, Roger W Whatmore
Journal of the American Ceramic Society 96 (8), 2339-2357, 2013 (Feature article)

6.   ''Superspin glass mediated giant spontaneous exchange bias in a nanocomposite of BiFeO3- Bi2Fe4O9''
T Maity, S Goswami, D Bhattacharya, S Roy
Physical Review Letter 110, 107201 (2013)

7.   ''Spontaneous exchange bias in a nanocomposite of $BiFeO_3$-$Bi_2Fe_4O_9$''
T Maity, S Goswami, G C Das, D Bhattacharya, S Roy
Journal of Applied Physics 113, (2013)

8.   ''Ordered magnetic dipoles: Controlling anisotropy in nanomodulated continuous ferromagnetic films''
Tuhin Maity, Shunpu Li, Lynette Keeney, Saibal Roy,
Physical Review B 86 (024438), 7(2012)

9.   ''Large Scale Monodisperse Hexagonal Arrays of Superparamagnetic Iron Oxides Nanodots: A Facile Block Copolymer Inclusion Method''
T Ghoshal, T Maity, JF Godsell, S Roy, MA Morris
Advanced Materials 5 (2012)

Book Chapters:

10.   "Nanostructured Magnetic Materials for High-Frequency Applications - Beyond-CMOS Nanodevices 1, 457-483"
S. Roy, J. Godsell and T. Maity
Wiley Publication 2014

11.   "Novel approaches for genuine single phase room temperature magnetoelectric multiferroics"
Lynette Keeney, Michael Schmidt, Andreas Amann, Tuhin Maity, Nitin Deepak, Ahmad Faraz, Nikolay Petkov, Saibal Roy, Martyn E. Pemble and Roger W. Whatmore
Wiley Publication 2014 (In press)

Journal papers from Master's Programme (from previous Institutes)

12.   ''Structural, magnetic and electric properties of $HoMnO_3$ films on $SrTiO_3$(001)''
R Wunderlich, C Chiliotte, G Bridoux, T Maity, Ö Kocabiyik, A Setzer, M .
Journal of Magnetism and Magnetic Materials 324 (4), 460-465(2012)

13.   ''Observation of Enhanced Dielectric Coupling and Room Temperature Ferromagnetism in Chemically Synthesized $BiFeO_3$@ SiO_2 Core–shell Particles''
MM Shirolkar, R Das, T Maity, P Poddar, SK Kulkarni
The Journal of Physical Chemistry C1(2012)

14. ''Dielectric and spin relaxation behaviour in $DyFeO_3$ nanocrystals''
A Jaiswal, R Das, T Maity, P Poddar
Journal of Applied Physics 110 (12), 124301-124301-7(2011)

15. ''Investigations of magnetic and dielectric properties of cupric oxide nanoparticles''
RS Bhalerao-Panajkar, MM Shirolkar, R Das, T Maity, P Poddar, SK Kulkarni
Solid State Communications 5(2010)

16. ''Temperature-Dependent Raman and Dielectric Spectroscopy of $BiFeO_3$ Nanoparticles: Signatures of Spin-Phonon and Magnetoelectric Coupling''
A Jaiswal, R Das, T Maity, K Vivekanand, S Adyanthaya, P Poddar
The Journal of Physical Chemistry C 9(2010)

17. ''Magnetic and dielectric properties and Raman spectroscopy of $GdCrO_3$ nanoparticles''
A Jaiswal, R Das, K Vivekanand, T Maity, PM Abraham, S Adyanthaya, P Poddar
Journal of Applied Physics 107 (1), 013912-013912-7 11(2010)

International Peer Reviewed Conference Proceedings

Presented in 2013

18. Super spin mediated giant exchange bias in multiferroic nanocomposite
Tuhin Maity, Sudipta Goswami, Dipten Bhattacharya and Saibal Roy
JEMS 2014, Rhodos, Greece

19. ''Observation of tunable magnetic dipoles by MFM in nanomodulated continuous ferromagnetic film''
Tuhin Maity, Saibal Roy
IEEE MMM/Intermag 2013, Chicago, 2013

20. ''Synthesis and Multiferroic Investigations of Bi7Ti3Fe2.1Mn0.9O15 Aurivillius Phase Thin Films''
Lynette Keeney, Tuhin Maity, Michael Schmidt, Nitin Deepak, Saibal Roy, Martyn E. Pemble, Roger W. Whatmore, COST MPO904 Action / IEEE-ROMSC Iasi, Romania, 24 Sept 2012.

21.　''Synthesis and Multiferroic Investigations of Bi $_{m+1}$Ti$_3$Fe $_{m-3}$O $_{3m+1}$ Aurivillius Phase Thin Films where m ≥ 6''
Lynette Keeney, Tuhin Maity, Michael Schmidt, Nitin Deepak, Saibal Roy, Martyn E. Pemble, Roger W. Whatmore, ISAF-ECAPD-PFM- 2012 – Aveiro, Portugal, 11 July 2012.

22.　''Multiferroic (ferroelectric/ferromagnetic) behaviour of Aurivillius Phase Thin Films''
Roger W. Whatmore, Lynette Keeney, Tuhin Maity, Michael Schmidt, Nitin Deepak, Saibal Roy, Andreas Amann, Nikolay Petkov, Martyn E. Pemble, Electronic Materials and Applications 2013, January 23 - 25, 2013, Orlando, Florida

　　　Presented in 2012

23.　''A facile block copolymer inclusion technique for large scale monodisperse hexagonal arrays of superparamagnetic iron oxides nanodots''
T Ghoshal, T Maity, JF Godsell, S Roy, MA Morris Nanotechnology 2012 1, 128 - 131(2012) ISBN:978-1-4665-6274-5 CRC Press Taylor & Francis

24.　''Symmetry of magnetic dipole controlled anisotropy in nanomodulated thin ferromagnetic film''
Tuhin Maity, Shunpu Li, Saibal Roy
IEEE INTERMAG 2012, Vancuver, Canada

25.　''Symmetry of magnetic anisotropy in 3D nanomodulated continuous thin ferromagnetic film''
Tuhin Maity, Shunpu Li, Saibal Roy
ICSM 2012, Istanbul, Turkey

　　　Presented in 2011

26.　''Symmetry of magnetic anisotropy in nanomodulated thin ferromagnetic film''
Tuhin Maity, Shunpu Li, Saibal Roy
Syncroton User Meeting 2011, Oxford, UK

Units

The subject of the thesis is widely based on different magnetic materials and different magnetic measurements. Different unit systems are used to study magnetism in recent times, they are mainly International System/System International d'Unites (SI) or meter-kilogram-second system (MKS) and Gaussian system or centimeter-gram-second or electromagnetic system (CGS). The CGS system is commonly used in the USA and Asian countries whereas SI system is widely used in Europe. Both the systems define same phenomenon but visualizing in different way or obtained by different measurement technique and presented in different units. Same occurrence can be converted from one unit system to another by simple conversion factor. Some of the principle magnetic properties in the two unit systems used in this thesis with their conversion factor are presented in Table 1.

Table 1: CGS and SI magnetic unit conversion table.

No	Quantity	Symbol	Gaussian/cgs	Conversion factor	SI & mks
1	Magnetic flux density	B	gauss (G)	10^{-4}	tesla (T)
2	Magnetic field strength	H	oersted (Oe)	$10^3/4\pi$	ampere (A)
3	Magnetization (vol.)	M	emu/cm^3	10^3	A/m
4	Magnetization (vol.)	$4\pi M$	emu/cm^3	$10^3/4\pi$	A/m
5	Magnetization (mass)	σ, M	emu/g	$4\pi \times 10^{-7}$	Wb.m/kg
6	Magnetic moment	m	emu, erg/G	10^{-3}	A.m2
7	Magnetic dipole moment	j	emu, erg/G	$4\pi \times 10^{-7}$	Wb.m
8	Susceptibility (mass)	χ	emu/g	$(4\pi)^2 \times 10^{-10}$	H.m^2/kg
9	Permeability	μ	dimensionless	$4\pi \times 10^{-7}$	H/m
10	Relative permeability	μ_r	undefined		dimensionless
11	Demagnetization factor	D,N	dimensionless	$1/4\pi$	dimensionless

1. Chapter – Introduction

1.1. Background

The magnetic properties of micro/nano-structured materials have attracted intense research interest from the viewpoints of geometrically-induced magnetism to delinate fundamental magnetic phenomena and also from the technological point of view in areas such as magnetic sensors, storage devices, integrated inductive components and a number of magnetic devices for novel applications. It is a well-known experimental fact that ferromagnetic material exhibits 'easy' and 'hard' directions of the magnetization depending on magnetic spin configuration for energy minimization. For the technological application this magnetic anisotropy becomes one of the most important properties of magnetic materials. The enormous research on magnetic properties of nanostructures has been the thrust in recent years behind the fundamental understanding of the magnetic anisotropy and its application in micromagnetic devices. For advanced device applications, materials with tuneable anisotropy are more useful.

A preferred magnetic moment orientation in nanostructured material can be quite different in terms of the factors that account for the easy-axis alignment in bulk material, and consequently the anisotropy strength can also be significantly different. The influence of the elements like geometry, crystal structure, magnetic spin configuration at the materials interfaces and surfaces, are the basic ingredients for this behavior. By varying the suitable parameters and choosing appropriate materials, it is possible to tailor the magnetic anisotropy. The most dramatic manifestation in this respect could be the chance to manipulate the magnetic anisotropy over the intrinsic preferential direction of the magnetization as commonly observed in all ferromagnetic thin films which can open up new window of functionality of ferromagnetic materials for device applications.

Different type of magnetic anisotropy of magnetic nanostructured thin films and their manipulation is discussed in this thesis. Magnetocrystalline, dipolar (shape), magnetoelastic and exchange anisotropies are explained. Detailed experimental and analytical methods for the quantitative and qualitative determination of various magnetic anisotropies are described. Many experimental results are further investigated by Object Oriented Micromagnetic Framework (OOMMF) simulation. Magnetic field, temperature

and measurement protocol dependence of magnetic anisotropy of nanoscale materials are presented. It is shown that geometry of nanostructures, material interface and selection of materials play important role to determine the magnetic anisotropy.

1.2.   Motivation of the work

The interest in nanostructured magnetic materials has experienced a tremendous boost for potential use in numerous present and future device applications such as sensors, actuators, magnetic data storage and integrated passive devices due to the tunable magnetic properties and simultaneous improvement in material preparation technique. Following the unavoidable trend of device miniaturization, the present research trend is focused on various ways to reduce the size of every aspect of integrated circuits and integrated magnetic components.   In all such applications the key property of ferromagnetic materials is the direction of its magnetization which is widely based on magnetic anisotropy. This is the property which determines the preferred easy or hard magnetization directions of magnetic domains at remanence state and also decides the magnetization reversal process in presence of external field.

1.3.   Defining the scope of the Thesis

A number of novel magnetic materials have been investigated to find out new possibilities to control and enhance magnetic anisotropy for next generation device applications. A unique nanopatterned soft magnetic thin film was investigated for possible magnetic anisotropy (shape/dipole) control. The goal of the work is to investigate a unique low cost solution to control magnetic anisotropy for device applications.

The magnetic anisotropy has been distinguished depending on its origin. The crystalline anisotropy or magnetoelastic anisotropy is intrinsic in nature and originates due to spin–orbit coupling (SOC) depending on crystalline structure of the materials. For polycrystalline materials, the overall magnetic anisotropy is of dipolar origin and largely

originates from the shape and known as shape anisotropy. In the present desertation work magnetic anisotropy of polycrystalline nanomodulated $Ni_{45}Fe_{55}$ films have been studied as a function of modulation geometry. In plane magnetic field rotations revealed a rotational symmetry of magnetization in a unique nanomodulated structure. We found a systematic crossover from lower folds to higher folds of magnetic symmetry in nanomodulated continuous film depending upon the modulation parameters. It is argued that this complex rotational symmetry can be introduced and controlled by proper 3-dimentional modulation having a particular geometrical symmetry. Analytical expression for the angular dependence of the magnetization was obtained to validate the experimental results. The overall discussion is focused on the effect of 3-dimensional geometry on magnetic property of a ferromagnetic thin film. The nanomodulation technique used in this work is cost effective. A further investigation in this work was how to avoid magnetic vortex formation in nano-patterned ferromagnetic material. The existence of both in plane and out of plane dipoles in this 3D nanomodulation film and their competition resulting into a metastable state don't allow vortex formation (the minimum energy state). This is an essential requirement for nanostrcutured ferromagnetic materials in memory device application.

A second approach in a novel technique was employed to control exchange anisotropy mostly known as exchange bias at ferromagnetic (FM) – aniferomagnetic (AFM) interface showing for the first time its tuneability in multiferroic nanocomposite materials where two different phase/types of materials can be simultaneously synthesized. Apart from the strong multiferroic coupling at room temperature, $BiFeO_3$, with a long wavelength (~62 nm) cycloidal magnetic structure and canted antiferromagnetism, exhibits an additional functionality of switching the magnetic anisotropy of a ferromagnetic layer via exchange bias coupling in a $BiFeO_3$ antiferromagnetic – $Bi_2Fe_4O_9$ ferromagnetic layer composite. We have shown that the switching can be triggered both by a magnetic as well as an electric field because of strong multiferroicity present in the system. The role of exchange bias coupling has been noted not just in a single crystal $BiFeO_3$-ferromagnetic layer system but in other thin film based heterostructures as well. Whether the exchange bias is larger in thin film or in bulk $BiFeO_3$ based bilayer systems is debatable. While the exchange bias in thin films and nanoscale systems originates from uncompensated cycloid of the magnetic

structure, larger canting angle offers significant exchange bias even in bulk $BiFeO_3$ based systems.

The third parallel aspect of this work was to study the electroplated thin films of metal alloy nanocomposite for enhanced exchange bias. In this work we described direct observation of positive (anti clock wise) and negative (clock wise) hysteresis loop formation in the Ni,Fe solid solution with very low coercivity and large positive exchange anisotropy/exchange bias. These two opposite (positive/negative) hysteresis loop originated depending upon the field range of hysteresis loop measurement. Like most other positive exchange bias system $Ni_{45}Fe_{55}$ shows positive shift at field direction when the loop tracing field range is relatively small (just above the saturation field) and the loop is positive. However, when the film is measured with a higher loop tracing field range, we observed a typical negative hysteresis loop with no exchange bias. The main interest here was to achieve high exchange bias for materials with very low coercivity and low saturation magnetic field and trigger the hysteresis loop direction. The importance of this study lays in the essence on high exchange anisotropic materials for cutting edge technologies.

1.4. Summary and Thesis Layout

In this thesis at first the current state of the art in chapter two a broad literature review of the area of research has been reviewed. In chapter three different experimental techniques used in the work are discussed in details. Micromagnetic simulation has been performed to understand further the mechanism of magnetic materials. This has been introduced in chapter four. In chapter five, the magnetic anisotropy control by 3D nanomodulation and how to avoid vortex formation are discussed. Chapter six introduces giant exchange bias in multiferroic nanocomposite ($BiFeO_3$-$Bi_2Fe_4O_9$) and the effect of temperature and magnetic field on it. Chapter seven examines how the exchange bias can be used to manipulated hysteresis loop direction in alloy composite with low coercivity (H_C). Chapter eight concludes with the summary of the key findings of the study, potential applications of them and possible future scope of the research.

2. Chapter – State of the Art Review

2.1. Introduction

In this chapter the state of the art in current research on magnetic anisotropy control in different ferromagnetic materials is discussed. Magnetic anisotropy in general is a fundamental property of magnetic materials. The magnetization tends to lie in a preferred direction to obtain lowest magneto-static energy state. The energy includes an anisotropy term $E_a(\theta,\varphi)$ where the direction of magnetization is defined by the angular coordinates θ and φ. The anisotropy can be intrinsic, related to atomic scale interactions in a unit cell which define easy directions in the crystal structure called magnetocrystalline anisotropy. It can also be related to the energy of the sample in its own demagnetizing field due to the sample geometry called shape/dipolar anisotropy. Exchange bias or exchange anisotropy occurs due to magnetic interaction between layers of magnetic materials where the strong magnetic coupling of an antiferromagnetic thin film causes a shift in the magnetic loop of soft magnetization of a ferromagnetic film. Magnetic anisotropy is one of the very important parameters in relation to the characterization of materials which is widely used in different technological applications, particularly magnetic recording media, sensors, magnetic passive devises, etc. The enormous research on magnetic anisotropy of ultrathin films and nanostructures opens up new horizon in terms of fundamental understanding as well. This chapter includes fundamental theory of different magnetic anisotropy and recent developments in this field.

A vast number of magnetic devices are employed in the present day electronic industry. In ancient time the magnetic phenomenon in human beings were experienced by utilizing natural iron minerals. In modern times this was understood and explained from the standpoint of electromagnetics, to which many physicists such as Oersted and Faraday made a great contribution. In 1822 Ampère explained magnetic materials based on a small circular electric current which was the first explanation of a molecular magnet. Later, Ampère's circuital law introduced the concept of a magnetic moment or magnetic dipoles. The magnetic field generated by an electrical field is given by Ampère's circuital law as

$$\oint H.dl = I$$

Where the total current (I), is equal to the line integral of the magnetic field (H) around a closed path containing the current. Whereas, in the materials the origins of the magnetic moment and it's magnetic field are the electrons in atoms comprising the materials. The response of materials to an external magnetic field is relevant to magnetic energy expressed as (in CGS)

$$E = -m.H$$

In SI unit

$$E = -\mu_0 m.H$$

where μ_0 is the magnetic permeability of free space.

The magnetization M is a property of the material which depends on the individual magnetic moments of its constituent magnetic origins. The magnetization of the material reflects the magnetic interaction at a microscopic molecular level which results in experimental behaviors due to external parameters such as temperature and magnetic field. Magnetic induction (B) is a magnetic response of the material when it is placed in an external magnetic field (H). The relationship between B and H is expressed as (in CGS)

$$B = H + 4\pi M$$

In SI units the relationship is given using the permeability of free space (μ_0) as

$$B = \mu_0(H + M)$$

The magnetic properties are measured as a direct magnetization response to the applied magnetic field and the ratio of M to H expressed by magnetic susceptibility χ.

$$\chi = M/H$$

The magnetization M of ordinary materials exhibits a linear function $M = \chi H$ with external magnetic field H. Material shows either positive or negative magnetic susceptibility, i.e. $\chi > 0$ or $\chi < 0$. In the case of $\chi > 0$ the material is called as Paramagnetic and in the case of $\chi < 0$ it's known as diamagnetic material. In the M − H curve this behavior is discriminated as a positive or negative MH slope, as shown in Figure 2.1. Usually, a diamagnetic response toward an external magnetic field is very minor and the slope is very small compared to the slope of paramagnetic material.
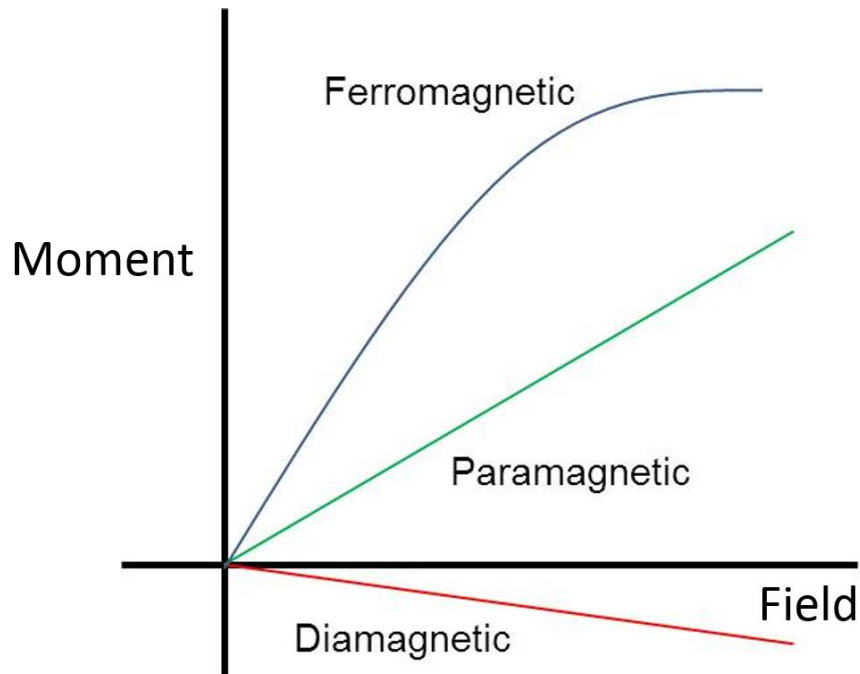
Fig.2.1. Schematic representation of typical field dependence of magnetization for particular type of magnetic materials.

Paramagnetic materials sometimes experience magnetic phase transitions due to orderings of magnetic moments which occur through exchange and dipolar interactions between them as a function of temperature. There exist several ordering patterns which specify the vector arrangement of magnetic moments in different kind of materials. Parallel and antiparallel orientations are called ferromagnetism andantiferromagnetism respectively.
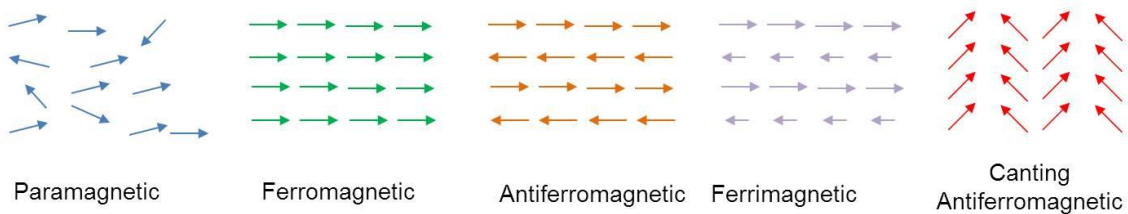
Fig.2.2. Disordered and ordered states of magnetic moments for different magnetic materials

In ferromagnetic materials magnetization (M) curve under a magnetic field cycle after the magnetic field is applied to reach a certain high value, the field is reduced to zero, and then it is reversed in field direction, making a loop. The magnetization (M), is traced out versus

external applied field H, as shown in Figure 2.1, and is called a "hysteresis curve". The initial increase of the magnetization starts at the origin and it reaches a maximum value called saturation magnetization, $M_s = N_{gJ}\mu_B J$. In the reverse process of the field the magnetization does not trall back to the original curve, but remains at a certain value of magnetization at H = 0. This is called the remanenence magnetization which corresponds to spontaneous magnetization of the material. The residual magnetization gradually decreased due to reversed magnetic field and finally makes the magnetization zero at certain field, H = H_C, which is called the "coercivity" or " coercive force " for the material at that temperature. The hysteresis loop is a complete illustration of the magnetic moment after a cyclic application of the external magnetic field. The important parameters in the evaluation of hysteresis loop for the ferromagnetic materials consist of these three values, M_S, M_r, and H_C. Every combination of these materials parameters are useful for device applications depending on the various aims. For example, large remanence (M_r) means a strong magnet, and the coercivity (H_C) determines the materials as either soft or hard magnets. A soft magnet is likely to be magnetized easily and is also easily demagnetized, whereas a hard magnetic material needs more field to be magnetized and reach magnetically saturated state. Even in the same sample it's possible that in one direction it's easier to magnetize compared to other direction which is called magnetic anisotropy.

Ferromagnetic materials are most widely used material among all. The phenomenon of ferromagnetism originates from interactions of neighboring spins. While the spin interaction is complicated, the ferromagnetic moment can be considered as result from a quasi-paramagnetic response to a huge internal field called Weiss molecular field (H_w). According to Weiss theory, H_w is proportional to the magnetization of the material, i.e.

$H_w = \beta M$ Equation 2.1

The total magnetic field that the material experiences is:

$H_{tot} = H + H_w = H + \beta M$ Equation 2.2

where β is the constant of proportionality, H is the external field.

By analogy to paramagnetism, we can substitute x = $\mu_o m_b (H_{tot}) / kT$ for H in the Langevin function and write:

$$\frac{M}{M_S} = \mathcal{L}\left(\frac{\mu_0 m_b (H + \beta M)}{KT}\right)$$ Equation 2.3

For temperatures above the Curie temperature (T_c) by definition no internal field is zero, hence βM is zero. Substituting Nm_b/v for M_S, and using the low-field approximation for L(a), we can write

$$\frac{M}{H} = \frac{\mu_0\,Nm_b^2}{v^3K(T-T_C)} = \chi_f \qquad\qquad \text{Equation 2.4}$$

This is known as the Curie-Weiss law and determines ferromagnetic susceptibility above the Curie temperature (T_C).

Since $H_w \gg H$ below the Curie temperature we can neglect the external field H and rewrite

$$\frac{M}{M_S} = \mathcal{L}\left(\frac{\mu_0 m_b BM}{KT}\right) \qquad\qquad \text{Equation 2.5}$$

or

$$\frac{M}{M_S} = \mathcal{L}\left(\frac{T_C}{T}\cdot\frac{M}{M_S}\right) \qquad\qquad \text{Equation 2.6}$$

Where, $T_C = \dfrac{N\beta m_b^2}{vK}$

Below the Curie temperature (T_C), due to the alignment of unpaired electronic spins over a large area within the crystal certain crystals have a permanent (remanent) magnetization. The magnetic spins can be either parallel or anti-parallel which is controlled entirely by crystal structure of the materials and the energy term associated with this phenomenon is called exchange energy. Depending on the spin configuration there are three main categories of spin alignment: ferromagnetism, ferrimagnetism and antiferromagnetism (Fig. 2.2). In ferromagnetism all the spins are parallel and the exchange energy is minimized as occurs in pure iron. In antiferromagnetism spins are perfectly antiparallel and there is no net magnetic moment. In some crystals the antiferromagnetic spins are not aligned in a perfectly antiparallel orientation, but are canted by a few degrees which give rise to a weak net moment.

The magnetic anisotropy phenomenon is well established by theoretical and experimental investigations. As already described there is an obvious interest of magnetic anisotropy of ferromagnetic thin films and nanostructures for technological applications. The classification of the magnetic anisotropy is based on their physical origins such as spin–

orbit coupling (SOC), dipolar magnetic interaction, and exchange interaction. Based on that, magnetic anisotropy is classified in to magnetocrystalline, magnetoelastic, dipolar/shape, exchange, dipolar crystalline, etc. The dipolar crystalline anisotropy can be neglected due to its small magnitude. Magnetocrystalline anisotropy, magnetoelastic anisotropy, and shape anisotropy have been thoroughly investigated on bulk magnetism, ultrathin film magnetism, and for different magnetic nanostructures within last few decades. In the following sections, an overview of the electronic origin of different kind of magnetic anisotropy is briefly discussed. The shape/dipolar magnetic anisotropy in nanomodulated films and exchange bias in different nanostructures are introduced, and the recent research trend in relation to that has been addressed. A comprehensive literature review has been carried out to identify different methods to control magnetic anisotropy of different magnetic materials. Different techniques to control anisotropy reported for the various structured materials have been overviewed, highlighting the respective advantages and disadvantages of each of the techniques. Examples of the techniques employed include patterned, isolated magnetic structures and structured continuous magnetic films. These approaches have certain limitations which inhibit their use for device applications. For example, why the isolated nanostructure forms vortex at frustrated state and one dimensional structure doesn't have much control over anisotropy, etc alongwith some potential solutions have been discussed below.

2.2. Types of magnetic anisotropy

Magnetic anisotropy has historically been analyzed by means of the anisotropy of susceptibility and the anisotropy of an artificial remanent magnetization. Both types are due to a non-isotropic distribution of magnetic grains. Six mechanisms have been proposed to explain magnetic anisotropy, whereby shape anisotropy and crystalline anisotropy are the most important ones.

2.2.1. Shape anisotropy

One of the important sources of magnetic anisotropy is shape. To understand how the shape controls magnetic energy of the material, the concept of the internal demagnetizing field of a magnetized body needs to be understood. The magnetic vectors within a ferromagnetic

materials produced by an external magnetic field is proportional to the magnetic moment. A magnetized body will produce a set of free poles distributed over the surface of the materials. This surface magnetic charge distribution or surface magnetic poles do not just produce the external field, rather they produce an internal field as well which is known as the demagnetizing field (H_{dem}). The applied field causes surface magnetic charges, which produce an internal field in the opposite direction of the external field. If field is applied, the effective field (H_{eff}) along the field direction is:

$$H_{eff} = H_{ext} - H_{dem}$$
<div align="right">Equation 2.7</div>

The demagnetization field is proportional to the grain magnetization, the constant of proportionality being the demagnetization factor (N_i). Therefore the effective field can be written as:

$$H_{eff} = H_{ext}M - KH_{ext}N_xH_{eff}$$
<div align="right">Equation 2.8</div>

where N_x is the demagnetization factor along the x-axis and M is the magnetization of the grain. The relationship between the effective field and the external field considering isotropic susceptibility is:

$$H_{eff} = H_{ext}\frac{1}{1+N_xK}$$
<div align="right">Equation 2.9</div>
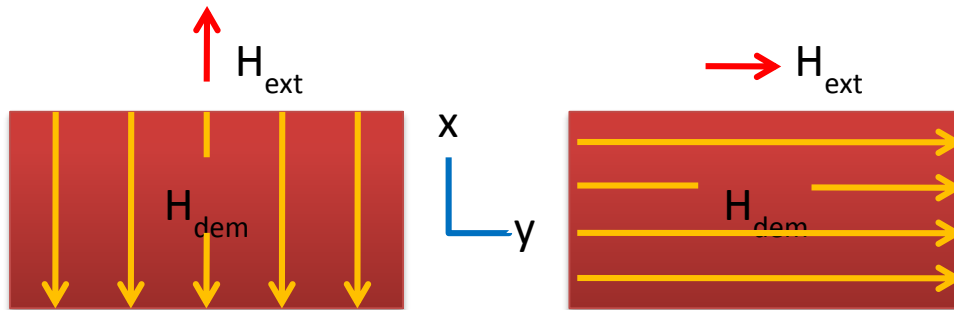
Fig.2.3. Shape anisotropy of rectangular film

Consider a thin-film of rectangular shape with H_{ext} applied along x-axis. The magnetization is:

$$M_xH_{eff} = -K_xH_{ext}\frac{1}{1+N_xK}$$
<div align="right">Equation 2.10</div>

In the example presented in Figure 2.3, the H_{dem} is higher when H_{ext} is applied parallel to the x-axis as compared to the y-axis, because $N_x > N_y$, therefore $M_x < M_y$.

2.2.2. Anisotropy due to domain alignment

When magnetic thin-films are deposited on a substrate they form grains. In the growth process the magnetic energy and the magnetic charge grows with grain size. At a certain point, magnetic domains take a critical size which minimizes the magnetostatic energy. Each magnetic domain is a region of the material where the magnetization has a constant direction (Fig.2.4a&b). The region in which the magnetization changes its orientation from one domain to another is called a domain wall or Bloch Wall (Fig.2.4c). Magnetic susceptibility values depend on the direction of the applied field with respect to the domains of the magnetic material. When an external field is parallel to the domain walls, the obtained susceptibility (K) is a measure of the ease with which the 180° walls may move. The susceptibility perpendicular to the domain walls is due to the rotation of the spontaneous magnetization against the forces of magnetocrystalline anisotropy.
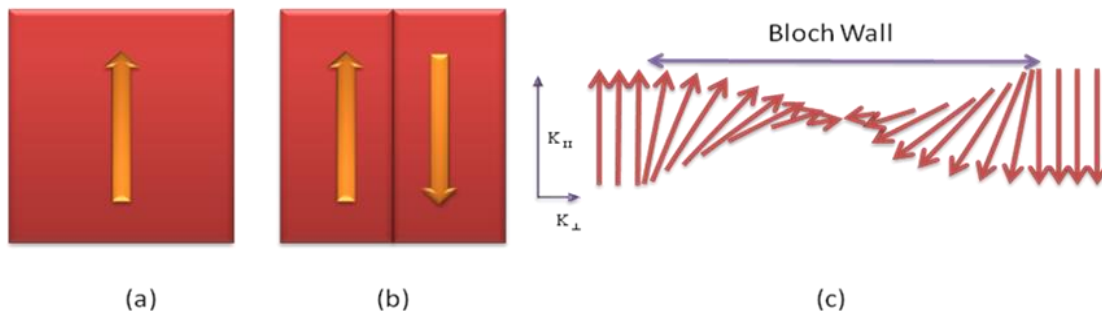
Fig.2.4. Formation of two-domain grain decreases the magnetostatic energy. a) single-domain grain, b) grain with two domains, in which the magnetic susceptibility has a different value parallel (K_{II}) or perpendicular ($K_{\perp}$) to the domain wall and c) simplified model of a domain wall.

2.2.3. Crystalline anisotropy

For magnetic materials with single-domain or with low saturation magnetizations, the crystal structure determines the magnetic anisotropy. In such materials the easy direction of magnetization or easy axis is aligned along the crystallographic directions along which magnetocrystalline energy is minimum. In crystals, the arrangement of the ions in the lattice structure affects the exchange process. As a result the direction of magnetization is

directly influenced by this exchange and magnetocrystalline anisotropy. The spatial configuration of the cations and anions in the crystal is responsible for crystalline anisotropy in common ferromagnetic minerals. The super-exchange phenomenon is more effective in a certain direction than in others and therefore the magnetization prefers to lie along specific crystallographic directions. This behavior gives rise to an easy magnetization axis and a hard magnetization axis within the crystal. In Figure 2.5 the magnetocrystalline anisotropy energy density, E_a for magnetite at room temperature is shown. The highest energy bulges lie in directions perpendicular to the cubic faces (<001>, <010>, <100>) whereas the lowest energy dimples are along the body diagonals of the crystal unit cell (<111>).
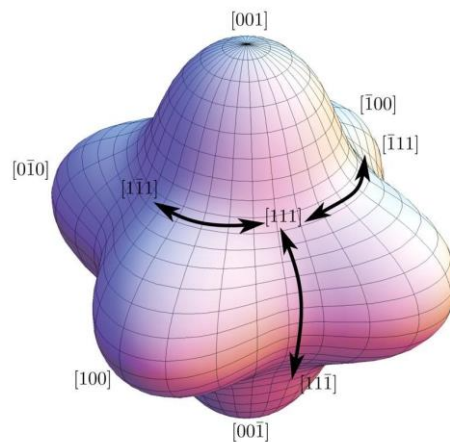
Fig.2.5. The magnetocrystalline energy is highest when the system is magnetized along a "hard" direction and lowest when magnetized along an "easy" direction. [Ref. 1]

2.2.4. Textural anisotropy

This is the term given to the magnetic anisotropy that results from the stringing together of magnetic grains in lines or planes. The stronger susceptibility lies parallel to the string of grains (Fig. 2.6).
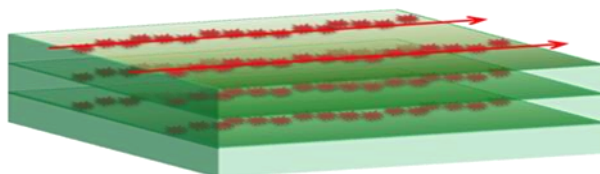
Fig.2.6. Schematic diagram of textural anisotropy. The arrow shows the direction of maximum magnetic susceptibility.

In natural materials the distribution of grains is generally related with structures in the samples, e.g., fractures or cracks, natural veins, minerals cleavage or void (e.g, Kligfield et al. (1982)).

2.2.5. Exchange anisotropy

This term was originally used to describe a magnetic interaction between an antiferromagnetic material and a ferromagnetic material and has been later extended to include the interaction between ferromagnetic and ferrimagnetic materials (Meiklejohn, 1962). The simplest model assumes a single domain of antiferromagnetic material and a ferromagnetic material with an interface plane separating them (Figure 2.7)
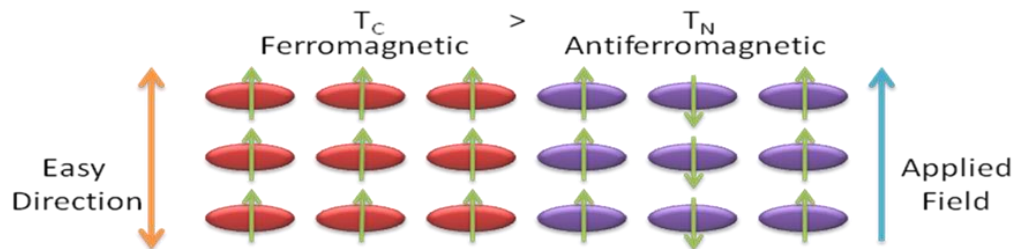
Fig.2.7. Simple model of exchange anisotropy. T_c is the Curie temperature of the ferromagneticphase and T_N is the Néel temperature of the antiferromagnetic phase.

When a large magnetic field is applied along the easy direction of magnetization with $T_N < T < T_c$, the ferromagnetic moments orient parallel to the applied field. If the specimen is then cooled through the Néel temperature T_N of the antiferromagnet, the spins of the lattice closest to the ferromagnet will align in the same direction as the ferromagnet. Subsequent spin planes will orient antiparallel to each other. These alternating antiparallel planes are highly anisotropic and hold the magnetization of the ferromagnetic material in the direction of the applied field.

The exchange energy per unit area of an exchange coupled assuming coherent rotation of the magnetic spin can be expressed as

$$E = -HM_{FM}t_{FM}\cos(\theta - \beta) + K_{FM}t_{FM}sin^2(\beta) + K_{AFM}t_{AFM}sin^2(\alpha)$$
$$- J_{INT}\cos(\beta - \alpha) \qquad \text{Equation 2.11}$$

Where, H is external applied field, M_{FM} is the saturation magnetization, β is the angle between the magnetization and the FM anisotropy, α is the angle between the AFM sublattice magnetization and AFM anisotropy axis, θ is the angle between the applied field and the FM anisotropy axis, t_{FM} is the thickness of the FM layer, t_{AFM} is the thickness of the AFM layer, K_{FM} is the anisotropy of the AFM layer and J_{INT} the interface coupling constant.

It is considered that the FM and AFM anisotropy axes are in the same direction. In the energy equation the first term is for the effect of the applied field on FM layer, the second term represents the effect of the FM anisotropy, the third term is for the AFM anisotropy and the last term is due to interface coupling.

2.2.6. Stress induced anisotropy

In addition to above anisotropies, there is another anisotropy effect related to spin-orbit coupling arises from the strain dependence of the anisotropy constants which is called magnetostriction. Due to magnetization, a previously demagnetized crystal experiences a strain which can be estimated as a function of external applied field along the principal crystallographic axes. Hence a magnetic material changes its dimension when magnetized.

The reverse effect or the change of magnetization due to stress can also occur. A uniaxial stress can generate a unique easy axis of magnetization or uniaxial anisotropy if the stress is sufficient to overcome all other anisotropies. This type of anisotropy is of interest, since it may lead to a possible deflection of the magnetization of rocks as a result of a tectonic stress.

2.2.7. Induced uniaxial anisotropy

Inducing a uniaxial anisotropy by the application of a magnetic field parallel to the plane of the depositing film is a widely used technique in thin film deposition where it is preferable to align the domain magnetisation in a particular direction during the deposition. The magnetic field is usually provided by permanent magnets which are positioned on

either side of the substrate in which direction the uniaxial anisotropy needs to be created. It is important that the field applied by the permanent magnets needs to be parallel to the substrate surface and to minimise the number of flux lines which intersect the surface of the substrate.

There are other ways to create uniaxial anisotropy. One of the most commonly used method is thermal annealing. Macrosocpic anisotropy can be induced by applying a saturating magnetic field during thermal treatment so that the domain structure of the magnetic material consists of a single domain during the process. In voltage-driven spintronic devices the induced anisotropy can be created by applying very high voltage during the film deposition.

2.3. Anisotropy control

2.3.1. Crystal structure

Magnetocrystalline anisotropy is one of the fundamental parameters in the analysis of magnetic behavior of magnetic materials. It can be easily observed by measuring magnetization curves along different crystalline directions. Magnetocrystalline anisotropy is the energy necessary to rotate the magnetic moment in a single crystal between the easy and the hard directions. In single-domain particles or particles with low saturation magnetizations the crystal structure of the materials dominates the magnetic energy. The so-called easy directions of magnetization are crystallographic directions along which magnetocrystalline energy is at a minimum. The magnetically easy and hard directions arise due to the interaction of the spin magnetic moment within the crystal lattice known as spin-orbit coupling. As a consequence of the magnetocrystalline anisotropy energy when the magnetization is aligned in an easy direction, work must be performed to change the magnetization in other direction. In order to switch from easy to hard direction or vice versa the magnetization has to traverse a path over an energy barrier which is the difference between the energy required for the spin to be aligned in the magnetically easy and hard directions. In cubic crystals the magnetocrystalline anisotropy energy is given by an exponential series in terms of the angles between the magnetization direction and the axes

of crystal cube. The anisotropy energy can be represented in an arbitrary direction only by the first two empirical constant terms in the series called the first- and second order anisotropy constants, or k_1 and k_2 respectively.

The magnetic anisotropy in transition metals arises from spin-orbit coupling. The typical fourth-order approximation of the parameterization of uniaxial anisotropy expressed in terms of energy density is:

$$\varepsilon_{uni}^i = k_1 \cos^2(\theta_i) + k_2 \cos^4(\theta_i) = k_1 S_z^2 + k_1 S_z^4 \qquad \text{Equation 2.12}$$

Where,

ε_{uni}^i =The uniaxial anisotropy energy of a magnetic moment μ_i

k_1 =The primary anisotropy constant of a material obtained from experimental measurements, expressed as a temperature-dependent energy density

k_2 =The secondary anisotropy constant of a material obtained from experimental measurements,

θ_i = The angle between S_i and the easy.

Both the constants (k_1 & k_2) are expressed as a temperature-dependent energy density and can exist with either a positive or negative sign. When $k_1 > 1$ the axis is easy, when $k_1 < 0$ the axis becomes hard (which yields an easy plane).

By neglecting constant terms, an equivalent parameterisation can be written as:

$$\varepsilon_{uni}^i = k_1 \sin^2(\theta_i) + k_2 \sin^4(\theta_i) \qquad \text{Equation 2.13}$$

The typical cubic anisotropyparameterization is not straight forward trigonometrically:

$$\varepsilon_{cub}^i = k_1(S_x^2 S_y^2 + S_y^2 S_z^2) + k_2(S_x^2 S_y^2 S_z^2) \qquad \text{Equation 2.14}$$

where ε_{cub}^i is the cubic anisotropy energy of a magnetic moment $\mu_i k$.

The positive k_1 yields easy axes along the body edges (100) and negative k_1 indicates the easy axes across the diagonals (111). [2]

The energy for a system of magnetic moments is given by:

$$\varepsilon_{ah} = \sum_i \varepsilon_{cub}^i \qquad\qquad\qquad \text{Equation 2.15}$$

where, ε_{ah} is either ε_{uni} or ε_{cub}.

Materials like permalloys are considered isotropic (*i.e.* $k_1 = k_2 = 0$). The contribution to the total energy from the anisotropy for such kind of materials is zero. To induce anisotropy in those materials a novel technique such as nanomodulation technique is used, which is discussed in the next section.

2.3.2. Nanomodulation

In recent years magnetic anisotropy has been demonstrated for patterned, isolated magnetic structures [3-5] and structured continuous magnetic films [6]. Such kinds of control open up opportunities for potential applications such as spintronic devices, magnetic random access memory (MRAM) [7] high density patterned information storage media [7,8], and high precision ultra-small magnetic field sensors [9]. Due to fundamental reasons and potential applications, it is necessary to understand further the magnetic properties of patterned structures in reduced dimensions, while both geometry and crystal microstructure are needed to be optimized prior to configure the magnetization [10]. Subsequent investigations further reveal fascinating properties like geometrical frustration, domain wall pining, etc. due to dipolar interaction based on spin configurations [11,12]. Several methods such as ion irradiation through a mask [6], selective epitaxy [13], surface modulation [13], etc. have been studied to control the magnetization configuration in patterned structures. In recent years Ion beam lithography has been found to be very useful for transferring nanopatterns on three-dimensional surfaces. Ion beam lithography offers more precise nanopattern than UV, X-ray, or electron beam lithography because in this technique heavier particles with more momentum is used. Among all these, surface

nanomodulation is preferred for its cost effectiveness and simplicity to engineer spin configuration locally. [14] Furthermore, the optimization of magnetic parameters such as pattern geometry, film thickness, intrinsic anisotropy, and coercivity is essential to obtain a controlled anisotropy in a film by nanomodulation. Magnetostatic energy induced by strong nanomodulation forces the spins into local vortices which is unfavorable for many applications. Thus the development of a physical model for an optimized modulation is essential to manipulate film anisotropy.
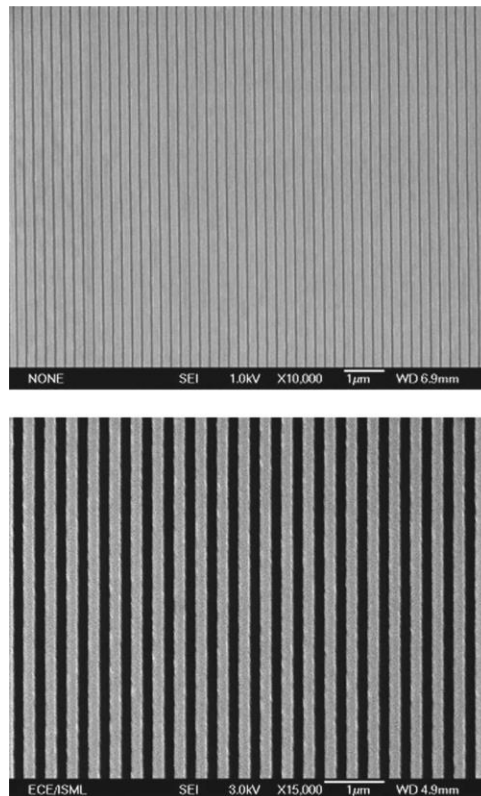
Fig.2.8. One dimensional nano structure gives 2 fold symmetry [Ref: 15]

Artificially created ordered corrugation produces controllable magnetic anisotropy. However, while the external field favors such magnetic dipole alignment, interdipole magnetostatic interaction results in a variation of the effective magnetostatic energy in different directions. This effect translates into in-plane anisotropy variation depending upon modulation geometry (Fig. 2.8, 2.9).
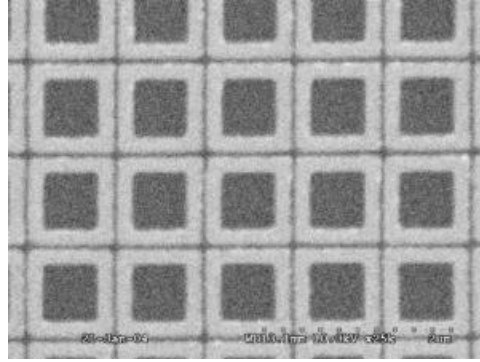
Fig.2.9. Dimensional nanostructure gives four fold symmetry [Ref: 16]

Magnetic anisotropy is the angular dependency of a specific magnetic property, e.g. magnetic susceptibility, remanent magnetization or saturation magnetization. In a given direction I, the relationship between magnetization and applied field is not a scalar but a second-rank tensor of magnetic anisotropy. The magnetization can be written as:

$$\begin{pmatrix} M \\ M \\ M \end{pmatrix} \begin{pmatrix} H \\ H \\ H \end{pmatrix} \begin{pmatrix} xx \\ yy \\ zz \end{pmatrix} = \begin{pmatrix} kk_{11}kk_{12}kk_{13} \\ kk_{21}kk_{22}kk_{23} \\ kk_{31}kk_{32}kk_{33} \end{pmatrix}$$

Equation 2.16

Magnetic dipole, generally a tiny magnet of microscopic to subatomic dimensions is equivalent to a flow of electric charge around a loop. Electrons circulating around atomic nuclei, electrons spinning on their axes, and rotating positively charged atomic nuclei all are magnetic dipoles. The sum of these effects may cancel so that a given type of atom may not be a magnetic dipole. If they do not fully cancel, the atom is a permanent magnetic dipole, as are iron atoms. Many millions of iron atoms spontaneously locked into the same alignment to form a ferromagnetic domain also constitute a magnetic dipole. Magnetic compasses needles and bar magnets are examples of macroscopic magnetic dipoles.

The strength of a magnetic dipole, called the magnetic dipole moment, may be thought of as a measure of a dipole's ability to turn itself into alignment with a given external magnetic field. In a uniform magnetic field, the magnitude of the dipole moment is proportional to the maximum amount of torque on the dipole, which occurs when the dipole is at right angles to the magnetic field. The magnetic dipole moment, often simply called the

magnetic moment, may be defined then as the maximum amount of torque caused by magnetic force on a dipole that arises per unit value of surrounding magnetic field in vacuum.
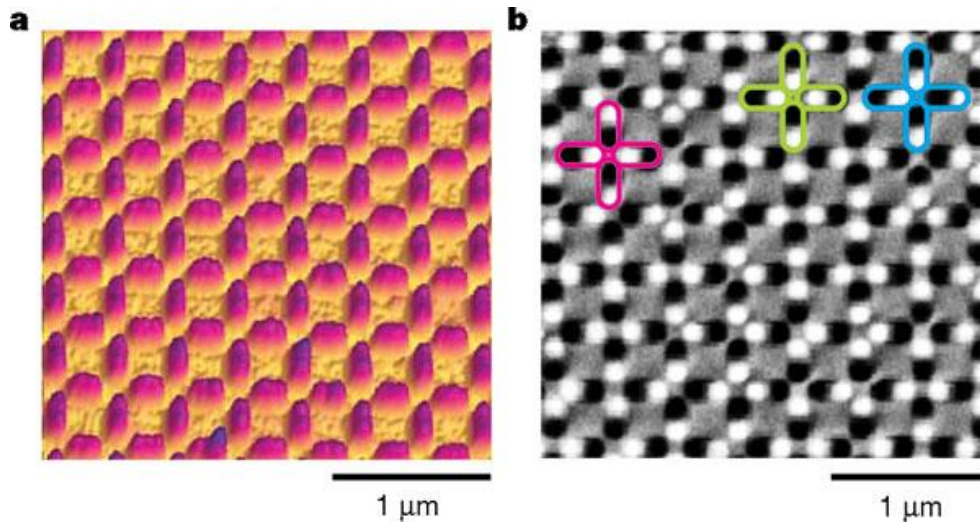
Fig.2.10. Atomic force microscopy (AFM) and magnetic force microscopy MFM images of a frustrated lattice [Ref: 17]

When a magnetic dipole is considered as a current loop, the magnitude of the dipole moment is proportional to the current multiplied by the size of the enclosed area. The direction of the dipole moment, which may be represented mathematically as a vector, is perpendicularly away from the side of the surface enclosed by the counterclockwise path of positive charge flow. Considering the current loop as a tiny magnet, this vector corresponds to the direction from the South to the North Pole. When free to rotate, dipoles align themselves so that their moments point predominantly in the direction of the external magnetic field. Nuclear and electron magnetic moments are quantized, which means that they may be oriented in space at only certain discrete angles with respect to the direction of the external field. In recent years the research focus is on the magnetic interaction of these tiny dipoles based on their geometrical arrangement (Fig.2.10) which opens up different new magnetic phenomena like magnetic monopole, artificial spin-ice, etc. [16, 17] These have been created much interest for their potential application in memory devices.

For such application it is essential to control the dipolar or magnetostatic interaction at a large scale. Magnetic dipole moments have dimensions of 'current times area' or 'energy divided by magnetic flux density'. In the MKS and SI systems, the specific unit for dipole moment is A^2m. In the CGS electromagnetic system, the unit is the erg (unit of energy) per gauss (unit of magnetic flux density). One thousand ergs per gauss equal one ampere-square metre. A convenient unit for the magnetic dipole moment of electrons is the Bohr magneton (equivalent to $9.27 \times 10^{-24} A^2m$). A similar unit for magnetic moments of nuclei, protons, and neutrons is the nuclear magneton (equivalent to $5.051 \times 10^{-27} A^2m$).

2.3.3. Exchange bias

The shift of hysterecis loop, initially called exchange anisotropy was first reported by Meiklejohn and Bean [18] in ferromagnetic (FM) Co particle encapsulated with antiferromagnetic (FM) CoO as quoted by them "*A new type of magnetic anisotropy has been discovered which is best described as an exchange anisotropy. This anisotropy is the result of an interaction between an antiferromagnetic material and a ferromagnetic material*". Later the name exchange anisotropy was changed to exchange bias. In the more than 60 years since its discovery, the phenomenon of exchange bias has become the basis for different important applications in micromagnetic technology with surge in research and development wordwide. However, it has only been within the last two decade or so when the basic, quantitatively predictive, fundamental understanding of exchange bias has been investigated significantly beyond the initial model presented by Meiklejohn and Bean. Primarily, exchange bias is the result of exchange interactions between ferromagnetic (FM) and anti-ferromagnetic (AFM) materials at the interface. Only recently these phenomena have been investigated thoroughly due to the required experimental and analytical tools for dealing with interfacial behavior at the atomic scale became available. Meiklejohn and Bean's discovery was initiated by the observation of the hysteresis loop measured below room temperature of a sample of nominal Co nanoparticles which was shifted along the field axis after cooling in an external applied field. They described how the exchange interaction across the interface between the FM Co and the AFM CoO could produce the shift in hysteresis loop along field direction and manifests exchange bias (Fig. 2.11).

Normally thr loop shift is measured after cooling under external magnetic field. The loop shift is equivalent to the assumption of a unidirectional anisotropy energy for the free energy at T=0 K of a single-domain spherical magnetic particle with uniaxial anisotropy. The uniaxial anisotropy is aligned with its easy axis in the direction of the external magnetic field(H) which is applied in the anti-parallel direction of particle's magnetization (Ms), i.e.,

$$F = HM_S cos\Theta - K_u cos\Theta + K_\perp sin^2\Theta$$ Equation 2.17

where Θ is the angle between the direction of magnetization and the easy direction of magnetization, K_u and K_1 are the unidirectional and uniaxial anisotropy energy constants respectively.

Solutions of this equation can be expressed in terms of an effective field

$$H' = H - K_u/M_S$$ Equation 2.18

which gives the hysteresis loop displaced by K_u/M_S along the field axis. Thus, an explanation of the loop shift is equivalent to explaining the interfacial unidirectional anisotropy.

For more than a half century this phenomena has been studied due to its potential applications in giant magneto resistance (GMR)[19], spin valve[20], high density storage media[21] etc. as well as for fundamental studies. The conventional way to induce exchange anisotropy, named exchange bias (EB) is to cool down a magnetically uncompensated AFM-FM interface below Neel Temperature (T_N) of AFM and Curie Temperature (T_C) of FM where $T_N<T_C$. A unidirectional shift of hysteresis or exchange bias should be observed in exchange coupled FM-AFM interface. In most cases the exchange bias is observed in the direction of cooling field, which is called positive EB.

Due to the AFM-FM interaction, the FM spins intend to point in the direction of the cooling field at low temperatures below T_N. In some cases due to the large unidirectional anisotropy of AFM, the AFM-FM interfacial interaction biases FM spins to the opposite direction of cooling field and causes a loop shift in opposite direction causing negative exchange bias. In addition an enhancement of coercively is also observed [6-8, 22-24]. Conventional field cooling is not necessary to introduce exchange bias in all cases. An exchange bias can be

observed in some AFM-FM interface, named spontaneous exchange bias when temperature is decreased below T_N, whereas field cooling enhance the effect. In very recent report Saha and Victora has discussed spontaneous mechanism of spontaneous exchange bias [25].
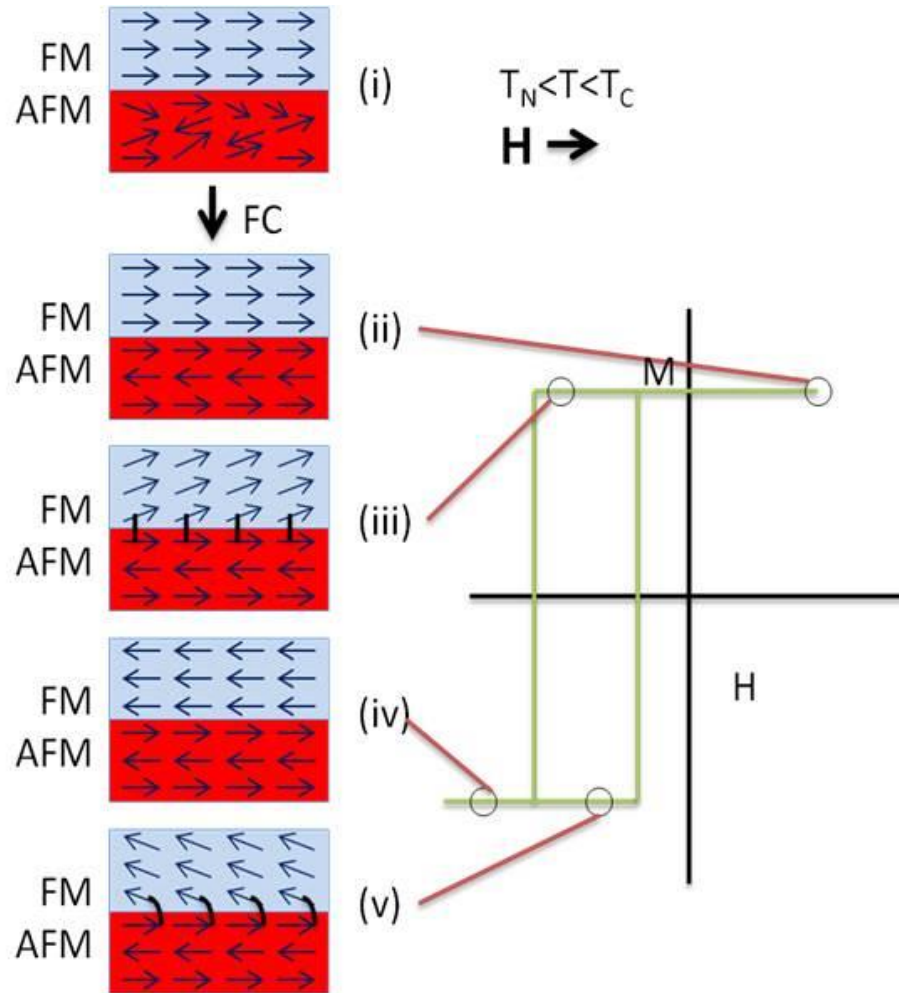
Fig.2.11. Schematic diagram of the spin configuration of an FM-AFM bilayer at different stages.

Extensive research has been done to investigate exchange bias phenomena in different materials, most of them are focused in AFM-FM bilayers. The Exchange bias effect has also been observed in various nano composite of perovskite oxides [26- 29] which is still not well understood. Recent reports show some nanoscale multiferroic materials [30, 31] show exchange bias which is not well investigated yet.

Different models of exchange bias:

Till now three main models are proposed to explain the exchangeanisotropy or exchange bias. The models are not mutually exclusive; often one incorporates several different ingredients in a particular calculation.

2.3.3.1. Meiklejohn and Bean - Direct exchange

This is the first and simplest model of exchange bias [18]. The antiferromagnet interface is uncompensated, with a net spin/area MAFM, and a Heisenberg coupling J_1 to the ferromagnetic spin MF is assumed:

$$E_{direct} = J_1(\boldsymbol{M}_{AFM} \cdot \boldsymbol{M}_F) \hspace{3cm} \text{Equation 2.19}$$

If one assumes that the antiferromagnet does not undergo reversal with the ferromagnet, then there will be unidirection anisotropy and the shift in the hysteresis curve (or the bias field) is immediately seen to be:

$$H_E = \Delta E / 2 M_F t_F \hspace{3.5cm} \text{Equation 2.20}$$

However this formula leads to bias fields that are orders of magnitude larger, and so refinements of this simple picture are described in the following sections. Recent experimental realization makesthis simple model more relevant than previously thought. It was found that there are in fact only very small percentages (4%) of moments at the AFM interface which are pinned. The rest of the moments rotate rigidly with the ferromagnet. Only these pinned moments contribute to the expression above, so that the predicted bias fields are reduced by a factor of .04, which leads to realistic values for the exchange bias. However, the nature of the pinning (its origin and magnitude) is not known.

2.3.3.2. Mauri - AFM spring:

Mauri realized that the exchange energy cost associated with reversal of the ferromagnet can be decreased by accommodating a domain wall within the antiferromagnet. A form of the energy function which accounts for this is given as follows:

$$E = -\boldsymbol{H}.\boldsymbol{M} - J_1[\boldsymbol{M}.\boldsymbol{m}] + \sigma/2.[1 - \boldsymbol{m}.\boldsymbol{n}] \qquad \text{Equation 2.21}$$

Here $\boldsymbol{M}$ is the ferromagnetic orientation, $\boldsymbol{m}$ is the orientation of the net spin of the antiferromagnet at the interface, $\boldsymbol{u}$ is the direction of the easy axis of the antiferromagnet; it is assumed that far away from the interface the antiferromagnet has relaxed to point along its easy axis. σ is the energy of a domain wall in the antiferromagnet. An expression for the switching field can be found (here we assumed the external field points in the z-direction):

$$H_E = J_1(\sigma/2)u_z/(J_1^2 + (\sigma/2)^2 - J_1\sigma(\boldsymbol{M}.\boldsymbol{u})_\perp \qquad \text{Equation 2.22}$$

If $\boldsymbol{u}$ is assumed to make an angle θ with the z-axis, then the above can be written:

$$H_E = (J_1/M_t)\frac{\cos\theta}{(r^2+1+2r|\sin\theta|)^{1/2}} \qquad \text{Equation 2.23}$$

with r = J/(σ/2). The important point to note is that the presence of the domain wall decreases the bias field by a factor outside of the brackets - which for realistic parameters can reduce the exchange bias field by one or two orders of magnitude, making the model predictions consistent with experiments. Typically it is assumed that the domain wall is present in the antiferromagnet (because of a weaker stiffness in the AFM). In the case where $r \to \infty$ (physically where the direct exchange J dominates, and is essentially frozen out of the problem), the above expression indicates an energy cost associated with ferromagnet reversal of σ - in this case, reversal costs the energy of 1 domain wall. If $r \to 0$, the domain wall (DW) is frozen out and we recover exchange bias $H_E = \Delta E/2M_F t_F$.

2.3.3.3.   Malozemoff - Random field exchange

The Mauri model gives a good explanation of the order of magnitude of the exchange bias. However, it suffers from some defects: for one, it is known that the exchange bias is not very sensitive to the thickness of the AFM. So even in very thin AFM, where a DW wall is impossible and Mauri's model is no longer relevant, we still have a bias field that needs explanation. Malozemoff et al. considered the effect of interface roughness on a compensated antiferromagnet-ferromagnet interface. It turns out to be energetically favorable to form domains on the antiferromagnet interface surface, and these domains lead to a reduction of H_E with a similar form as that found by Mauri.

The following figure demonstrates how a single bump in the interface can lead to a unidirectional exchange between the ferromagnet and antiferromagnet at a compensated interface:
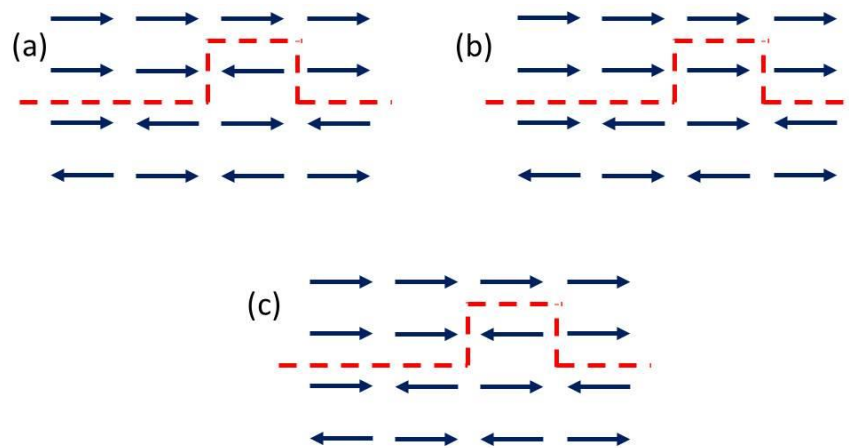
Fig.2.12. The presence of a bump at the interface changes the relative energy between ferromagnet orientations. The difference in energies between (a) and (b) corresponds to the exchange bias from a single bump. (Notice that (b) is the same as (a) with the FM reversed).

Figure 2.12 above shows how the spin configuration changes if we add a single bump at the interface. To find the energy associated with this bump, we count the number of reversed spin pairs the bump induces. Here the difference is 4 (1FM pair replaced by 3 AFM pairs). Fig 2.12 (b) shows the difference when the bump is shifted by 1 lattice site - (also, note configuration (b) corresponds to (a/c) when the ferromagnet in (a) is reversed).

In this case the difference in energy caused by the bump is -4 (1 AFM pair replaced with 3 FM pairs - the exact counting of energies can be tricky, but it's not important for us). Thus a single bump in the interfaceinduces unidirectional exchange energy of $\pm z_i J$ - where z_i is of the order unity and depends on the lattice details around the bump, and J is the atomic exchange energy. The sign of the exchange bias depends on the atomic location of the bump - so for example the sign in Fig.2.12 (a) and (b) are different. An interface with random spatial roughness will result in spatially random effective exchange energies between the antiferromagnet and ferromagnet. In this simple model, a collinear arrangement of spins is assumed so that the exchange energy per unit area takes on a value of $\pm z_i J/a^2$ at each atomic lattice site on the interface ('a' is the interatomic spacing).

The model further assumes that the ferromagnet is uniform. So each atomic site on the anti-ferromagnet surface has some random preferred direction, $\pm z$. If there is no energy cost associated with formation of domains in the antiferromagnetic interface, then clearly it is energetically favorable for each lattice site to assume its preferred position. There is of course an energy cost for domain formation, and so the game is to find the energetically optimum domain size.
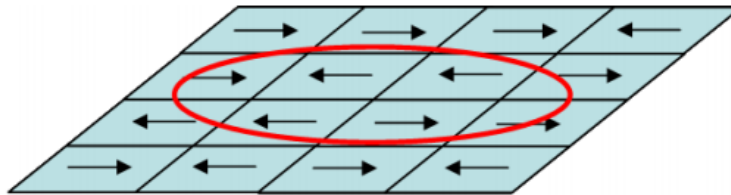
Fig.2.13. A representation of surface roughness as a random FM-AFM exchange at each atomic plaquette (arrows = random direction of exchange field), with a circular domain superimposed. A small domain size decreases random field exchange energy, the expense of domain wall energy.

The randomness of the problem plays a unique role in that as the domain size increases, a larger set of random exchange energies is averaged over, so that the exchange energy gain goes down (Fig.2.13). Specifically, for a domain of area L_2, the number of lattice sites is $N = L_2/a^2$, and the average unidirectional exchange energy per unit area is then $-z_i J/a^2\sqrt{N}$

$=-z_i/aL$. Mazeloff does the calculation to find the optimum domain size L, finding: $L \simeq \pi(A/K)^{1/2}$. This leads to a unidirectional exchange energy of $z_i (KA)^{1/2}$, or a bias field of

$$H_E=(KA)^{1/2}/2M_F t_F \hspace{4cm} \text{Equation 2.24}$$

which is the same form found in Meiklejohn and Bean model (in the r → ∞ limit). This model can explain the order of magnitude of H_E for very thin AFM layers. The notion of DW formation on the surface of the AFM as the source of exchange bias is a feature of more modern and elaborate theories of exchange bias.

2.3.3.4. Koon/Butler - Spin-flop coupling

Koon found that at a perfectly compensated interface, the interface spins of the antiferromagnet will cant slightly out of the plane. A perfectly compensated interface will decrease its energy by canting slightly out of the plane, towards the FM. This results in a small net moment which couples to the FM, and leads to a spin-flop coupling between the FM and the axis of the AFM.There will be a small net moment which is perpindicular to the axis of the antiferromagnet. This moment will couple to the ferromagnet, and leads to spin-flop coupling like interaction $K_2(\mathbf{M}_F \cdot \mathbf{M}_{AFM})^2$. Adding this term to the energy,one obtains:

$$E = -\mathbf{H}\cdot \mathbf{M} - \mathrm{J}[\mathbf{M}\cdot \mathbf{m}] + J_{sf}[\mathbf{M}\cdot \mathbf{m}]^2+(\sigma/2)[1 - \mathbf{m} \cdot \mathbf{u}] \hspace{2cm} \text{Equation 2.25}$$

Koon initially proposed that this coupling can lead to unidirectional anisotropy, or exchange bias. The mechanism is Mauri-like, in that it relies on partial longitudinal domain wall formation in the antiferromagnet. This result was initially supported by atomistic calculations of Koon (done with an XY-model, or strictly easy plane limitation). However, Butler *et al.* reportedmore detailed calculations which allow for out-of-plane spins, and including magnetostatic interactions. They found that a pure spin-flop coupling for Heisenberg spin term does not give rise to exchange bias. The extra freedom allowed in Butler's calculation allowed the antiferromagnetic orientation to switch between its degenerate minima before a domain wall is formed. This spin-flop coupling can, however, account for the enhanced hysteresis of the ferromagnet, Butler used a combination of spin-flop coupling, and Malozemoff random field effects to find realistic values for the exchange

bias. Stiles *et al* found that the addition of spin-flop coupling actually reduces the exchange bias field in the simple model given by above equation.

2.4   Different magnetic phenomena out of nanostrcutures

2.4.1. Superparamagnetism

Superparamagnetism (SPM) is a type of magnetism which occurs in small ferrimagnetic or ferromagnetic nanoparticles with size around a few nanometers to a couple of tenth of nanometers, depending on the materials. In a simple approximation, when the size of the nanoparticle are smaller than its single domain size the total magnetic moment of the nanoparticle can be regarded as one giant magnetic moment, composed of all the individual magnetic moments of the atoms of nanoparticle. These nanoparticles are called superparamagnetic nanoparticles. In such nanoparticles having5 uniaxial anisotropy, magnetization can randomly flip direction under the influence of temperature. The typical time between two flips is called the Néel relaxation time:

$$\tau = \tau_0 exp\left(\frac{\Delta E}{k_B T}\right)$$

Where,

τ_0=The length of time characteristic of the probed material.

Δhe length of barrier the magnetization flip has to overcome by thermal energy.

k_B: The Boltzmann constant

T: Temperature.

 The observation of superparamagnetic state in nanoparticles does only depend on the temperature T and energy barrier ΔE but also measurement time τ_m of each experimental technique. Depending on the measuremnt time two scenarios can occur. When the measurement time is much smaller than the relaxation time, a well defined blocked state can be observed. If the measurement tttime is much larger than the relaxation time a time-averaged net zero magnetic moment is observed due to the fluctuation state of magnetization which is called superparamagnetism.

2.4.2. Superferromagnetism

Superferromagnetism is the magnetic state of an ensemble of magnetically interacting very small size (nano) magnetic material with super-moment. In the case of diluted nanoparticle systems where the magnetic interactions between particles are ignored, it is a superparamagnetic state of the nanoparticles due to the absence of a collective order. For highly dense nanoparticles with strong magnetic interactions, it can reach a superferromagnetism stage due to a collective ferromagnetic order. For example, nanoparticles of ferrihydrite (nominally FeOOH) like iron oxides interact magnetically and due to the interactions the magnetic behaviours of the nanoparticles (both above and below their blocking temperatures T_B) are changed and lead to an ordered low-temperature phase with non-randomly oriented particle with super-moments which is called superferromagnetism.

2.4.3. Super Spin Glass

A spin glass is a disordered magnet, where the magnetic spin of the component atoms (the orientation of the north and south magnetic poles in three-dimensional space) are not aligned in a regular pattern. The spin glass is a random mixed-interactingsystem characterized by randomness and freezing of spins at a well-defined temperature T_f. Below the temperature a highly irreversible metastable frozen state generates without the usual long-range spatial magnetic order. The two most important charecteristics of spin glasses are, randomness in either position of the spins or the sign of interactions with neighbouring spin. Also a disordered, site or bond is required to create a spin glass. Otherwise the magnetic transition will be considered as standard ferromagnetic or antiferromagnetic type of long-range order. The term "glass" comes from an analogy from the positional disorder of a conventional, chemical glass, e.g., a window glass to the magnetic disorder in a spin glass. In amorphous solids like window glass, the atomic bond structures are highly disordered or irregular whereas in a crystal has a uniform pattern of atomic bonds.

In magnetic nanoparticle systems, the particale size are smaller than single magnetic domain size and become superparamagnetic which interacts to each other weakly. Magnetic moments of each nanoparticle are called superspins, and such weakly interacting magnetic nanoparticle systems are called superparamagnets. For dense magnetic

nanoparticle systems, slow dynamics or cooperative spin-glass dynamics originates due to frustration caused by strong dipolar magnetic interactions among the nano particles, randomness in the particle positions and magnetic anisotropy axis orientations. Such dense magnetic nanoparticle systems, which exhibit spin-glass behavior are called superspin glasses.

2.4.3. Inverted hysteresis loop

The hysteresis loop is the fundamental behaviour of ferromagnetism, which is characterized by two important magnetic parameters, the remanence magnetization M_r, and the coercive field H_C with positive values. For normal hysteresis loop when the field is decreased from positive saturation field a positive magnetization is observed which is called remanence magnetization M_r. A field is required in order to reverse its magnetization which is called the coercive field. These well-established features are challenged by inverted hysteresis loops (IHL) concept with partially inverted loops with negative remanence at positive coercive field. Instead of following the path anti clockwise, the loop follows clockwise path near the origin of the hysteresis loop.

2.5.   Sample preparation techniques

2.5.1. Electrodeposition and electroplated magnetic materials - films

In electroplating process electrolysis is used to deposit metal onto the surface of cathode. Electroplating is often called electrodeposition electrolytic deposition. It's a process which uses electrical current to reduce cations of a desired material from an electrolyte solution and deposit that material onto a conductive substrate surface. Figure 2.14 shows a typical electroplating system for the deposition of nickel from nickel sulphate solution on a metal (Cu) coated substrate. The electrolytic solution contains positively charged nickel (Ni+) ions (cations) and negatively charged sulphate (SO^{4-}) ions (anions). When an external electric field is applied, the cations are attarcted towords the cathode where they are discharged and deposited as metallic layer.

 Thickness of the electrodeposited layer on the substrate is controlled by the time duration of the plating and the applied current/ potential. The longer the time the substrate remains
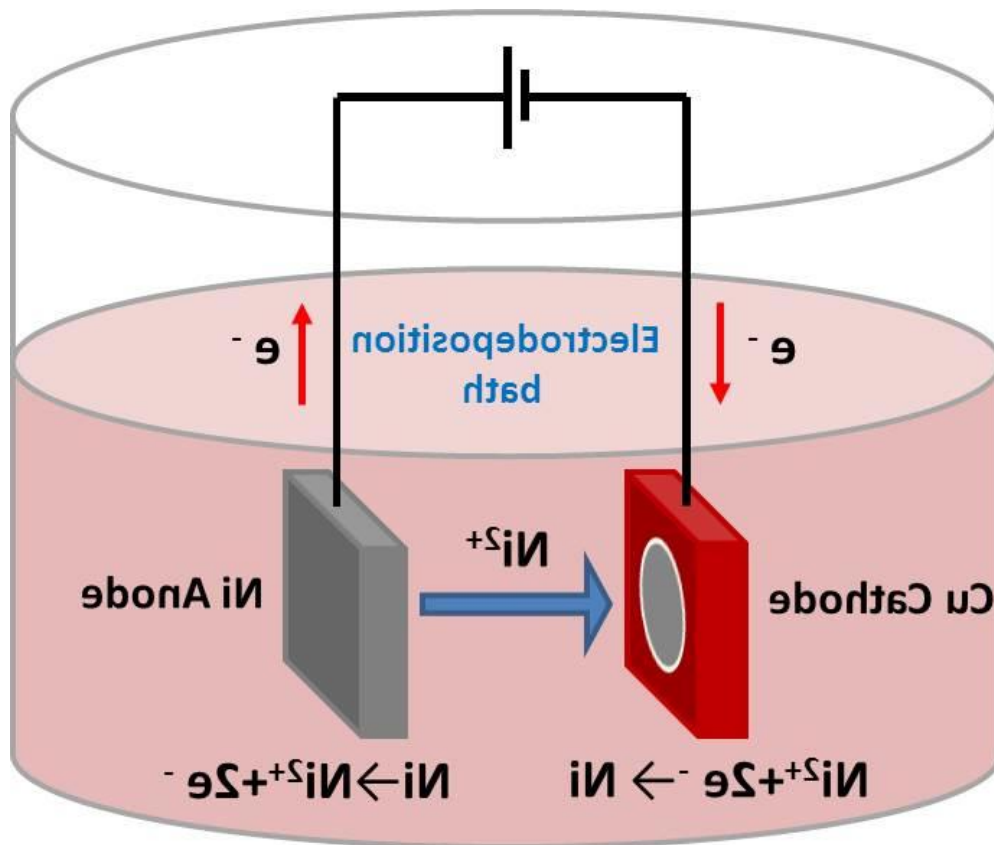
Fig.2.14. A schematic diagramme of electroplating example of Ni platting

Table 2: Material for electrodeposition

Chemical	NiFe bath	NiCo bath	NiFeMo Bath
$NiSo_4, 7H_2O$	200 g/L	300 g/L	60 g/L
$NiCl_2, 6H_2O$	5 g/L	50 g/L	
$FeSO_4, 6H_2O$	8 g/L		4 g/L
$CoSO_4, 7H_2O$		29 g/L	
$Na_2MoO4, 2H_2O$			2 g/L
H_3BO_3	25 g/L	30 g/L	
NaCl			10 g/L
Citic Acid			66 g/L
Sodium Lauryl Sulfate		0.1 g/L	
Saccharin	3 g/L	1.4 g/L	3.0 g/L

in the operating plating bath, the thicker the resulting electroplated layer will be. The thickness depends on applied current/ potential across the two electrodes as well. Typically thicknesses of the film can be varied from 100 nm to 30 microns. An electroplated layer is genrally composed of a single metallic material. Co-deposition of two or more metals such as a Cu-Zn alloy, Au-Sn alloy or Ni-Fe alloy is possible under suitable bath conditions. The development of micromagneic devices has widely based on the use of electroplated nickel-iron permalloy since it has good soft magnetic properties, high permeability, stable high frequency responses, etc. [28-30] Initially electroplated permalloy (Ni/Fe 80/20) has been widely used for micromagnetic devices. Later other alloy materials like NiFeMo, Ni-17Fe-4Mo, etc. have been investigated and used for better magnetic and mechanical properties [31-32]. Depending on the material composition the baths are prepared. Samples are electroplated on Si/Glass substrates with conducting titanium/gold/copper seed layer. Depending on alloy composition and deposition current, voltage, bath temperature, magnetic stirrer speed, external magnetic field, etc. are applied.

2.5.2. Sonochemical methods - nanocomposites

Researchers have recently developed sonochemical methods for the preparation of nanoparticles with controllable morphologies [33-34]. Ultrasound has become an important tool for the synthesis of different nanoparticles. Ultrasonic cavitation is formed when liquids are irradiated with ultrasonic irradiation. Ultrasonic cavitation which is is concerned with the formation, growth, and implosive collapse of bubbles, produces a variety of physical and chemical effects, such as high pressure (>20 MPa), temperature (>5000 K) and cooling rate (>1010 K s-1), which could provide a unique environment for chemical reactions under extreme conditions to prepare nanoparticles. Different research groups have demonstrated that ultrasound is a fine method to preparae nanoparticles with different controllable morphologies, such as dendritic, flowery, star-like, etc. It has been demonstrated that the ultrasonic irradiation plays a crucial role in the morphology of the product.

2.6. Nanocomposite multiferroic materials – The current state of the art

In the last decade or so there has been much research interest given on bulk single crystals to nanostructured multiferroic materials along with novel characterization techniques to investigate order parameters, coupling, spin dynamics, etc. with experimental and theoretical complexity. A single phase multiferroic [39] is a material that simultaneously possesses more than one of the 'ferroic' order parameters—ferroelectricity, ferromagnetism, and ferroelasticity. Magnetoelectric coupling typically refers to the induction of magnetization by an electric field or polarization by a magnetic field [40]. The potential to manipulate coupling between magnetic and electronic order parameters has captured the interest of researchers on multiferroics especially application at room temperature. It is known that the future system requirements in ICT devices drive towards size minimization reduce weight and minimal power consumption along with enhanced performance. To fulfill these requirements it requires to refocus the research efforts from conventional macroscopic "bulk materials" approaches toward innovative micro-nanoscale technologies of emerging complex oxide and multiferroic thin film materials. Recent research indicates that integrated thin film complex oxide and multiferroic materials are expected to play a significant role in the development of high performance device applications in the near future.
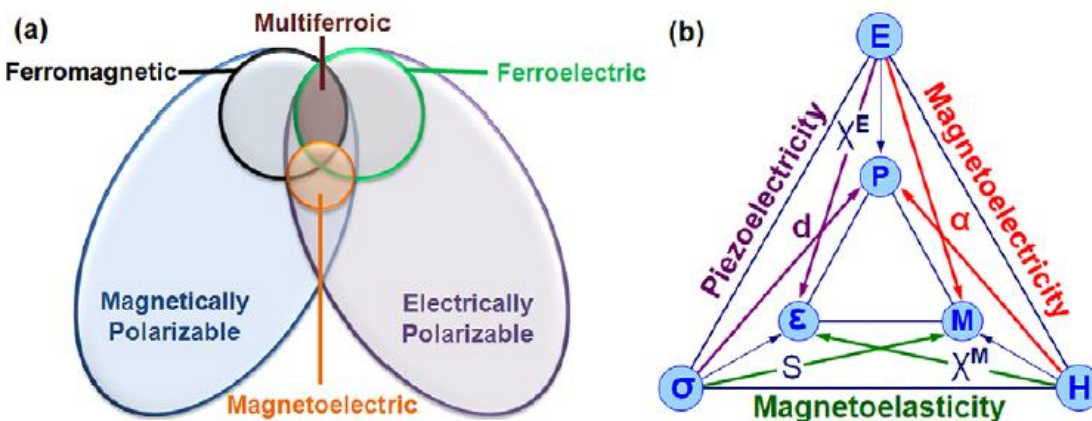
Fig.2.15. a) Relationship between multiferroic and magnetoelectric materials. (b) Schematic illustrating different types of coupling present in materials. Much attention has been given to materials where electric and magnetic order is coupled. These materials are known as magnetoelectric materials. [Ref: 41]

No other multiferroic has experienced the same level of interest in last decade as $BiFeO_3$ (BFO). The perovskite BFO was first invented in the late 1950s [42] and was thoroughly investigated for potential device application due to its magnetoelectric coupling [43]. Later in 1960/70s the physical and structural properties of BFO was studied. Initially BFO was suspected to be a G-type antiferromagnetic, ferroelectric multiferroic material [44, 45] with a N´eel temperature of ~673 K [46] and possessed a cycloidal spin structure with a period of ~620 Å[47]. Later the magnetic nature of BFO was studied in detail. It was also identified that if the magnetic moments were oriented perpendicular to the [111]-polarization direction the symmetry allow a small canting angle of the moments in the structure which results a weak ferromagnetism of the Dzyaloshinskii–Moriya type (Fig.2.15.) [48, 49].

At ferroelectric state BFO possesses a distorted rhombohedral ABO_3 type perovskite multiferroic with space group R_{3c} with lattice parameters, a_r = 3.965 Å and α_r = 89.4° at room temperature. [50] Above the Curie temperature (T_C= K), the structure possess a high symmetry cubic phase. Magnetic character of pure phase in single crystal is antiferromagnetic. On the other hand there have been some controversies on magnetism in thin film BFO where presence of impurities like Fe^{2+} and other iron borne impurities can show significant amount of magnetism. [51]
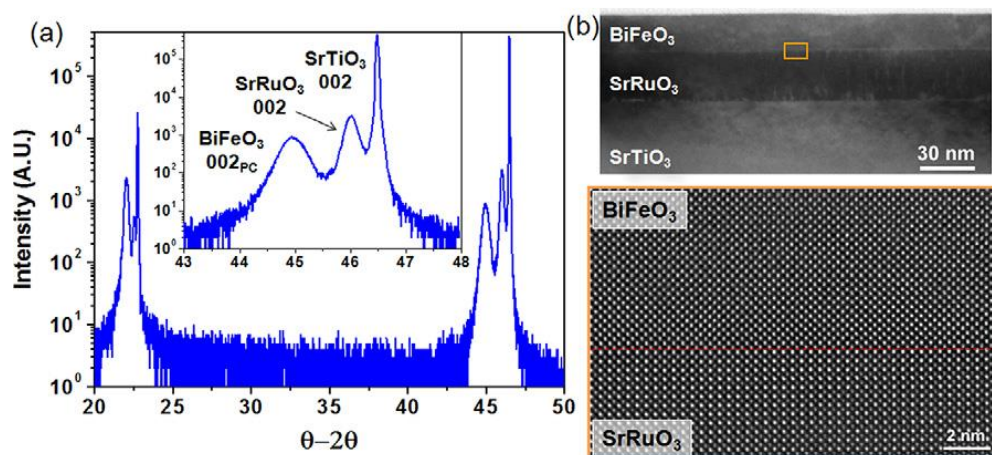
Fig.2.16. (a) X-ray diffraction results from a fully epitaxial single phase BFO/SRO on STO(001) heterostructure. (b) Low and high resolution TEM images of BFO/SRO/STO(001) heterostructure. [Ref: 41]

2.7.   Exchange bias systems – The current state of the art

Exchange bias was first observed in fine particles by Meiklejohn and Bean in 1956. It was observed that the hysteresis loop below room temperature of a sample of Co nanoparticles was shifted along the field axis after cooling in an applied field. It was subsequently investigated that the ferromagnetic Co particles had been partially oxidized to CoO which is an antiferromagnetic material. Meiklejohn and Bean described how the exchange interaction across the interface between the FM Co core and the AFM CoO shell could produce the shifted hysteresis loop and the other unique manifestations of exchange bias. The Fig. 2.15 shows shifted hysteresis loop at 77 K in oxidized Co particles (10-100 nm). The shifted loop was measured after cooling in a field of 10 kOe. Meiklejohn and Bean showed that the loop shift was equivalent to the estimation of unidirectional anisotropy energy in terms of free energy at 0 K of a single-domain spherical particle with uniaxial anisotropy, aligned with its easy axis in the direction of the fieeld, H.

Since its discovery, exchange bias has been mainly observed in ferromagnetic particles covered with their antiferromagnetic or ferrimagnetic native oxide like Co—CoO [18], Ni—NiO [52], Fe—FeO [53], etc. The particles studied are usually nanoparticals of size range 10—100 nm and prepared by a number of methods, such as vapour deposition, electrodeposition, reduction of the oxalate or mechanical alloying, sputtering, etc. In small particles it's difficult to determin the exact FM and AFM thicknesses. Hence it is difficult to conclude a quantitative comparison of the results between different systems. Thus these systems are not ideal for fundamental study of exchange bias. Apart from that distribution of particle sizes, irregular shapes make it difficult to identify the nature of the interface, stoichiometry, etc. of the FM-AFM layers.

The other major group is materials with multiple random AFM-FM interfaces, which are mainly polycrystalline materials with a mixture of AFM (or ferri) and FM components, so called inhomogeneous materials. Examples of the most studied in this group are Co sputtered in low oxygen pressure atmosphere, which includes Co rich and CoO rich areas [54], co-sputtered CoCr [55] or NiO with $NiFe_2O_3$ precipitates [56].
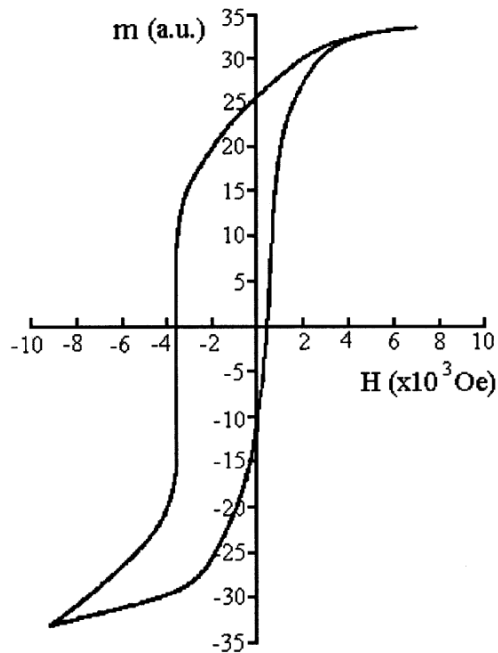
Fig.2.17. Exchange anisotropy first observed by W. Meiklejohn and C. P. Bean on Co-CoO particle at 77K after field cooled [Ref: 18]

Exchange bias has been mostly studied in the materials in thin film form. In such systems the interface can be effectively controlled and well characterized [57, 58]. From the application point of view as well, most of the device applications are based on thin film systems of exchange bias [59, 60]. Moreover, in thin film systems there are many basic interesting parameters like AFM thickness [61], interface disorder [58], orientation dependence of H_E [57], multi FM-AFM layers, etc. which open up new functionality in the exchange bias phenomenon. Among the layered systems, though AFM-FM interfaces based exchange bias are the most investigated, however other related systems such as AFM-ferri [62], ferri-ferri [63], ferri-FM [64] have also been investigated. The exchange bias based on AFM-FM interface can be divided in three main categories depending on AFM part: oxide, metallic and others. In this thesis both oxide and metallic materials have been thoroughly investigated for exchange bias studies.

3. Chapter – Experimental techniques

3.1. Magnetic Characterizations of Materials

3.1.1. Introduction to Magnetic characterization:

The materials were characterized in our magnetic characterization laboratory using two different instruments, an SHB instruments (Mesa 200-HF) Magnetic Measurement System real time B-H loop tracer and a Quantum Designs MPMS-XL5 superconducting quantum interference device (SQUID). An overview of this process and some of the results to date are outlined in this section. The first step prior to examining the results is to outline the operation of the instruments used.

- The first instrument is a B-H loop tracer (hence forth referred to simply as the SHB) which was initially used to characterise thin-film samples. This instrument has the advantage of being a real time measurement at room temperature, allowing samples to be analysed quickly and inexpensively. All thin-film samples were analysed using this instrument.
- A selection of samples was chosen to be analysed using the Superconducting Quantum Interference Device (henceforth referred to as the SQUID) which is a far more sensitive instrument. A selection of thin-film and powder samples were measured, with room temperature and low temperature (down to 10K) measurements being performed.

3.1.2. Characterization of materials with the hysteresis loop tracer

For this work hysteresis loop tracer (MESA 200 HF) by SHB Instruments Inc. [65] was used which measures in the frequency range of 10 Hz and below. The mechanism of real time hysteresis loop tracer is to apply an AC magnetic field to the sample (thin film) and measure the flux density as a function of applied field generated by the magnetic coil where the sample acts like core material for the coil. To obtain the magnetic induction the response voltage from the sense coil is integrated by the instrument. In absence of a sample the instrument would still show an elliptical loop from the sensor coil itself due to the

applied field on it. To nullify this error a balancing error correction i.e. a balance coil placed in series with the sensor coil should be done prior to any measurement. Other possible error in the measurements can be from noise pickup and the phase error between the applied current and the integrator output.
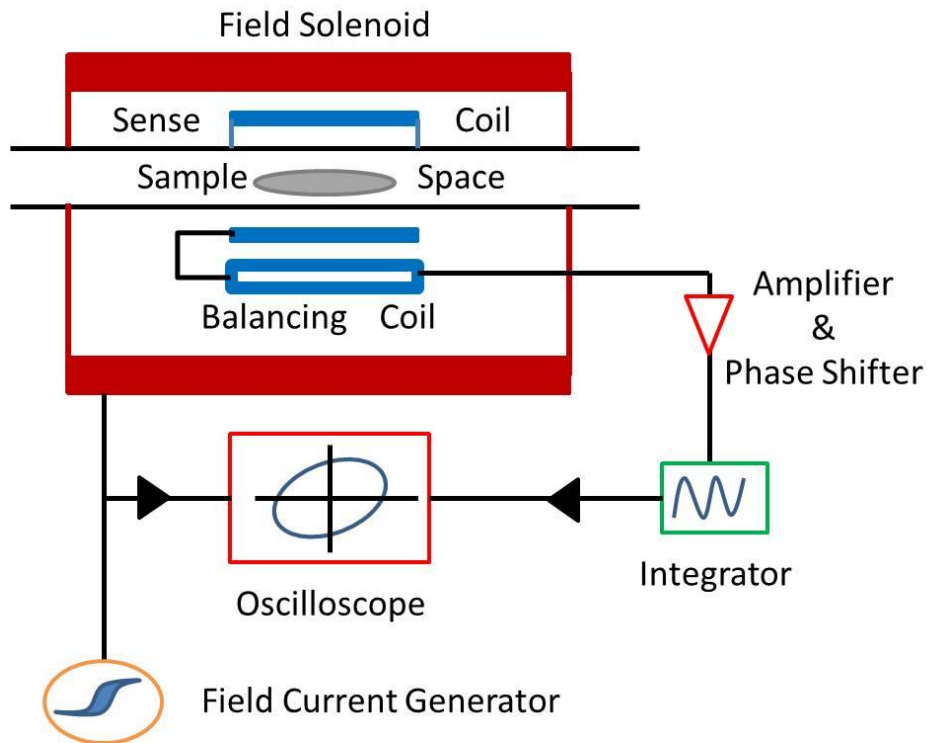
Fig.3.1. Schematic diagram of hysteresis loop tracer (MESA 200 HF) by SHB Instruments Inc.

As the SHB hysteresis loop tracer is calibrated for a 1 cm x 1 cm sample, thin-film samples were required to be diced to this size prior to analysis. This was done by either dicing the substrate on a wafer dicing machine prior to film deposition, or hand dicing of selected samples after the magnetic thin-film is deposited. The diced samples were then loaded onto the sample stage and inserted into the instrument. Various drive fields were applied to the samples with intensities of up to 1000 Oersted (Oe)/(0.1T) and the resulting magnetic induction (flux density) was measured.

Fig. 3.2. SHB MESA 200 HF hysteresis loop tracer

Once the samples were inserted into the SHB, the applied field and the measurement sensitivity were varied across the field range of the instrument. The resultant magnetic response of the material was observed on the instrument display screen. When a discernable B-H (magnetic flux density versus applied field) loop was observed, this showed that the material was within the range of sensitivity of the SHB. Typical material parameters examined were the saturation induction (B_s), the magnetic coercivity of the sample (H_c), and the anisotropy field of the sample (H_k), on both the hard and easy axis (where apparent). The samples were rotated with respect to applied magnetic field direction by rotating the sample stage.

Due to the relatively small volumes of magnetic material in very thin samples, resultant magnetic moments produced by the applied fields were often beyond the limits of the SHB

sensitivity 0.008% of full scale. As such some samples had to be characterized in the SQUID which has a greater sensitivity range.

3.1.3. Characterization of materials with the SQUID

Quantum Design Superconducting Quantum Interference Device (SQUID) with 5 Tesla range Magnetic Properties Measurements System (MPMS-XL5) was used for magnetic measurements with high accuracy [66]. Measurement protocol of SQUID is based on low temperature superconductors operating at liquid helium temperature. The working principle of SQUID is based on magnetic flux quantization in a superconducting cylinder which makes possible very high sensitivity in voltage, current and magnetization measurements. The Josephson Effect leads to high sensitive measurements The SQUID with its electronic circuits able detect about of a flux quantum (40 =h/2e). The superconducting Nb-wire (0.08 mm in diameter) magnetic flux transformer consists of pick-up coils and a SQUID coil. A superconducting contact is obtained by pressing the wires mechanically together. During operation sometimes it's required to destroy the supercurrent generated in the magnetic flux transformer. A carbon resistor of 10 kΩ is mounted in thermal contact with the wire to minimize unwanted magnetic fields near the magnetic- flux transformer. The whole SQUID unit is enclosed in a superconducting lead to avoid vibrations, and it must be rigorously shielded against external magnetic fields.

For magnetic measurement the magnetic field B is generated by the superconducting magnet coil. The sample is slowly moved up and down through the pick-up coils by a hydraulic system. The magnetic moment of the sample produces a magnetic flux change in the pick-up coils. The magnetic flux transformer exhibits a superconducting loop, thus transforming part of the total magnetic flux change from the pick-up coils into the SQUID. A typical signal curve generated from a sample due to an applied field is shown in Fig. x. The samples with high magnetic moment should be moved very slowly through the pick-up coils so that it does not exceed the maximum slewing rate of the electronic system.
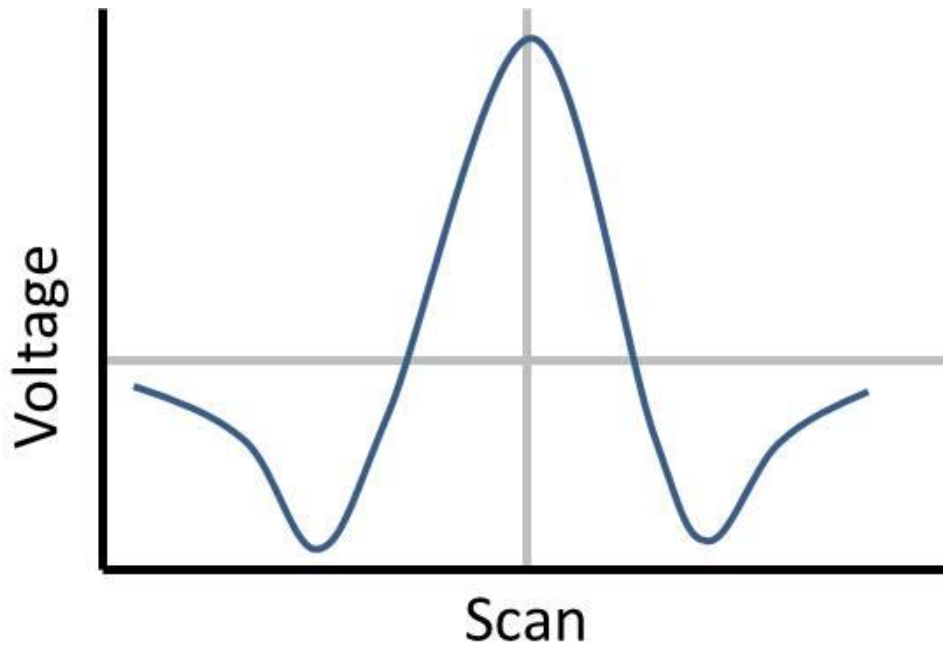
Fig.3.3. Output voltage vs. sample position plot, as a result of moving the sample through the pickup coils under an applied field.

A Prior to running samples on the SQUID, the samples were prepared by dicing them into a suitable size. The maximum size of a sample which can be inserted into the SQUID using the standard transport is approximately 6mm x 15 mm. To minimize the impact of shape anisotropy effect we diced the samples into a 4mm x 4mm size. They were then placed into a sample holder and inserted into the SQUID. The SQUID is calibrated to take account of the magnetic contribution of the straw, which may distort the measurements. The samples are next centered by applying a magnetic field sufficiently high so as to saturate the sample (up to 5T) and moving the sample through the SQUID's measurement coils. The operator then defines the center of the sample by visually inspecting the resultant centering curves and aligning the maximum point of the curve to the corresponding center point of the chamber. Once the sample is correctly loaded and centred, fields were applied to the samples varying from + 50000 Oe to -50000 Oe and the resultant magnetizationof the samples, in units of emu (electromagnetic units, $1000 \, emu/cm^3 = 1 \, A/m$), was measured.

01. Sample Rod
02. Sample rotator
03. Sample Transport
04. Probe assembly
05. He level Sensor
06. Superconducting Solinoid
07. Flow impedance
08. Squid capsule
09. Superconducting pick-up coil
10. Dewar Isolation cabinet
11. Dewar
12. Printer
13. Magnetic power supply
14. Temp. controller
15. Console Cabinet
16. Power distribution unit
17. MPMS controller
18. Gas/Magnet control unit
19. Computer
20. Monitor

Fig. 3.4. SQUID Magnetometer by Quantum Design

The SQUID measurement results are optimum in terms of time and accuracy for this unique new category of material. Both DC (or static) measurements (where the moment is measured in the prensence of a static magnetic field), as well as RSO (reciprocating sample option, where the sample is moved up and down relative to the pick-up coils in the presence of a static magnetic field) techniques were employed in the SQUID. For samples with low magnetic moments (not strongly ferromagnetic) both DC and RSO multimeasure techniques were used. This utilised a feature of the SQUID which measured the sample's magnetic moment many times and then applied statistical techniques to decide whether subsequent measurements were required to ensure that a certain percentage of the resultant magnetic moments fell within 2 sigma of the mean response. While the SQUID has a theoretical sensitivity and measurement sensitivity of 10^{-8} emu, in practice this requires both a prohibitively large amount of time and by extension liquid He to measure such samples on the SQUID.

Magnetic measurements using SQUID magnetometer:

High sensitivity magnetometry to measure magnetic susceptibilities is carried out in a SQUID (Superconducting Quantum Interference Devices) magnetometer. An equivalent SQUID circuit [67] is shown in Fig.3.5. A closed superconducting loop, which consists of a pickup coil and input coil, is shown in the figure. A persistent current is generated in the

superconducting loop due to the magnetic flux field measured at the pickup coil. The two Josephson tunnel junctions in SQUID which are shunted with resistors eliminate hysteresis in tunnel junction current-voltage characteristics. The output voltage across the Josephson junction appears due to the magnetic signal input at the pickup coil. The output voltage gradually changes due to the change of magnetic field for the quantum interference in Josephson junctions. Later this output signal is refined through modulation coil and converted to a magnetic moment.
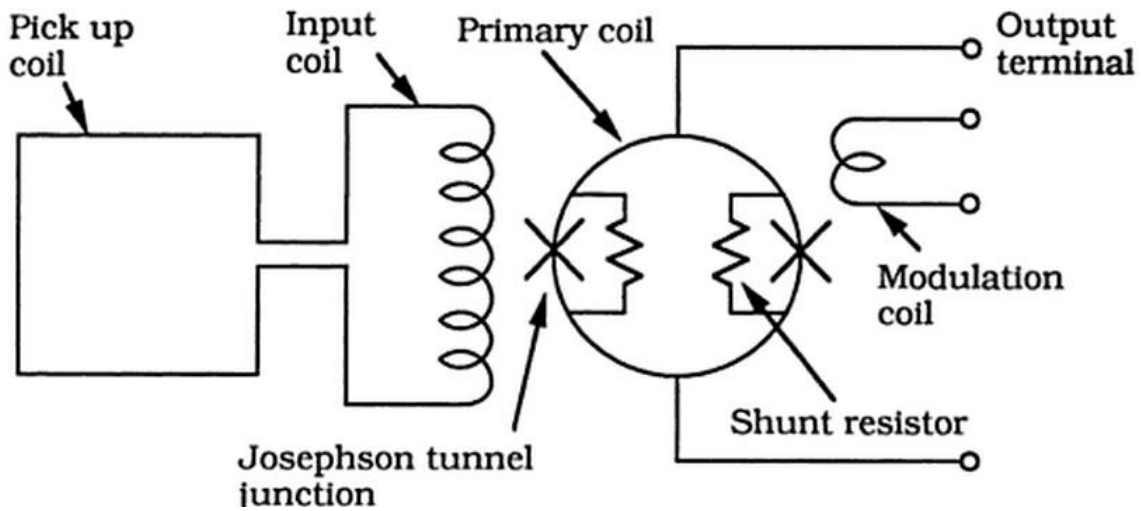
Fig. 3.5. Equivalent circuit of the SQUID for magnetometry

In a SQUID magnetometer, the magnetic moment of a sample can be measured as a function of temperature and external magnetic field using different measurement protocols. A typical temperature dependent magnetization ZFC (zero field cooled)-FC (Field Cooled) curve constitutes a widespread experimental measurement protocol to investigate the magnetic properties as a function of temperature and bias field. These are mainly low field susceptibility measurements and generally follow a particular procedure explained below:

1. Before any measuremnts each sample was demagnetized by a well designed demagnetized protocol by aplication of an oscillating field with varying amplitude; the amplitude reduces from maximum to zero. For example, for a demagnetizing field 1000 Oe, the amplitude is brought down to zero in the following sequence: (+1000)-(-900)-(+800)-(-700)...(+50)- (-40)...(+5)-(-4)-(+3)-(-2)-(+1)-(0).

2. The sample is cooled down from a high starting temperature (normally room temperature) to low temperature (2-5K) without applying any magnetic field.

3. A small magnetic field (chosen from the linear region of hysteresis loop of respective sample) is applied and kept. Then a response moment from the sample is measured while the temperature is swept up to the starting point and down again with the same cooling rate and data accusing rate.

4. Finally the field is removed and magnetization is measured with increasing temperature from lowest temperature to the highest temperature.
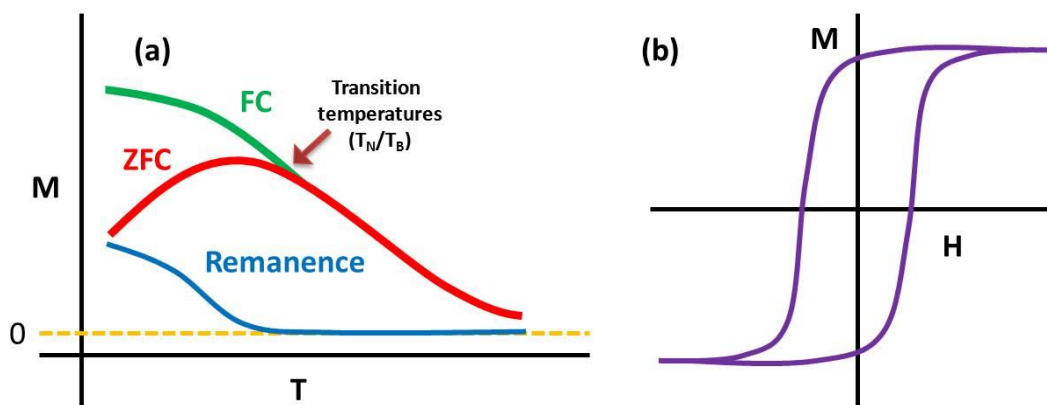
Fig. 3.6. A typical Zero Field Cooled (ZFC) – Field Cooled (FC) – Remanence curve (a) and magnetic hysteresis (MH) loop (b) measured in SQUID magnetometer

Hence the final curve is made of three different parts. The first part is called Zero Field Cooled (ZFC) curve, second curve is called Field Cooled (FC) curve and the third one is called remanence (REM) curve (Fig. 3.6.a). The point at which splitting between ZFC-FC curves occurs gives the transition temperatures, for example Neel temperature (T_N) or blocking temperature (T_B). Below T_N or T_B, the material is antiferromagnetic or ferromagnetic, and will give a small positive or a large positive remanence respectively. The other important measurement is magnetic hysteresis loop (MH) measurement, where the measurement is done as a function of field (Fig.3.6.b).

3.1.4. Characterization of materials with the MFM

The operating principle of magnetic force microscopy is the same as in AFM [68]. Both static and dynamic detection modes can be applied, but mainly the dynamic mode is considered here because it offers better sensitivity. The cantilever (incorporating the tip) is excited to vibrate close to its resonance frequency, with certain amplitude and a phase shift with respect to the drive signal. The deflection sensor of the microscope monitors the motion of the tip. Under the influence of a probe-sample interaction, the cantilever behaves as if it had a modified spring constantk , where c is the natural spring constant and $F_c = -\partial F/\partial z$. $\partial F/\partial z$ is the derivative of the interaction force relative to the perpendicular coordinate z. It is assumed that the cantilever is oriented parallel to the sample surface. Anattractive interaction with $\partial F / \partial z > 0$ will effectively make the
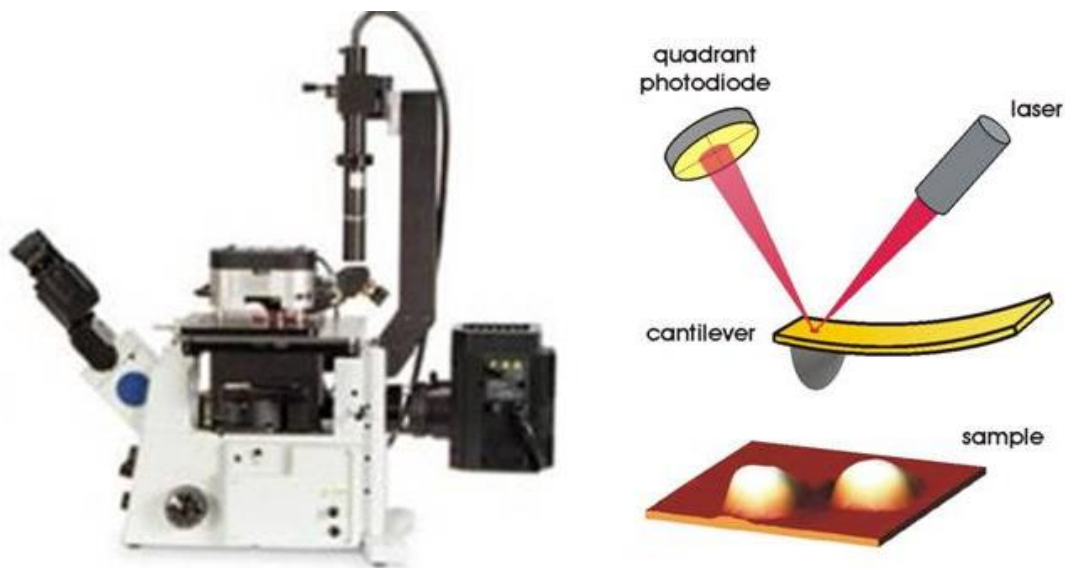
Fig. 3.5. Magnetic force microscopy (MFM) technique for surface imaging

cantilever spring softer, so that its resonance frequency will decrease. A shift in resonance frequency will lead to a change of the oscillation amplitude of the probe and of its phase. All of these are measurable quantities that can be used to map the lateralvariation of $\partial F/\partial z$. The most common detection method uses the amplitude signaland is referred to as amplitude modulation (AM). The cantilever is driven slightlyaway from resonance, where

the slope of the amplitude-versus-frequency curve is high, in order to maximize the signal obtained from a given force derivative.Measurement sensitivity, or the minimum detectable force derivative, has an inverse dependence on the Q value of the oscillating system. Therefore, a high Qvalue might seem advantageous, but this has the drawback that it increases theresponse time of the detection system. In the situations where Q is necessarily high, for example when scanning in vacuum, a suitable alternative is the frequency modulation (FM) technique. In this method the cantilever oscillates directly at its resonance frequency by using a feedback amplifier with amplitude control.

The VFM2-HV AFM-MFM by Asylum Research has been used for different AFM-MFM measuremnts in this thesis. The VFM2-HV can apply static magnetic fields up to ±0.8 T(~1 G resolution), parallel to the sample plane. A unique design incorporating rare-earth magnets are used to produce the magnetic field. Due to this, there is no effect of heating or drift during the change of the field which provides low-noise, high-precision scanning probemeasurements. By rotating the powerful rare-earth magnet it allows the magnetic field intensity variation at the sample (maximum field when rotated at 90°, field is turned off at 0° or 180°). Once a field value is reached, the motor is turned off and the field is remained without residual heat, thermal drift, or mechanical vibration during the measurement time. Before any measurement, sharp MFM tips are magnetized by rare earth permanent magnets.

3.2. Structural characterization of materials

3.2.1. Characterization of materials with the TEM

In Transmission Electron Microscopy (TEM) a monochromatic beam of electrons is accelerated through a potential of 40 to 100 kilovolts (kV) and passed through a strong magnetic field that acts as a lens [69]. Then this beam is transmitted through an ultra-thin sample and it interacts with the material while passing through. An image is formed due to the interaction of the electrons transmitted through the material which is magnified, focused and detected by a sensor such as a CCD camera. The resolution of a modern TEM

is about 0.2 nm which is the typical separation between two atoms in a solid. The TEM can magnify a specimen 1,000,000 times. Figure shown schematic diagram of a TEM.

A TEM is constituted of three different types of lenses. There are two to three condenser lenses which focus the electron beam on the sample. To form the diffraction in the back focal plane and the image of the sample an objective lens is used. Some intermediate lenses are used to magnify the diffraction pattern or the image on the screen.
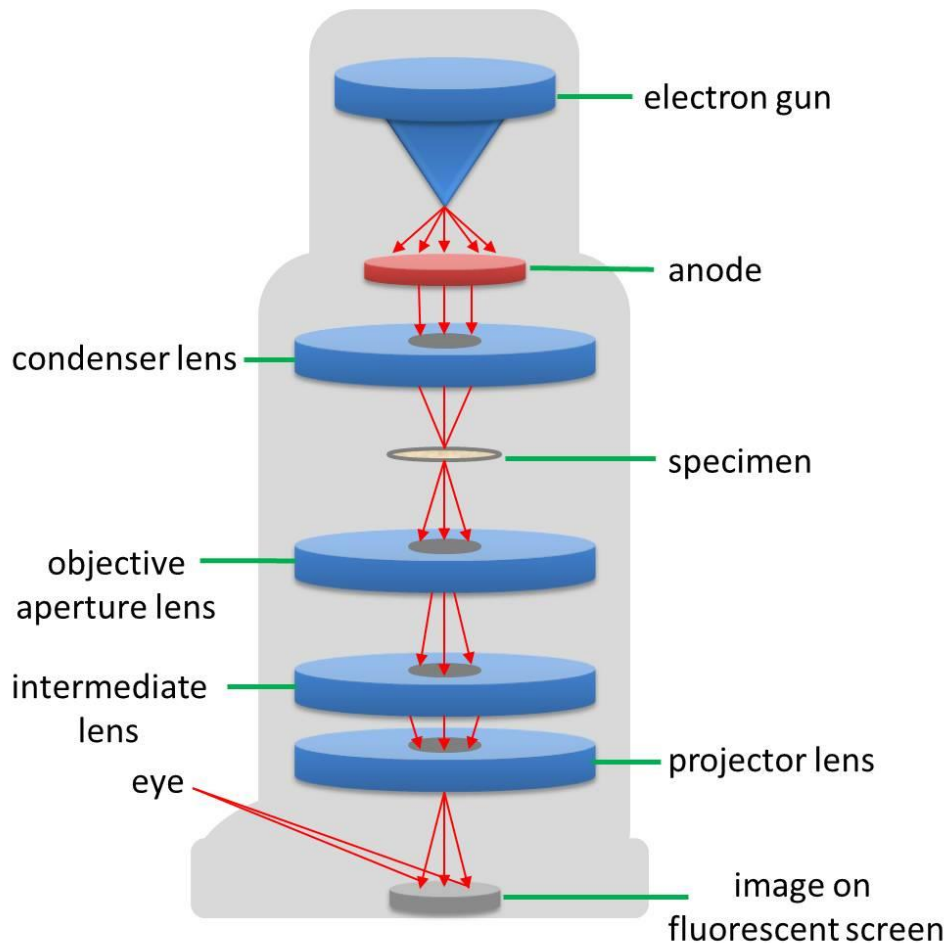
Fig. 3.6. Schematic diagram of TEM

An amplitude contrasted image is obtained where the contrast depends on the sample thickness and chemical composition. To select the transmitted beam or diffracted beam an objective diaphragm is placed in the back focal plane. The crystalline parts of the sample

appear dark and the amorphous parts appear bright in Bragg orientation. This imaging method is called *bright field imaging* mode. If there are multiple diffractions from different phases they can be differentiated by selecting one of its diffracted beams and avoiding off axis aberrations using the objective lens. This imaging method is known as *dark field imaging.*

An amplitude contrasted image is obtained where the contrast depends on the sample thickness and chemical compositions. To select the transmitted beam or diffracted beam an objective diaphragm is placed in the back focal plane. The crystalline parts of the sample appear dark and the amorphous parts appear bright in Bragg orientation. This imaging method is called *bright field imaging* mode. If there are multiple diffractions from different phases they can be differentiated by selecting one of its diffracted beams and avoiding off axis aberrations using the objective lens. This imaging method is known as *dark field imaging.*

.

Fig. 3.7. TEM instrument for micro structural analysis of materials

3.2.2. Characterization of materials with the Electron Energy Loss Spectroscopy (EELS)

Electron Energy Loss Spectroscopy (EELS) is a very powerful technique to provide chemical and electronic information from particular areas of the sample. In the analysis of EELS the energy distribution of the electrons which have passed through a thin sample with inelastic collision is measured. Material information can be obtained by two different approaches. In the first approach EELS is combined with a scanning transmission electron microscope (STEM) where the electron probe is scanned across a selected sample area and an EELS spectrum is collected point by point across the scan and a Spectrum Image (SI) is obtained. In the second approach Energy Filtering Transmission Electron Microscopy (EFTEM) is used. In EFTEM a special spectrometer is used which has the capability to filter the energy of the electrons which interacted with the specimen. Thus images of two dimensional distribution of a particular element is obtained by concentrating on a particular ionization edge is obtained.
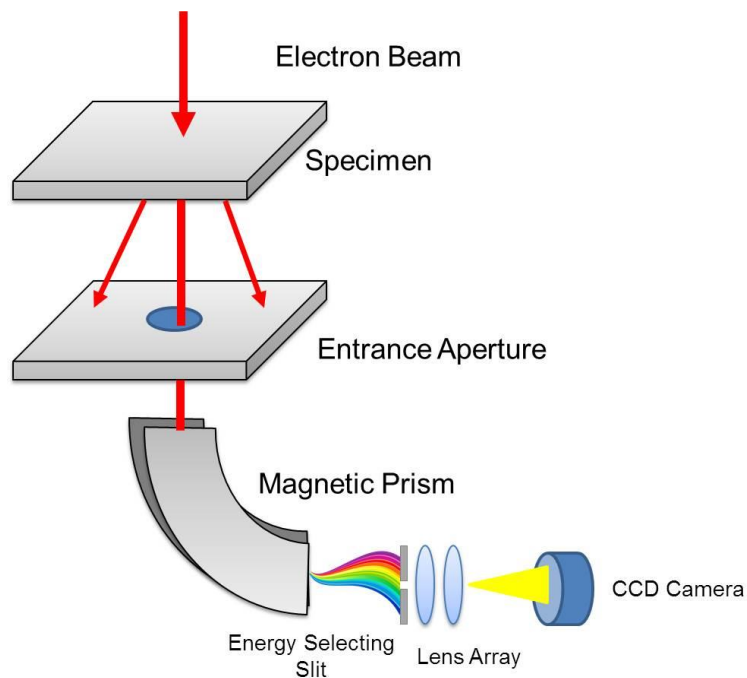
Fig.3.8. Schematic Diagram of EELS

3.2.3. Characterization of materials with the SEM

By a scanning electron microcopy an image of three-dimensional objects can be interpreted by scanning a very narrow electron beam across the sample surface. The main components of a typical SEM are electron column, vacuum system, scanning system, detector, and electronics controls [70]. The electron column of the SEM consists of an electron gun which generates free electrons and accelerates then to energies in the range 1-40 keV and two or more electromagnetic lenses to probe small, focused electron on the specimen. For this operation high vacuum is required. The purpose of the electron lenses is to create a small, focused electron to probe on the specimen. Most SEMs can generate an electron beam with spot size less than 10 nm with probe diameter in the range of 1 nm to 1 µm and probe current pA to µA. The surface of the specimen emits signal in the form of electromagnetic radiation due to accelerated electrons. There are different kinds of signals are produced due to the electron's interaction with the sample such as secondary electrons, back scattered electron, characteristic X-rays, Auger electrons and cathadoluminescence. Characteristic X-rays are used to determine the chemical composition of the elements in the sample.
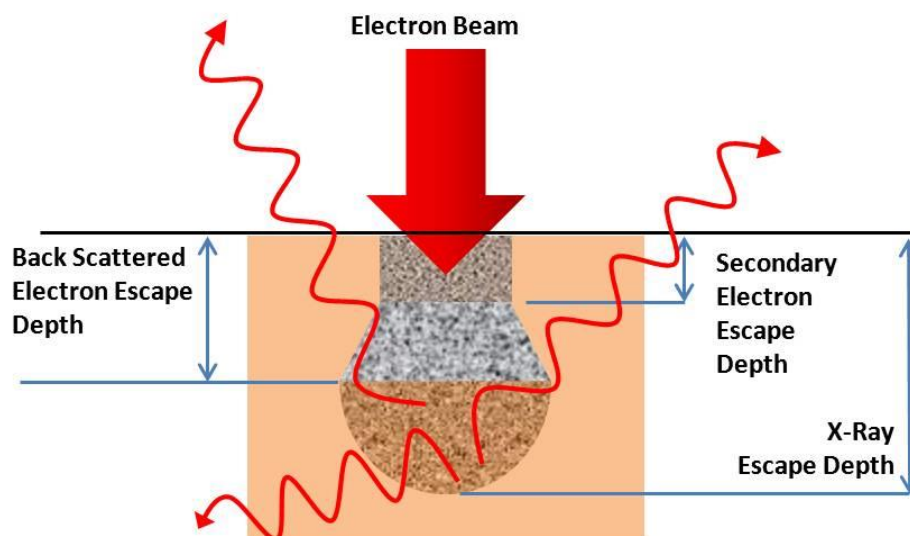
Fig. 3.9. Principle of scanning electron microscopy (SEM)

The electron beam is rastered from top to bottom and left to right. There is a correlation between the rastering pattern of the specimen and the rastering pattern to produce the image on the monitor. In order to obtain high resolution images users need to adjust the probe diameter to the imaging scale of interest, contrast, appropriate probe current and scan rate settings. Since the SEM is operated under high vacuum the specimens should be
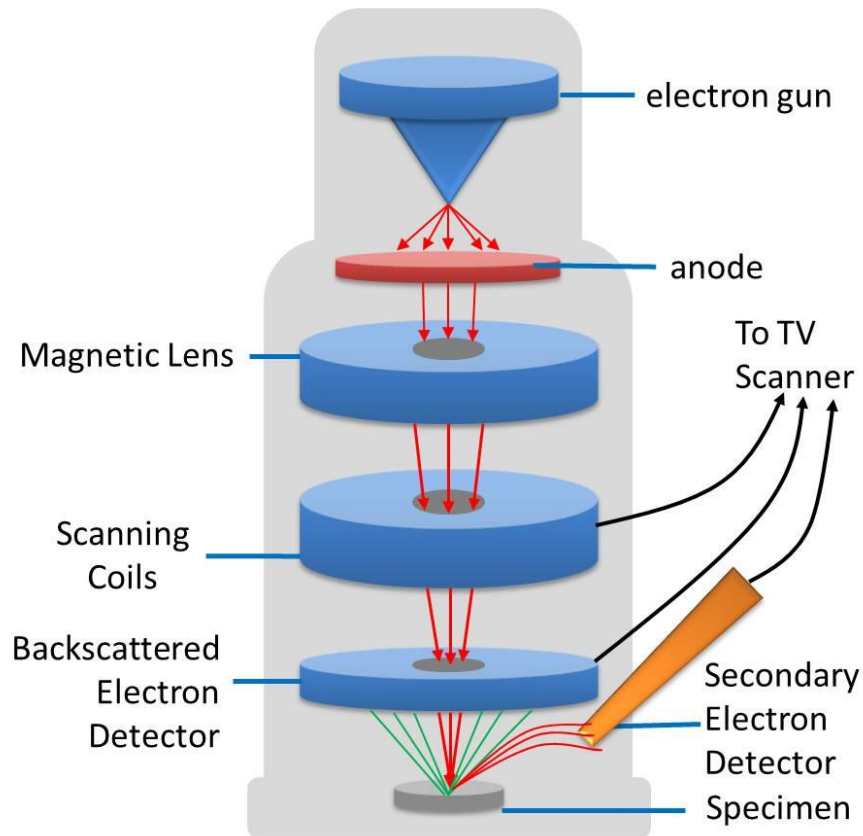
Fig. 3.10. Schematic diagram of SEM

compatible with high vacuum (~ 10^{-5} mbar). The materials containing liquids and other volatile components cannot be imaged directly. Also fine powder samples need to be properly fixed on holder substrate so that they will not contaminate the high vacuum system and SEM chamber. It's always difficult to image non-conductive materials due to charging effect. They need to be attached to a conductive specimen holder (carbon substrate/ copper tape) or coated with a very thin conductive film by sputtering or evaporating metal (Au, Pt, Pd, their alloys) or carbon.

3.2.4. Characterization of materials with the X-Ray Diffraction (XRD)

X-ray diffraction (XRD) is one of the most important non-destructive methods to analyze crystalline structure and chemical compositions of different kind of materials [71]. XRD technique is based on the Debye-Scherrer method. X-rays are focused on powder or crystalline samples fixed on the axis of the spectrometer are diffracted by every possible crystalline orientation of the sample. The changes in the diffraction of X-ray intensities are measured, recorded in the three dimensional reciprocal space and plottedonto a single dimension against the rotation angles of the sample. The result is called the X-ray diffraction pattern of the material. The result is described in the three dimensional space with reciprocal axes x*,y* and z* or alternatively by spherical coordinates system q, φ*,
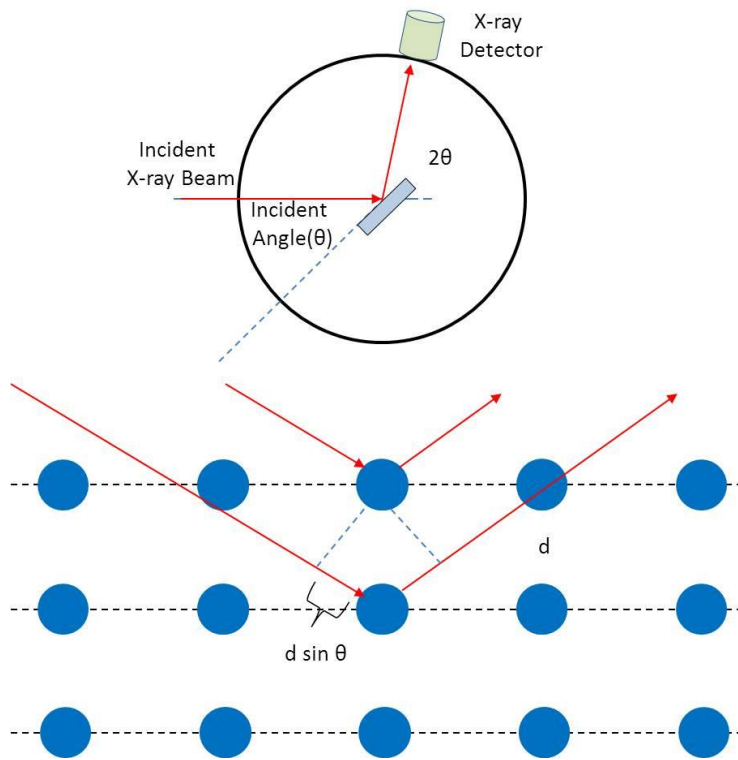
Fig. 3.11. Schismatic diagram of operating principle of X-Ray Diffraction (XRD) mechanism.

χ*. The Debye-Scherrer method averages the scanned data over φ* and χ*.'q'becomes an important measurable quantity and crystal structure of the sample is determined by it.

Effects of texturing and true randomness can be eliminated by rotating the sample orientation. The graph obtained by scanning is called diffractogram where the diffracted intensity is plotted as function either of the scattering angle 2θ or as a function of the scattering vector q. The diffractogram is a unique "fingerprint" of materials from which one can analyze unknown materials and characterize them by comparing with diffractogram to known standards databases.

Fig. 3.12. Image of PANalytical X'Pert Pro MPD X-ray Diffractometer (XRD) used for structural characterization of the materials.

3.2.5. Focused Ion Beam

Focused Ion Beam (FIB) technique is used to deposit materials with a resolution on the order of typically square microns, for the preparation of transmission electron microscopy

(TEM) specimens, etc. [72] A FIB can be used to image as sample by column of focused ions similar to SEM where column of electron is used. In FIB instrument an ion beam is focused to create specimen image. The intensity of the secondary ions produced at the raster position on the surfaceare detected and used to create an image of the specimen. By FIB sample specimens can be imaged with magnifications up to ∽100 000 times with a very good depth of field. The operation of a FIB typically based on liquid metal ion source (LMIS) where a reservoir of gallium (Ga) source is positioned with a sharp Tungsten (W) needle.
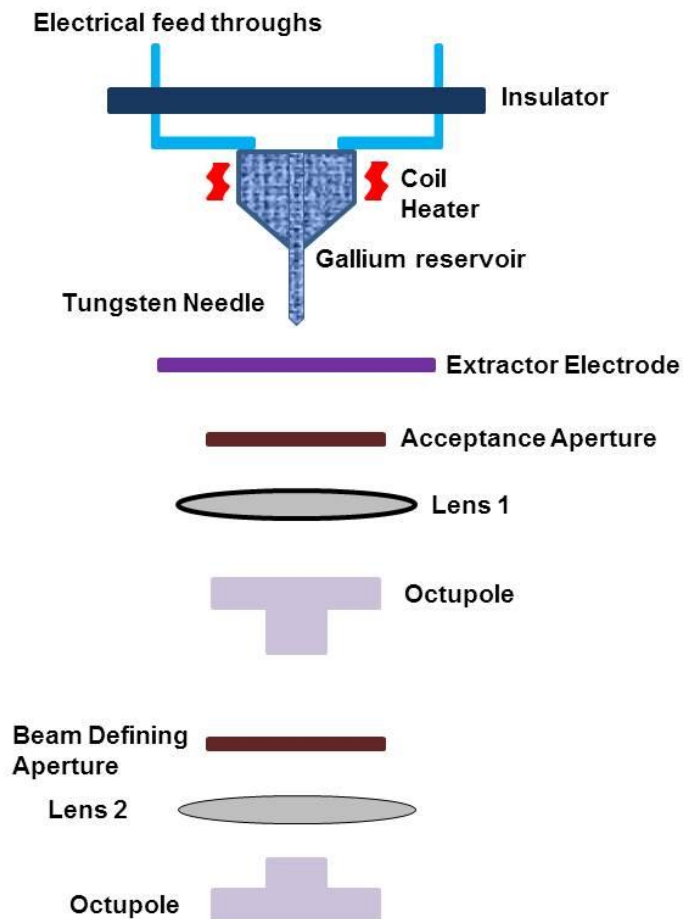
Fig. 3.13. A schematic diagram of the LMIS and FIB column

The Ga flows to the tip of W needle. A sharp cone of Ga whose radius is around 5–10 nm is generated by a high extraction field (>108 V/cm). As a result of field ionization and post-ionization the ions are emitted and then accelerated down the target FIB column. Ga ions

are used at a high power for milling and at a low power for imaging any sample. Ga is used as FIB material due its low melting point and Ga can be focused to a very fine probe size (<10 nm in diameter). FIB is typically operated with an accelerating voltage between 5 - 50 keV and from tens of pA to several nA corresponding to a beam diameter of ᴗ5 nm to ᴗ0.5 µm. FIB and SEM systems are generally integrated together into a single instrument which generates electron beam and ion beam simultaneously. The electron beam is used for imaging at much higher resolution without milling the surface as ion beam does. The sample is placed at the intersection point of electron beam.
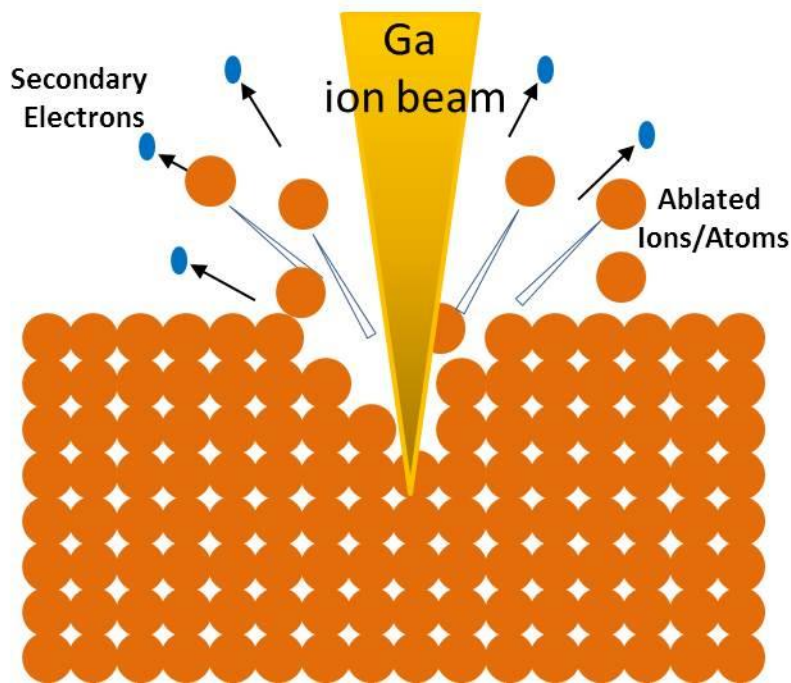
Fig. 3.14. Schematic illustration of the operating principle of FIB

4. Chapter - Micromagnetic Simulations

4.1. Introduction

In this chapter the technique of micromagnetic simulation has been discussed. The theoretical framework has been explained for the simulated results which have been incorporated in chapter 5. Further the advantages and limitation of micromagnetic simulation technique have also been explained.

4.2. Micromagnetic Theory

Presently there are different computational techniques available to model magnetic phenomena of materials and their associated parameters. The micromagnetic modelling predicts the behaviour of magnetic materials on the length scale of nano-metre to micrometre by magnetization reversal process. When an external magnetic field is applied to a sample the individual atoms try to align at a particular direction to minimize the energy of the system. Depending on the material and sample structure energy configuration of the system varies. Micromagnetic simulation method models all possible magnetic interaction within the system and fully demonstrates the magnetic domain landscape's evolution with time. Micromagneic simulation is one level above atomic simulation used to describe internal magnetic structure of a system.

4.3. Energy terms in micromagnetic simulation

Since micromagnetic simmulations is based on the magnetic interaction of individual magnetic moments, a continuous magnetization M is used to approximate the minimum energy.

i. Exchange energy:

One of the fundamental phenomenons of magnetism where individual atomic magnetic moments try to align all other neighboring atomic magnetic moments within a material is known as the exchange interaction (Aharoni, 2000). [73] The energy associated with this

magnetic interaction is called exchange energy. The exchange energy between two neighboring magnetic moments μ_i and μ_j is usually described by

$$\varepsilon_{ex}^{i,j} = -J\, S_i S_j$$

Equation 4.1

Where J is the exchange integral originates from the overlap of wave function of two electrons.

$$\varepsilon_{ex} = \frac{1}{2} \sum_i \sum_{j \in N_i} \varepsilon_{ex}^{i,j}$$

Equation 4.2

Where, N_i is the nearest neighbour i.

ii.   Anisotropy Energy

Magnetic anisotropy is a dependence of magnetic energy level within a system to the direction of magnetism of same system. If the magnetic moments in a material self-oriented towards one particular direction then the material is said to have uniaxial anisotropy, the direction is called easy axis and the perpendicular direction is called the hard direction. If the magnetization prefers to orient towards many particular directions, then the material has multiple easy and hard axes and it possesses different anisotropy symmetry (see figure 4.1). Cubic crystals such as iron and nickel have cubic anisotropy symmetry (Aharoni, 2000, p86) [73].This type of anisotropies is form of magnetocrystalline anisotropy which is attributed to spin-orbit coupling within the material arise from the crystalline structure of the material.

iron   nickel
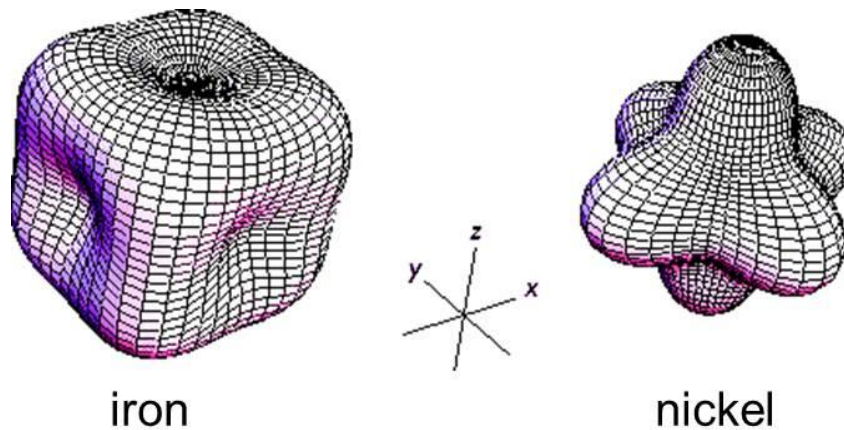
Fig. 4.1. Normalised cubic anisotropy energy surfaces $\omega_c(\theta,\phi)$. The different shapes of the surfaces are a reflection of the sign of K_1 (O'Handley, 1999). [Ref: 74]

iii.   Zeeman energy

When an external magnetic field (H) is applied to magnetic moment (μ) energy supplied by the external field induces the rotation of internal magnetization of material by harmonisation of the directions of internal and internal fields to minimization of Zeeman energy:

$$\varepsilon^i_{Ze} = -\mu_0 \mu_i . H_i$$ Equation 4.3

Where μ_i and H_i are the magnetization of individual magnetic moment due to the externally applied magnetic field on it.

The Zeeman energy reaches a minimum when all the magnetic moments are aligned in a particular direction due to the applied field.

iv.   Dipolar energy

Dipolar energy often called magnetostatic or demagnetising energy associated with the magnetic flux lines is the resultant energy due to the internal interaction of magnetic moments. The dipolar energy for two magnetic moments $\mu_{i.}$ and μ_j positioned at r_i and r_j can be represented as:

$$\varepsilon^{i,j}_{dipole} = \mu_0 \left(\frac{\mu_i.\mu_j}{|r_{ij}|^3} - \frac{3(\mu_{ij}.\mu_{ij}).(\mu_j.\mu_{ij})}{|r_{ij}|^5} \right)$$ Equation 4.4

Where $r_{ij} = r_i\text{-}r_j$

In the presence of external magnetic field a demagnetization field $\mathbf{H}_{de}(\mathbf{r})$ is created in the sample. The dipolar energy can be represented for a continuous media:

$$\varepsilon_{di} = -\mu_0 \int_v \mathbf{H}_{de}(\mathbf{r}).\mathbf{M}(\mathbf{r})d^3r$$ Equation 4.5

4.4.   Landau Lifshiftz Gilbert Equation

An important differential micromagnetic equation to describe the precession towards equilibrium magnetization was derived by Landau and Lifshitz (1935). Later Gilbert (1955) modified the equation adding an extra damping term which leads to the Landau-Lifshitz-

Gilbert (LLG) equation. Due to the rapidly-increased processing capability of modern computers, there has been of huge interest in the field of computational micromagnetic simulation to understand magnetic configuration. The LLG equation which is a fundamental part of time-dependent computational micromagnetics is used to define magnetization towords equilibrium. The OOMMF simulation software developed by Donahue and Porter in 1999 uses the Landau and Lifshitz form [79]:

$$\frac{d\boldsymbol{M}(r,t)}{dt} = -|\bar{\gamma}|\boldsymbol{M}(r,t) \times \boldsymbol{H}_{eff}\big(\boldsymbol{M}(r,t)\big) - \frac{|\bar{\gamma}|\alpha}{M_s}\boldsymbol{M}(r,t) \times \big(\boldsymbol{M}(r,t) \times \boldsymbol{H}_{eff}\big(\boldsymbol{M}(r,t)\big)\big)$$

Equation 4.6

Which is written in simplified form

$$\frac{d\boldsymbol{M}}{dt} = -|\bar{\gamma}|\boldsymbol{M} \times \boldsymbol{H}_{eff} - \frac{|\bar{\gamma}|\alpha}{M_s}\boldsymbol{M} \times (\boldsymbol{M}\mathrm{X}\boldsymbol{H}_{eff})$$

Equation 4.7

Where M is the magnetization, γ is gyromagnetic ratio (constant), $\boldsymbol{H}_{eff}$ is effective field and α is the Landau and Lifshitz phenomenological damping parameter [75].

$$\boldsymbol{H}_{eff} = \boldsymbol{H}_{efexf} + \boldsymbol{H}_{an} + \boldsymbol{H}_{msat} + \boldsymbol{H}_{ext}$$

Equation 4.8

Where
$\boldsymbol{H}_{ex}$: exchange field
$\boldsymbol{H}_{an}$: anisotropy field
$\boldsymbol{H}_{msat}$: magnetostatic field
$\boldsymbol{H}_{ext}$: external field
If one assumes $\gamma=(1+\alpha^2)\bar{\gamma}$
Then the equation can be written in mathematical equivalent form

$$\frac{d\boldsymbol{M}}{dt} = -|\bar{\gamma}|\boldsymbol{M} \times \boldsymbol{H}_{eff} - \frac{\alpha}{M_s}\boldsymbol{M} \times \left(\boldsymbol{M} \times \frac{d\boldsymbol{M}}{dt}\right)$$

Equation 4.9
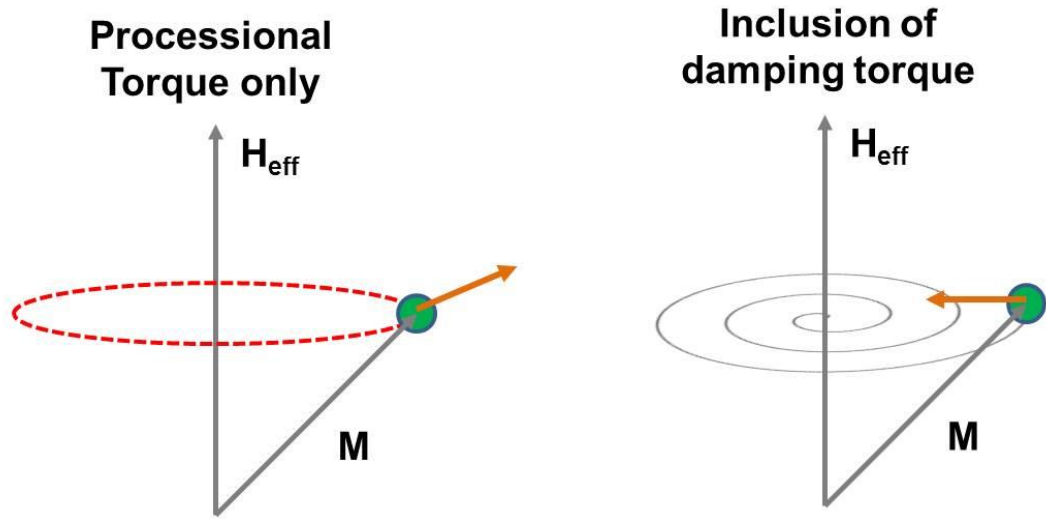
Fig. 4.2. Schematic illustration the action of 1st term (left) which induces motion of magnetization (M) about the effective field and 2nd term is schematic to illustrate of damped magnetic moment (M) in the presence of magnetic field (Heff).

The first term in the equation describes the precession of the magnetization vector (M) about the effective field (H_{eff}) where the angular frequency is equal to the Larmor frequency (w_l) and angle between the magnetization and effective field remains constant.

The magnetization decay over time due to the loss of eddy currents, spin scattering, diffusion and sample imperfections. To estimate this intrinsic loss a phenomelogical damping parameter α was introduced by Gilbert in 1955.The damping torque allows the magnetization to align along externally applied field.

4.5. Length Scale

In micromagnetic simulation a particular geometry isdiscretized into lots of smaller homogeneously magnetized cuboidal cells so that finite difference method can be used. Inside this cellular domain all of the atomic magnetic moments are defined to response as a single particle in simulation. At an atomic length scale the exchange interaction which is most significant energy term is responsible for the alignment of magnetic momentshomogeneously. These small cells which represent a certain amount of magnetic

material can then be used to perform the simulation. For micromagnetic simulation a smaller cell size is more desirable, particularly when there is curved surface in the sample geometry.

The exchange length is a length scale over which the magnetization direction does not change significantly. Due to the energy minimization of magnetostatic energy sample is broken into multiple domains with different magnetisation directions. In a coarse mesh micromagnetic software cannot resolve the exchange length properly and independent domains will not form correctly. Hence, the magnetisation can change direction over one domain wall width as given by following equation:

$$\delta_B = \pi \sqrt{\frac{A}{K}} \qquad\qquad \text{Equation 4.10}$$

The exchange length is calculated by considering (Seberino and Bertram, 2001, Kronmüller and Fähnle, 2003)[76, 77]:

$$\lambda_{ex} \sqrt{\frac{A}{\frac{1}{2}\mu_0 M_s^2}} \qquad\qquad \text{Equation 4.11}$$

Where A is the exchange energy, μ_0 is the magnetic constant and M_S is the magnetisation, μ_0 the magnetic constant. Therefor exchange length λ_{ex} gives us a quantitative assumption of mesh resolution required for micromagnetic simulation.
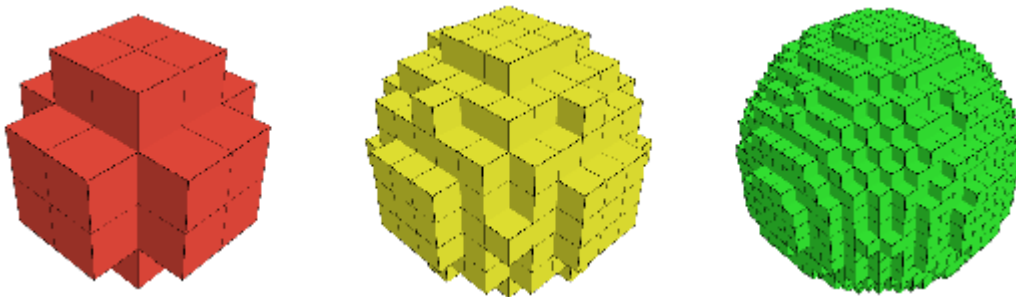
Fig.4.3. The effect of cell size and number of cell for a sample of sphere shape. As the cell size is reduced the 'model' gives much more accurate 'spherical' representation and accuracy of the simulation result is also increased. [Ref: Richard Boardman's PhD thesis, University of Southampton][Ref: 78]

In general one equation of motion is solved for each cell. By reducing the cell size the number of cell is rapidly increased and simultaneously the computational overhead is also increased. The accuracy of simulation is also increased with the increment of number of cells shown in Figure 4.3. The demagnetization field H_d at each cell depends on the magnetization distribution over the entire mesh due to external applied field.

4.6.   The Object Oriented MicroMagnetic Framework (OOMMF)

In micromagnetic simulation a set of partial differential equations are repetitively solved. For the systems where static metastable magnetisation state is considered can be simply relaxed by defining some initial magnetisation configuration, generally homogeneous or random. Then the Landau-Lifshitz-Gilbert equation is used as the Finite Differentiate (FD) method, opposed to Finite Element (FE) method to iterate the system until the rate of change of magnetisation goes below a certain threshold. The LLG theory which is difficult to solve analytically is numerically solved over time and leads to a set of differential equations. To solve that freely available Object Oriented Micromagnetic Framework (OOMMF) program based on FD method is used. [79]OOMMF was developed by Donahue and Porter in 1999 and provided by the National Institute of Standards and Technology (NIST), an agency of the U.S. Department of Commerce [79]. OOMMF has been exclusively used for all micromagnetic simulation for this thesis. To run OOMMF Tcl/Tk package is also required (Ball, 1999, Flynt, 1999, Raines and Tranter, 1999, Smith, 2000, Welch, 1999). There are few computational issues involved with OOMMF simulation. OOMMF consumes approximately one kilobyte of RAM. The simulation packagewhich must be loaded into RAM itself requires certain amount of RAM and creates a fixed overhead. Figure 4.4 shows the amount of memory (RAM) required for simulation as function cell geometry.

The first stage in the OOMMF simulation process is to define the magnetic structure to be solved. This is done by creating a MIF file which contains the material parameters, defines the structural geometry. The experimental parameters over which the simulation runs also defined in MIF file. It is essential to use accurate material parameters as inputs which are

representative of the material under investigation by micromagnetic simulation so that it can provide accurate and physically meaningful results.
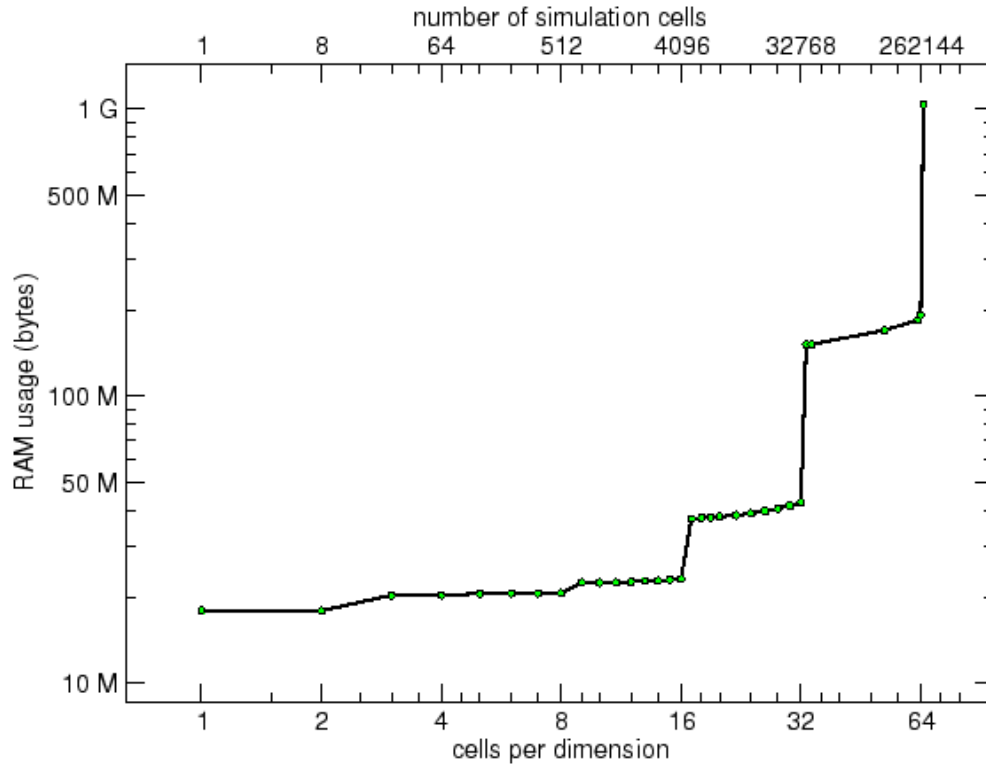
Fig.4.4. The memory required for OOMMF simulation as a function of the number of discrete simulation cells in three-dimensional geometry. [Ref: 71]

Table 3. Magnetic properties of some common ferromagnetic materials

Material	Exchange Energy A (J/m)	Magnetisation Ms(A/m)	Anisotropy $K_1(J/m^3)$	Exchange Length λ_{ex} (nm)
Nickel	9×10^{-12}	4.9×10^5	-5.7×10^3	7.72
Iron	2.1×10^{-13}	1.7×10^6	4.8×10^4	3.4
Cobalt	3.0×10^{-13}	1.4×10^6	5.2×10^5	4.94
Supermalloy	1.05×10^{-13}	8.0×10^5	0	5.11
Permalloy	1.30×10^{-13}	1.11×10^6	0	2.76

Ms= Saturation magnetisation in A/m

K_1=First anisotropy constant in J/m^3, i.e. by first order approximation the uniaxial anisotropy is given by $K_1 V sin^2\theta$ and $K1 = \frac{\mu_0 M_S H_k}{2}$

A=$3\frac{k_B T_c}{aZ}$; k_B is Boltzman's Constant, T_c is the Curie temperature, a is lattice constant and z is number of nearest neighbouring atoms.

5 Chapter – Manipulation of magnetic anisotropy-shape/dipolar

5.1. Introduction

One of the most significant challenges in micromagnetic devices is to configure magnetization directions of patterned ferromagnetic films. In polycrystalline materials this is mainly determined by external environmental effects or geometry [80] due to insufficient long range microscopic crystalline order. Hence, applications of these materials are widely based on the ability to control the magnetic anisotropy resulting out of spin configuration based on pattern geometry. In recent years, this has been demonstrated for patterned, isolated magnetic structures [81-84] and structured continuous magnetic films [85]. Such kinds of control open up opportunities for potential applications such as spintronic devices, magnetic random access memory (MRAM)[86] high density patterned information storage media[86,87], and high precision ultra small magnetic field sensors[88]. Due to fundamental reasons and potential applications, it is necessary to understand further the magnetic properties of patterned structures in reduced dimensions, while both geometry and crystal microstructure are needed to be optimised prior to configure the magnetization[89]. Subsequent investigations further reveal properties like geometrical frustration, domain wall pining, etc due to dipolar interaction based on spin configurations [90, 91]. Several methods such as ion irradiation through a mask, selective epitaxy, surface modulation [92], etc. have been studied to control the magnetization configuration in patterned structures. Among them, surface nanomodulation is preferred for its cost effectiveness and simplicity to engineer the spin configuration locally [93]. Furthermore, the optimization of magnetic parameters such as pattern geometry, film thickness, intrinsic anisotropy, and coercivity is essential to obtain a controlled anisotropy in a film by nanomodulation. Magnetostatic energy induced by strong nanomodulation forces the spins into local vortices which is unfavourable for many applications. Thus, the development of a physical model for an optimized modulation is essential to manipulate the film anisotropy.

In the present work results of anisotropy variation due to magnetic dipoles formation in nanomodulated film and detailed micromagnetic simulation study with key symmetry

features of complete nanomodulation based anisotropy in continuous ferromagnetic thin films have been discussed. Novel ways to produce different anisotropy are introduced, which have been validated by experimental evidences and analytical derivation. To determine anisotropy variation due to the magnetostatic dipole interactions we performed various magnetometry measurements combined with MFM imaging on nanomodulated continuous $Ni_{45}Fe_{55}$ film. Artificially created ordered corrugation produces controllable magnetic dipoles. However, while the external field favors such magnetic dipole alignment, interdipole magnetostatic interaction results in a variation of the effective magnetostatic energy in different directions. This effect translates into in-plane and out of plane anisotropy variation depending upon modulation geometry.

It is also demonstrated how a unique nanostrucuture of continuous ferromagnetic film can induce magnetic dipoles at sub-micron scale at pre-defined locations and play a key role to tune the global magnetic properties of the film due to magnetostatic interactions. Synthetic arrays of magnetic dipoles are tuneable at in-plane and out of plane directions and can be rotated in plane in such three dimensional modulated structure. In-plane magnetic field rotations influence magnetostatic interactions in different directions which open up a new methodology to control the various magnetic properties of a ferromagnetic thin film. Gradual formation of magnetic dipoles and their tunability have been studied in detail by MFM imaging and other magnetic measurements. It is observed that the diploes go through a transformation from metastable to stable state. The magnetostatic interaction depends on their geometrical arrangements. Thus magnetic properties of the continuous film can be varied by pattern geometry. This has been shown by experiment and micromagnetic simulation (OOMMF) in nanomodulated $Ni_{45}Fe_{55}$. It is usual that in nano pattern bigger than single magnetic domain, the dipole tries to form vortex at remanence state. Whereas this unique three dimensional structure prevents vortex formation due to strong magnetostatic interaction as a novel observation. Again this could influence the dynamic properties of the thin film. A detail analytical study of dipolar energy for our system agrees with our experimental and simulated results.

5.2. Nanomodulated Ni$_{45}$Fe$_{55}$ electrodeposited thin film

A nanomodulated conformal and uniform alloy composition of ferromagnetic Ni$_{45}$Fe$_{55}$ thin film (Fig.5.1 & 2) was prepared by an electrodeposition process [94] on patterned substrates fabricated by nanoimprint lithographyto create artificial surface roughness on electroplated thin-films.
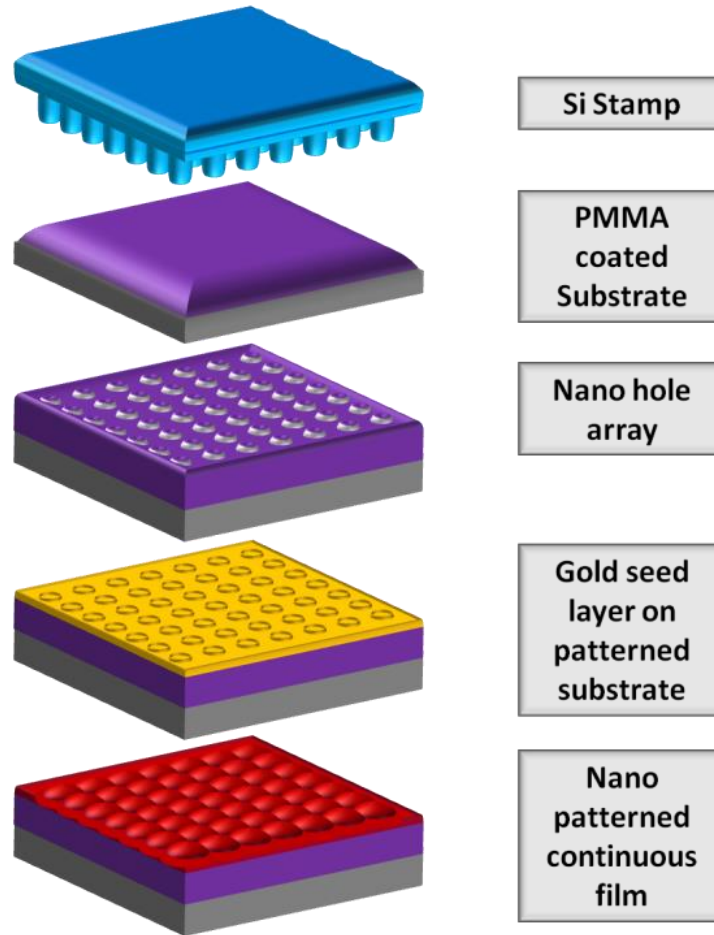
Fig.5.1. Schematic diagram of sample preparation

Nanoimprint processing was used to make the patterned substrate. A polymethylmethacrylate (PMMA, Molecular weight~230k) layer of 1μm thickness was spin-coated on a cleaned, 0.5mm thick silicon substrate and baked at 100°C for 10 minutes in air. Two different silicon stamps with 400 (D-diametre of the hole)/400 nm (S-seperation between two neighbouring holes) and 200/200nm diameter/separation were used to create

square arrays of nanoholes (Fig.5.2a). These stamps were fabricated by interference lithography and subsequent ion-reactive etching. A Self-Assembled Monolayer (SAM) of Octadecyltrichlorosilane (ODTS) was coated on the stamp to avoid any kind of adhesion with the pillar array. For multiple uses the stamps were cleaned by acetone and ethanol. The stamps were placed on the PMMA layer and heated at 160°C for 30 minutes with a pressure of 50 bars to generate an array of nanoholes with a depth of 240nm. After cooling down, the stamps were carefully removed and an array was imprinted on each substrate (Fig.5.2.a). An adhesion layer (10nm Ti) and a 150nm layer of Au were sputtered on patterned PMMA as a seed layer (Fig.5.2b). The thickness of the Au seed layer on the wall of the holes was around 25nm. A uniform $Ni_{45}Fe_{55}$ ferromagnetic film was deposited by DC electroplating on both types of pattern (Fig.5.2.c & d).
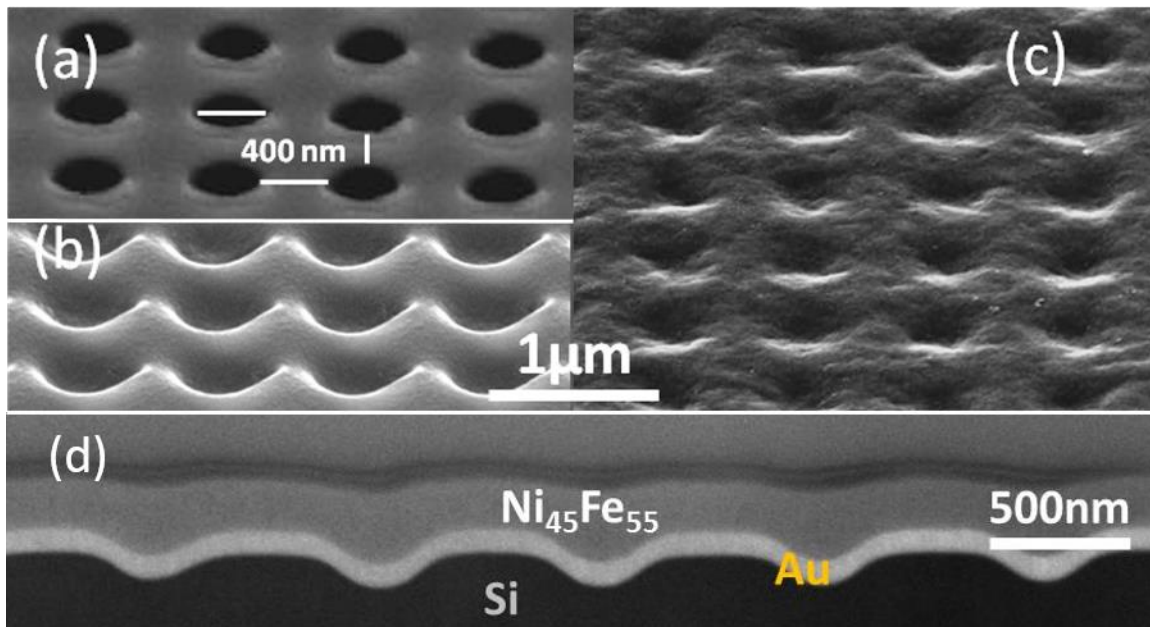
Fig.5.2. (a) SEM image of nanohole array on PMMA on Si. (b) Gold seed layer on patterned substrate, (c) Electroplated continuous Ni45Fe55 on nanomodulated substrate. (d) Cross section of the nanomodulated film.

During the electrodeposition an external magnetic field was applied at much higher level (~200 Oe) than the demagnetization field of the film to make sure it produces a uniaxial anisotropy in the deposited film along the field direction <100>.The variation of sample

thickness affects the anisotropy created by patterning. When the thickness of the sample is significantly more than the modulation amplitude then the anisotropy induced by patterning is suppressed by the uniaxial intrinsic anisotropy. Thicknesses near to the modulation amplitude give more control over the artificial anisotropy.

5.3. Magnetic measurements of anisotropy manipulation

Magnetic properties of nanopatterned films were investigated by using a hysteresis loop tracer (SHB instruments Inc., USA) and SQUID magnetometry (Quantum Design MPMS). A field range of +1000 Oe to - 1000 Oe was used to ensure saturation and to measure hysteresis loops in varying in-plane rotational angles.
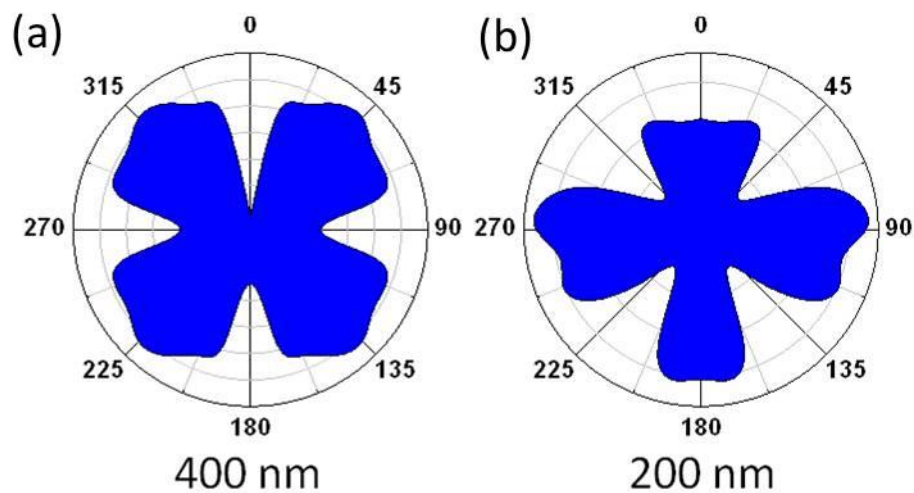
Fig.5.3. Angle dependent normalized remanant magnetization (M_r vs. θ) measured from 3D nanomodulated film with 400nm (a) and 200nm (b) element diameter respectively.

In this experiment magnetic force microscopy (MFM) imaging was done by a commercial atomic force microscope in MFM mode (VFM2-HV - Asylum Research High Voltage Variable Field Module - Version 2) and MESP-RC probes (Bruker AFM ProbesInternational). The VFM2-HV can apply static magnetic fields up to ±0.1 Tesla (~1G resolution), parallel to the sample plane. We were able to map the magnetization of

each nano size magnetic dipoles and their interaction with a ferromagnetic tip with low remanence. The low remanence tips were used to ensure that the tip magnetization do not influence the film's magnetization configuration within its own detection limit.

We observed that the remanence magnetization (M_r) and coercivity (H_c) both vary as a function of angle due to magnetic anisotropy created by nanomodulation. Since the variation in remanence (M_r) is much stronger than that in coercivity (H_c) for an ultra-soft magnetic material, we consider remanence for further discussion. In Fig.5.3.a & b normalised remanent magnetization (M_r) is plotted as a function of sample rotation angles with respect to applied in-plane field direction for two different patterns. Variation of remanent magnetization (M_r) as a function of applied field direction is small compared to the remanent magnetization (M_r). Hence the normalised angle dependent remanent magnetization [$M_r(\theta)$ /(M_{r-max}-M_{r-min})] is plotted to compare the symmetry variation. Both patterns show 4-fold symmetry whereas satellite maxima of the higher order are prominent in 400nm pattern (Fig.5.3.a).
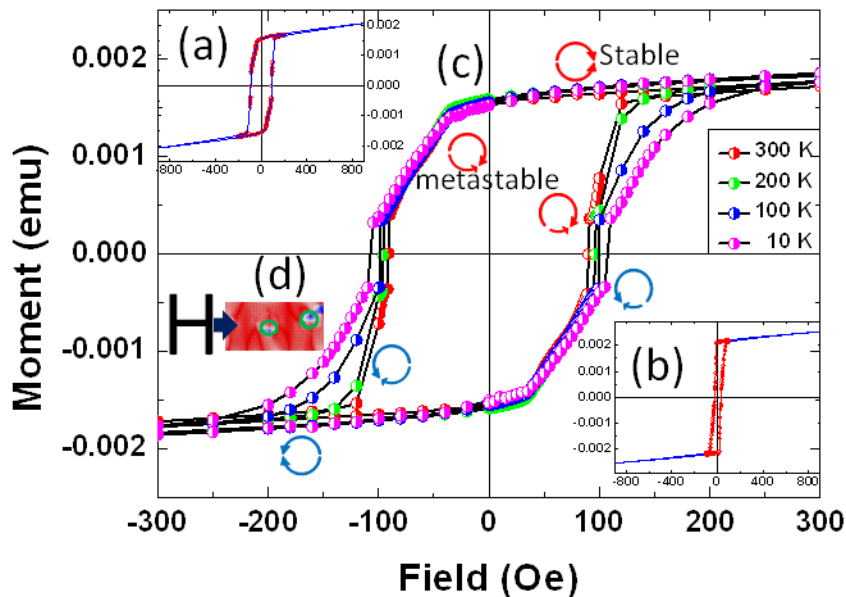
Fig.5.4. Hysteresis loop measure from thin nanomodulated sample (a-150nm and b-50nm) shows metastable state. (b) Step like MH curve (zoomed of 15nm thickness-figure a) in various temperatures shows existence of metastable dipoles throughout the temperature range. Near zero remanance the dipoles suddenly jump from positive to negative value. (d) OOMMF simulated picture of magnetization configuration near remanent shows incomplete vortex formation

The anisotropy based on nanomodulation is so strong that it could dominate film's uniaxial anisotropy. A novel phase shift is observed in 200 nm pattern (Fig5.3.b) for higher aspect ratio, whereas after gold deposition the aspect ratio diameter/separation (D/S) becomes 3:1. The reason of this phase shift has been explained later. In the case of the thickness (t) of the sample being significantly more than the modulation amplitude (A), the anisotropy induced by patterning is dominated by the uniaxial intrinsic anisotropy of the film. When sample thickness, t, ~150 nm is lower than modulation amplitude, A, (~ 240 nm) it tries to form a vortex and a step like behaviour in MH curve is visible (Fig5.4.a) due to the effect of nanomudulation . A further decrease in sample thickness (t) to ~50nm (Fig5.4.c) gives near zero remanence. The sample with thickness (t) ~ 150nm was measured at different temperatures (Fig5.4.c), which shows the existence of metastable states trough out the temperature range. It is found that the nanomodulated film requires a very high field to obtain saturation magnetization due to the formation of magnetic dipoles and their strong coupling. For the change of external magnetic field the magnetic dipole goes through a transition from saturation magnetization or stable non-hysteretic region via metastable planar region to unstable dipolar state or jumps (Fig5.4.c). At near zero fields, the remanence (M_r) suddenly jumps from positive to negative magnetization which indicates the existence of magnetic dipoles with nonzero M_r. Thus a complete vortex cannot be achieved in this unique structure. To understand the phenomena we focus on single element. For a square array-pattern of 400 nm diameter and 100 nm modulation amplitude (D/S is 1), the calculated energy densities are 0.49 x 10^4 J /m^3 and 1.33 x 10^4 J /m^3, for vortex and near single domain state respectively. Since the energy of a vortex state is less than that of a near-single-domain remanent state there should be a strong inclination to adopt vortex states in the nanomodulated continuous ferromagnetic thin films. On the other hand, it is necessary that the demagnetization processes needs to overcome the higher energy barrier to create local vortex in nanomodulated continuous ferromagnetic thin films where spins are strongly exchanged in parallel due to magnetostatic interaction. Thus these magnetostatic interactions in this patterned matrix try to resist formation of vortices which is analogous to closely-packed magnetic dots [95]. As a consequence, a near-single domain state originates at the remanence magnetisation state with an intention to become a vortex

state. To further elucidate, simulation results (Fig. 5.4-d) show that incomplete vortices exist all over the film but in very tiny amounts.

A range of samples with different thicknesses having fixed modulation amplitude (240 nm) were prepared. Thick film shows uniaxial anisotropy since dipolar anisotropy is weaker compared to uniaxial anisotropy. Very thin film shows only four fold anisotropy symmetry where dipoles are too week for higher order dipolar-interaction. Thus thickness (t) near to modulation amplitude (A) shows maximum anisotropy variation in easy and hard directions. These were investigated by micromagnetic simulation as well.

To explain these results we refer to the recently developed power law for a magnetic film with a roughness-induced demagnetizing effect $H_K \sim \tilde{N}M_S \sim A^2 / t$ ($\tilde{N}$ is demagnetizing tensor) [96]. Since the power law was derived by using a demagnetizing tensor ($\tilde{N}$) for demagnetizing field H_d in a magnetostatic phenomenon, it supports the argument that the symmetry of magnetic anisotropy comes from 3D nanomodulation, which has been shown by means of variation of remanence magnetization. The symmetry is based on alignment of the pattern induced magnetic dipoles and their magnetostatic interactions. The direction of effective dipole interaction depends on the direction of applied field (Figure 5.5).
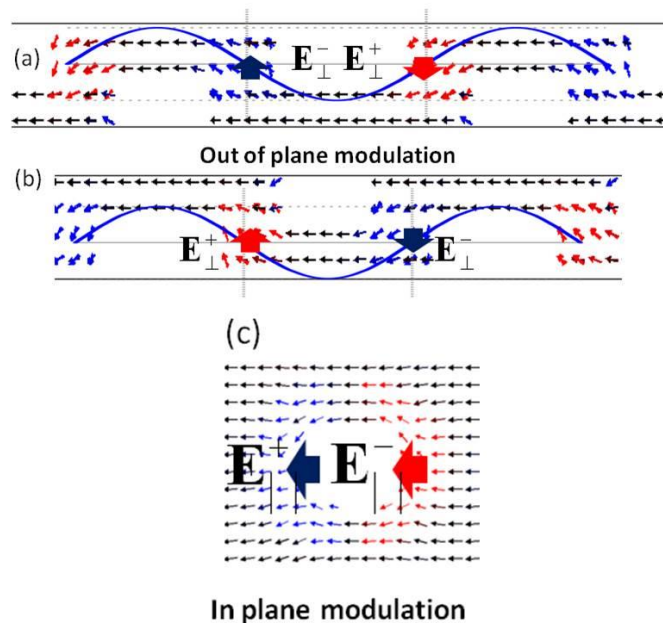
Fig. 5.5. Schematic diagram of out of plane (a-b) and in plane (c) modulation shows formation of dipoles and direction array chain of magnetostatic interactions. Modulation switches to upper layer for high aspect ratio (a) and to lower layer for low aspect ratio (b).

In the MFM image, the dipoles are aligned in <110> direction as an external field (1000 Oe) was applied in that direction before imaging. In case of an alignment in a certain direction by an external field (Fig.5.7-a) depending upon the pattern symmetry, dipoles across each patterned elements are coupled with their neighbours and the demagnetization energy decreases with an increase in remanent magnetization due to strong magnetostatic interactions. Also the linear density of the dipoles changes as a function of directional angle and hence the net dipole interaction varies. This unique three dimensional ferromagnetic nanostructure forces the microspin configuration to follow a
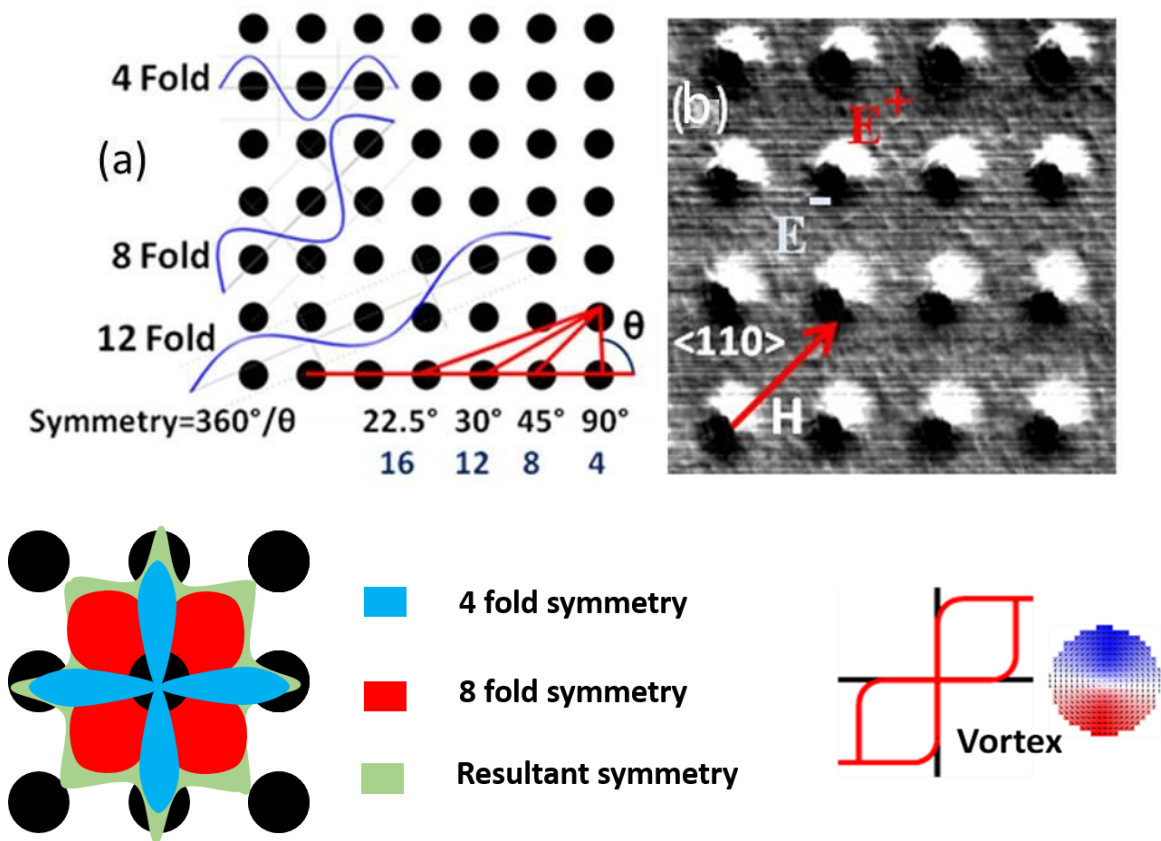
Fig.5.6. Different symmetry formation due to pattern arrangement (a). Interaction of one dipole with 1st neighbour creats 4-fold symmetry, 2nd neighbor creats 8-fold, etc. MFM phase images of dipoles (b) for externally applied field. An external field of 1000 Oe was applied in <110> direction before imaging. The images were taken at a 50nm distance from sample surface.

wave like propagation of magnetization which collectively generates in plane and out of plane dipoles (Figure 5.5.a-c). In a square array of magnetic nano structure the magnetic ordering is determined by minimization of collective magnetostatic energy whereas the magnetic anisotropy energy depends on the dipole interaction if it is strong enough to keep the magnetization after removal of applied field. Normally, the isolated nanostructure bigger than single domain, tries to form vortex (Fig.5.6) at remanence state to obtain the minimum energy state. Here the competition between two different dipoles (in plane and out of plane) and possible spin pinning between two consecutive dipoles through continuous ferromagnetic media keeps the magnetization stable at the direction of applied field and resists vortex formation. We varied the angle of applied field direction with respect to patterned array. The dipoles rotate with the rotation of applied field which is shown in Figure 5.6 a. The variation of magnetic anisotropy was investigated by measuring coersivity at different direction which shows a clear trend of four fold anisotropy symmetry (Figure 5.3) in the square array structure. This result agrees with micromagnetic simulation result. The competition between two different dipoles generates a collective metastable magnetic configuration and a step like MH curve is observed (Figure 5.4). The wave pattern creates a strong out of plane dipoles which becomes difficult to align at a particular in plane direction by a high external field. This has been observed in measured MH curve. The curve shows a prominent minor loop (Figure 5.4.c) and an unsaturated major loop (Figure 5.4.b) due to these strong out of plane dipoles. We applied a field of 1000 Oe, which is large enough to saturate $Ni_{45}Fe_{55}$ film and map the magnetization of our patterned field very carefully. Interestingly, a magnetic vortex with a single vortex core has been observed at the center of each nanopattern at high field due to the gyration motion of out of plane magnetic spins at vortex core.

5.4.   Micromagnetic simulation for anisotropy manipulation

The experimental results for nanomodulated continuous ferromagnetic thin film has further been investigated by static micromagnetic simulations which were carried out by solving the Landau-Lifshitz-Gilbert (LLG) equations (Eqn. 5.12), using Object Oriented Micromagnetic Framework (OOMMF) [79] software from NIST US.

$$\frac{\partial \vec{M}(\vec{r},t)}{\partial t} = \left|\gamma\right| \vec{M}(\vec{r},t) \times H_{eff}(\vec{r},t) + \alpha/M_S \left[\vec{M}(\vec{r},t) \times \frac{\partial \vec{M}(\vec{r},t)}{\partial t} \right]$$

$$H_{eff}(\vec{r},t) = -\left(\frac{1}{\mu_0}\right)\left[\frac{\partial E}{\partial \vec{M}(\vec{r},t)}\right]$$

Equation 5.1

Square and equilateral triangle arrays were made of 7 X 7 circular elements (Fig. 5.7-a) as this is the minimum number of elements required to include long range magnetostatic interaction effects in a large scale [97]. The real topographically patterned nanostructured film was implemented by creating two consecutive atlases or 3D geometrical spaces used for OOMMF simulation. In Figure 5.7 the side view of an ideal film is shown. To avoid the complexity of simulation the nanopattern has been simplified to square wave (Fig. 5.7). To simulate for such films, ideally unit cell with low dimension is required which will consider atomic interactions. This is unfavourable for mictomagnetic simulation. If the cell size is reduced too much, the computer will need huge time to complete one. Hence, an approximation close to the real system is required for such micromagnetic simulation. To simplify the simulation and save simulation time we have considered much simplified structure than the real nanomodulated film. Typical side view of simulated BIT maps is shown. The whole structure was modelled by creating two layers, top layer and the bottom layer, top-bottom view (Figure 5.7). 65% area of the whole atlas area was patterned
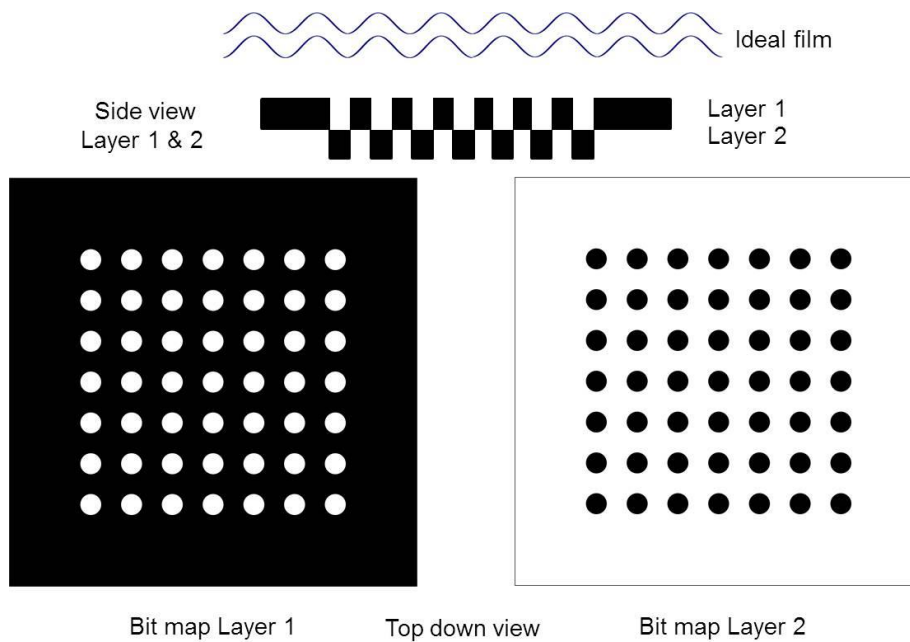
Fig.5.7. Bit map image used for OOMMF simulation

to avoid edge effect in the simulation. For all simulation, a standard MIF was used. For the area of 8μm×8μm and thickness 200nm a mesh size of 50 nm (cell size 50nm × 50nm × 50nm) produces 30000 cells. The pattern geometry and number of cells were kept constant but the diameter (D) of the hole was varied. Accordingly atlas size and cell size were varied keeping number of cell constant. For simulation, the cubic cells are used and minimum length of the cubic cell was taken as 6.25 nm, which is nearly equal to exchange length $(A/2\pi)^{1/2}M$, where A is exchange constant and M is magnetization. The total number of cells ($102400 \sim 10^5$) was constant for all simulations to maintain the same geometrical accuracy. Cell dimensions were varied accordingly depending upon simulation parameters. The
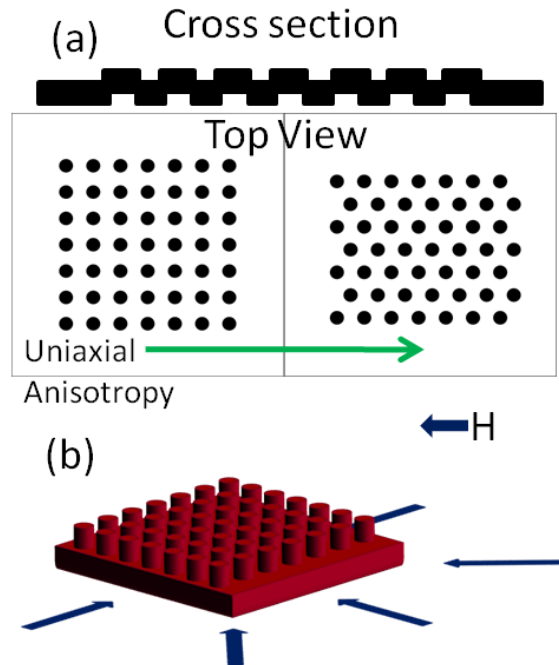
Fig. 5.8. (a) Cross section and top view of patterned film used for simulation. (b) Schematic diagram of rotation of H_{ext} in x-y plane. Uniaxial anisotropy in <100> direction of the pattern is considered for all simulation.

magnetic parameters for OOMMF simulation are required as inputs. We assumed typical material parameters for $Ni_{45}Fe_{55}$: $4\pi M_S = 1.2 \times 10^6$ A/m, $A = 6.47 \times 10^{-12}$ J /m, and anisotropy constant: $K = 600$ J /m^3 in the <100> direction of the pattern (Fig. 5.8). The global external

magnetic field H_{ext} was applied in the <100> direction of the whole atlas. To study rotational symmetry we only rotated the pattern (Fig. 5.8-b & Fig.5.9) with respect to whole atlas background and applied a magnetic field to confirm that only the effect of the patterned area was taken into account. In these calculations, we did not include the simulated results of angles near $0^{°}$, 90º and its equivalent angles for square pattern to avoid artificial degeneracy arising in simulations, when H_{ext} is exactly parallel to the <100> and <010> direction. The external applied magnetic field H_{ext} was increased from 0 Oe to 400 Oe on the film to ensure saturated static magnetization (H_K). For single element, we simulate the structure with cell dimension 20 nm x 20 nm x 20 nm of 400nm pattern elements having 3 x 3 arrays as this is the minimum number of elements required to include short range magnetostatic interaction effect.

To investigate the anisotropy symmetry the pattern in bitmap was rotated within the whole atlas and the field was applied to <100> direction for all the cases. All the bitmap image files were created and rotated using Microsoft Power Point. The patterned structure were simulated in following angles 0˚, 5˚, 11˚, 15˚, 18˚, 23˚, 27˚, 30˚, 36˚, 40˚, 45˚, 50˚, 54˚, 60˚, 60˚, 63˚, 67˚, 72˚, 70˚, 79˚, 85˚ and 90˚. All the other angles up to 360˚ were extrapolated by assuming symmetry in square atlas. To ensure the saturation of the sample and a field of 400 Oe was applied which is much higher that the saturation field of material.
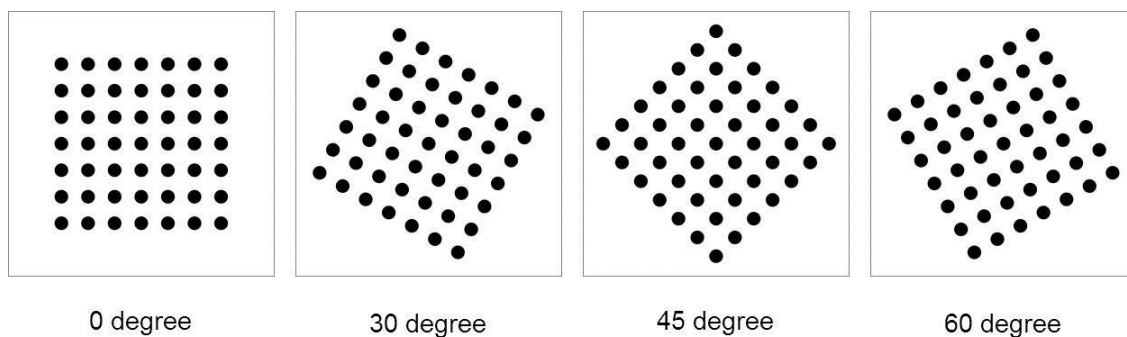
Fig.5.9. The patterned was rotated for OOMMF simulation to investigate magnetic anisotropy

The equation of energy can be written as:

$$E_t(M, H_{ext}) = \int \left[\frac{A}{M_S^2} \sum_{i=1}^{3} (\nabla M_i)^2 + f_k(M) - \frac{\mu_0}{2} M.H_d - \mu_0.M.H_{ext} \right] dv \qquad \text{Equation 5.2}$$

In OOMMF simulation the only energy term which is affected by this nanomodulation is magnetostatic energy and is proportional to H_d , where H_d is the demagnetising field. Again, H_d equals to $-N_d M$ where N_d is the demagnetising factor and M is the magnetisation. Normalised Magnetostatic Energy was calculated from OOMMF simulation output result for different rotation by following the equation and plotted as a function of angle (θ).

$$NME(\theta) = \frac{(ME@\theta^0 - ME@\theta45^0)}{(ME@0^0 - ME@\theta45^0)} \qquad \text{Equation 5.3}$$

The x and y Cartesian coordinates are extraploted using simple equations X = (1-NME) and Y = (1-NME) cos(θ), where NME= Normalised demagnetization energy. The results from simulations and related calculations are shown in the Table 4. The data then plotted in the following figure 5.10.
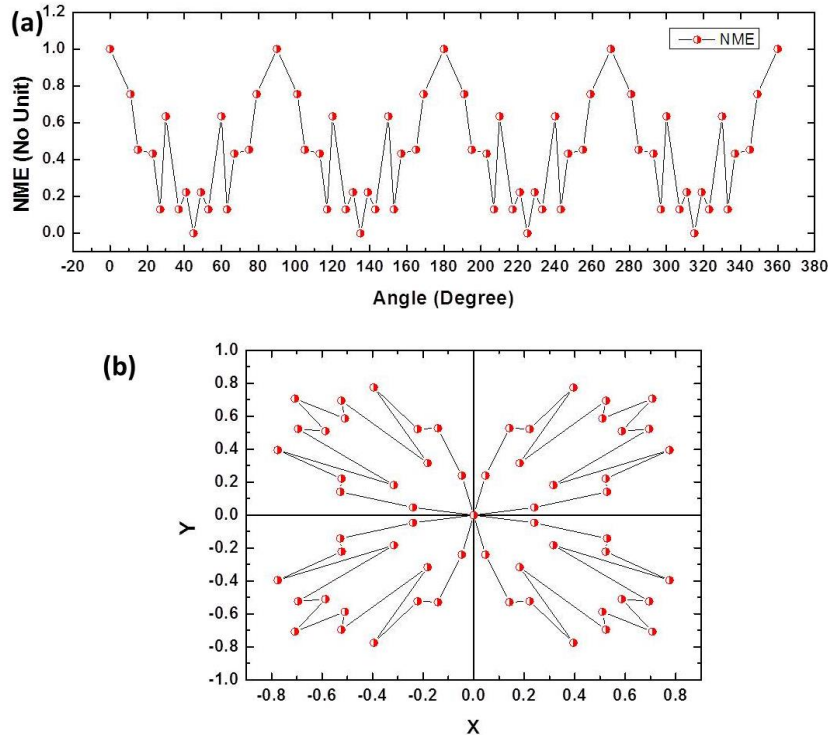
Fig.5.10. (a) Normalised demagnetization energy (NME) ploted as a function of angle, (b) X & Y component of (1-NMY) ploted.

To visualize the results of the simulation, the magnetization vector datasets were used as real time 3D output by the software package. Color contrast and spin configuration of the real-time image define the state of magnetization at the different level of samples at different stage of simulation.

Table 4: Micromagnetic simulation results

Rotation (θ in °)	Rotation (θ in rad)	Magnetostatic Energy (J)	Normalised ME (NME)	1-NME	X-value	y-value
0	0	1.56274E-13	1	0	0	0
11	0.19199	1.56043E-13	0.75581	0.24419	0.04659	0.2397
15	0.2618	1.55757E-13	0.45349	0.54651	0.14145	0.52789
23	0.40143	1.55737E-13	0.43235	0.56765	0.2218	0.52253
27	0.47124	1.55451E-13	0.13002	0.86998	0.39496	0.77516
30	0.5236	1.55929E-13	0.63531	0.36469	0.18235	0.31583
37	0.64577	1.55451E-13	0.13002	0.86998	0.52357	0.6948
41	0.71558	1.55539E-13	0.22304	0.77696	0.50973	0.58638
45	0.7854	1.55328E-13	0	1	0.70711	0.70711
49	0.85521	1.55539E-13	0.22304	0.77696	0.58638	0.50973
53	0.92502	1.55451E-13	0.13002	0.86998	0.6948	0.52357
60	1.0472	1.55929E-13	0.63531	0.36469	0.31583	0.18235
63	1.09956	1.55451E-13	0.13002	0.86998	0.77516	0.39496
67	1.16937	1.55737E-13	0.43235	0.56765	0.52253	0.2218
75	1.309	1.55757E-13	0.45349	0.54651	0.52789	0.14145
79	1.37881	1.56043E-13	0.75581	0.24419	0.2397	0.04659
90	1.5708	1.56274E-13	1	0	0	0
101	1.76278	1.56043E-13	0.75581	0.24419	0.2397	-0.04659
105	1.8326	1.55757E-13	0.45349	0.54651	0.52789	-0.14145
113	1.97222	1.55737E-13	0.43235	0.56765	0.52253	-0.2218
117	2.04204	1.55451E-13	0.13002	0.86998	0.77516	-0.39496
120	2.0944	1.55929E-13	0.63531	0.36469	0.31583	-0.18235
127	2.21657	1.55451E-13	0.13002	0.86998	0.6948	-0.52357
131	2.28638	1.55539E-13	0.22304	0.77696	0.58638	-0.50973
135	2.35619	1.55328E-13	0	1	0.70711	-0.70711
139	2.42601	1.55539E-13	0.22304	0.77696	0.50973	-0.58638
143	2.49582	1.55451E-13	0.13002	0.86998	0.52357	-0.6948
150	2.61799	1.55929E-13	0.63531	0.36469	0.18235	-0.31583
153	2.67035	1.55451E-13	0.13002	0.86998	0.39496	-0.77516
157	2.74017	1.55737E-13	0.43235	0.56765	0.2218	-0.52253
165	2.87979	1.55757E-13	0.45349	0.54651	0.14145	-0.52789

Rotation (θ in $^\circ$)	Rotation (θ in rad)	Magnetostatic Energy (J)	Normalised ME (NME)	1-NME	X-value	y-value
169	2.94961	1.56043E-13	0.75581	0.24419	0.04659	-0.2397
180	3.14159	1.56274E-13	1	0	0	0
191	3.33358	1.56043E-13	0.75581	0.24419	-0.04659	-0.2397
195	3.40339	1.55757E-13	0.45349	0.54651	-0.14145	-0.52789
203	3.54302	1.55737E-13	0.43235	0.56765	-0.2218	-0.52253
207	3.61283	1.55451E-13	0.13002	0.86998	-0.39496	-0.77516
210	3.66519	1.55929E-13	0.63531	0.36469	-0.18235	-0.31583
217	3.78736	1.55451E-13	0.13002	0.86998	-0.52357	-0.6948
221	3.85718	1.55539E-13	0.22304	0.77696	-0.50973	-0.58638
225	3.92699	1.55328E-13	0	1	-0.70711	-0.70711
229	3.9968	1.55539E-13	0.22304	0.77696	-0.58638	-0.50973
233	4.06662	1.55451E-13	0.13002	0.86998	-0.6948	-0.52357
240	4.18879	1.55929E-13	0.63531	0.36469	-0.31583	-0.18235
243	4.24115	1.55451E-13	0.13002	0.86998	-0.77516	-0.39496
247	4.31096	1.55737E-13	0.43235	0.56765	-0.52253	-0.2218
255	4.45059	1.55757E-13	0.45349	0.54651	-0.52789	-0.14145
259	4.5204	1.56043E-13	0.75581	0.24419	-0.2397	-0.04659
270	4.71239	1.56274E-13	1	0	0	0
281	4.90438	1.56043E-13	0.75581	0.24419	-0.2397	0.04659
285	4.97419	1.55757E-13	0.45349	0.54651	-0.52789	0.14145
293	5.11381	1.55737E-13	0.43235	0.56765	-0.52253	0.2218
297	5.18363	1.55451E-13	0.13002	0.86998	-0.77516	0.39496
300	5.23599	1.55929E-13	0.63531	0.36469	-0.31583	0.18235
307	5.35816	1.55451E-13	0.13002	0.86998	-0.6948	0.52357
311	5.42797	1.55539E-13	0.22304	0.77696	-0.58638	0.50973
315	5.49779	1.55328E-13	0	1	-0.70711	0.70711
319	5.5676	1.55539E-13	0.22304	0.77696	-0.50973	0.58638
323	5.63741	1.55451E-13	0.13002	0.86998	-0.52357	0.6948
330	5.75959	1.55929E-13	0.63531	0.36469	-0.18235	0.31583
333	5.81195	1.55451E-13	0.13002	0.86998	-0.39496	0.77516
337	5.88176	1.55737E-13	0.43235	0.56765	-0.2218	0.52253
345	6.02139	1.55757E-13	0.45349	0.54651	-0.14145	0.52789
349	6.0912	1.56043E-13	0.75581	0.24419	-0.04659	0.2397
360	6.28319	1.56274E-13	1	0	0	0

The pattern diameters are varied from 50 to 800 nm while the modulation amplitude was held constant at 100 nm. Since at first approximation the magnetostatic energy (E_M) is inversely proportional to the remanent magnetization (M_r) (i.e. $E_M \sim H_K \sim 1/M_r$), the polar plot of simulated results plotted with the opposite polarity, which is defined by ($1-E_M$).
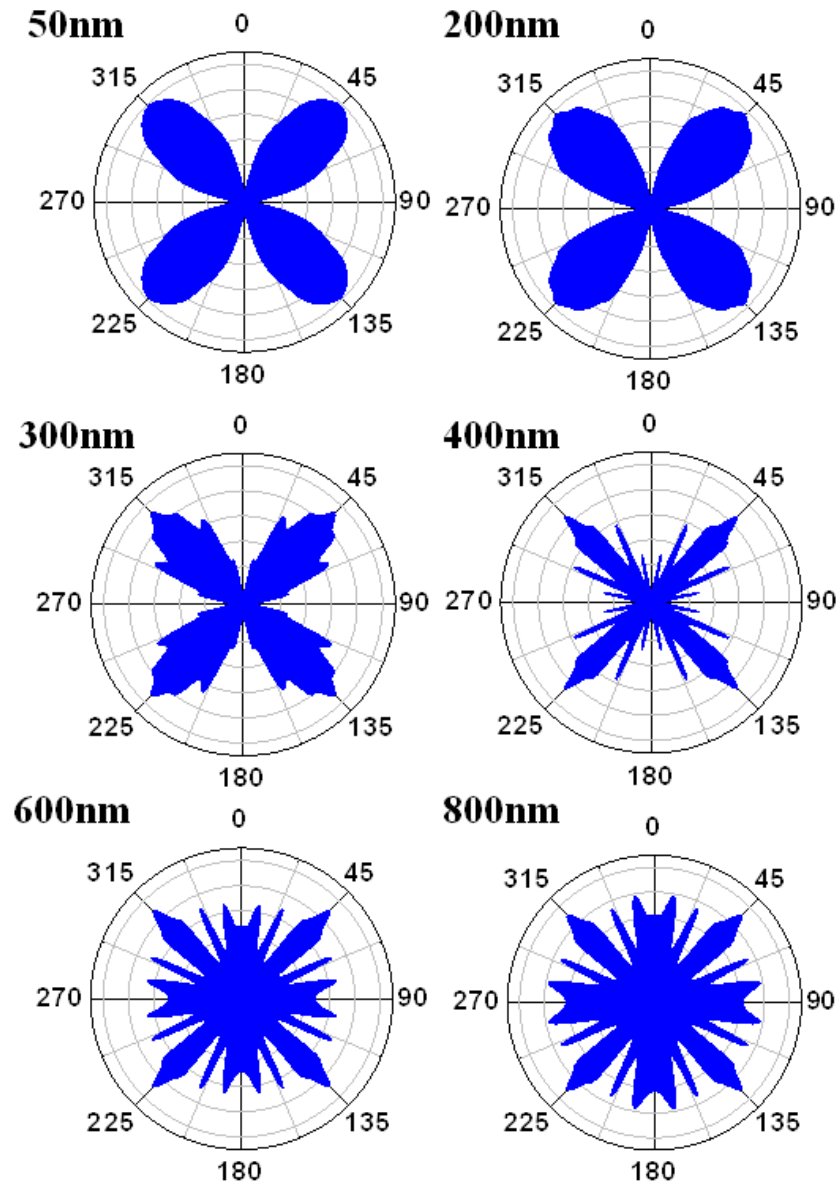
Fig. 5.11. Simulated angle dependence of magnetostatic energy derived from simulated demagnetization energy in nanomodulated films for different pattern diameter (D) from 50nm to 800nm plotted in inverse polarity. All of the plots certainly show 4-fold symmetry. Hints of new 8-fold peaks at 300 nm, 12-fold peaks at 400nm superimposed on the 4-fold ones are seen. Higher order peaks are observed in bigger diameter. The modulation amplitude (A) 200nm remained same for all diameters. Further decrease of modulation amplitude shows same type of result (symmetry increase).

This indicates the angle dependence of normalized magnetostatic energy (E_M) at a single domain state which in turn leads to an angular dependence of remnant magnetization (M_r).

The simulation results based on pattern diameter variation are shown in Fig. 5.11, where the remanent magnetization is plotted as a function of the angle of the applied field. To amplify the variation in magnetization the remanent magnetization is normalized. Variation of diameter and modulation amplitude shows a clear trend of symmetry variation. All of the plots in Fig.5.8 certainly show 4-fold symmetry. There is the indication of new 8-fold peaks at 300 nm, superimposed on the 4-fold ones, and these become clearer at 400 nm and 600 nm. The simulated result for 400 nm diameter matches well with the experiamental result for 400 nm pattern. In both the cases four fold symmetry including satellite peaks coming from eight fould symmetry were observed. The influence of symmetries has been plotted in Fig. 5.12, which shows that only 4n symmetries ($360°/\theta$ = symmetry, Fig. 5.12a) areavailable in a square pattern. Hence controllable (4n-fold) symmetry can be obtained in a square array pattern. This signifies that the nanomodulation minimizes the magnetostatic energy at least in the two equivalent <110> directions, where the uniaxial anisotropy (induced in the <010> direction during simulation) has been dominated by the anisotropy due to nanomodulation. For the smaller diameters (~50nm) this fourfold symmetry is dominant whereas satellite maxima beside each main maximum (<110> direction) become visible as the pattern diameter increases or modulation amplitude decreases. In a continuous patterned film, the coupling between the periods of the nanostructures is much stronger rather than inter-dot coupling between isolated 2D dot arrays which increases the anisotropy [98]. Thus, an eightfold or even higher order symmetry may contribute to the anisotropy considerably. In the case of the high aspect ratio substrate, the wave-like modulation of magnetic domains is envisaged to shift to the upper region (Fig.5.5-a). Here the modulation amplitude is more in the <110> direction than in the <100> direction and the hard axis is obtained in the <110> direction which is supported by simulation result (Fig.5.12-a). Same kind of results should occur in the case of low aspect ratio where wave like modulation shifts to the lower part of the modulated film (Fig.5.5-b). Variation of diameter and modulation amplitude shows a clear trend of symmetry (4n fold) variation. Similarly other type of symmetries can be obtained by changing the pattern or dipole arrangement.
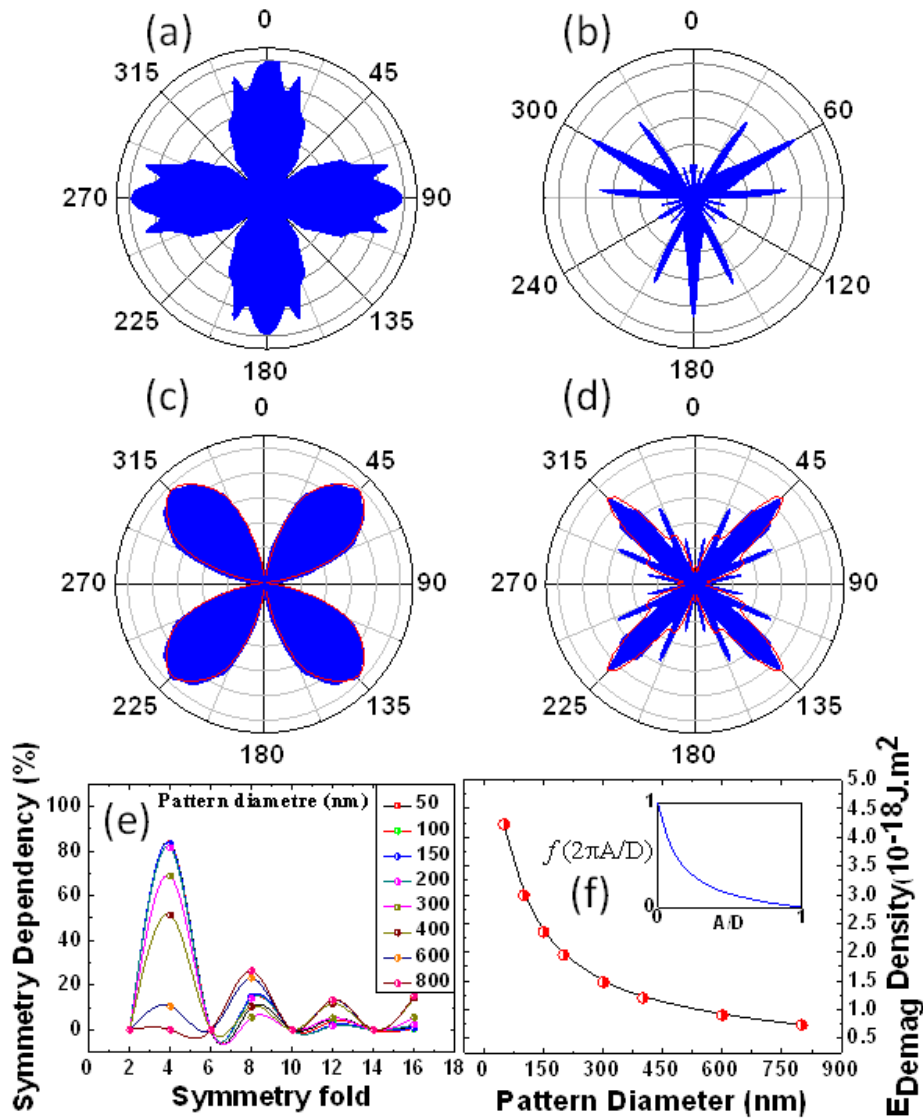
Fig. 5.12. For closed packed array phase shift has been observed (a). Equilateral triangular array shows 3n-fold symmetry (b). Fitted curve (redline) for 200nm (c) and 400nm (d) pattern with derived generalised anisotropy equation (Eqn.3). (e) Symmetry dependency for different pattern diameters, (f) Geometry depended Demagnetization energy. Inset graph shows the behaviour of f as afunction of A/D

The derived anisotropy equation (Eqn.4) fits well with our simulated results and describes possible anisotropies for different ferromagnetic materials. We considered up to 16-fold symmetry in curve fitting, which fits well to the data at lower diameter (~50nm) and near that (Fig. 5.12-c), but does not fit well at higher diameters(D) (Fig.5.9-d), which indicates

the dominance of lower order symmetry in lower diameters. The demagnetization energy density (calculated from simulated results) as a function of pattern geometry, follows function f [98], which delineates the fact that the uniaxial induced anisotropy is strongly dominated by the anisotropy created by nanomodulation. (Fig.5.12-f). Simulation of the triangular pattern shows a 3n–fold symmetry (Fig. 5.12-b) which supports the generalised model for possible different symmetries.

5.5. Generalized anisotropy model for modulated thin film

The pattern gives both in-plane and out-of-plane modulation (Fig. 5.5-a-b-c) which allows dipoles to rotate. The effective magnetostatic interaction strength is based on three different parameters: out-of-plane modulation amplitude, in-plane modulation amplitude and direction, based on modulation geometry and their arrangements.

A possible starting point for the description of the angularly-dependent magnetic behaviour for this patterned media in terms of anisotropy would be to consider all kinds of anisotropies in a system. We can write an equation for magnetic anisotropy in the following way:

$$H_K(r,\phi,\theta) = \frac{2}{\mu_0 M_S}\left[\frac{K_S \bullet V}{2}\sum_{i \neq j}\cos(i) \bullet \cos(j) + K_I \sin^2\theta + \sum_n K_n \cos^2(n.2\theta) + K_0\right]$$

Equation 5.4

Where the elements in the square bracket are in the following order i) Global shape anisotropy of the sample, ii) Induced Uniaxial Anisotropy, iii) Anisotropy due to patterning and iv) any other anisotropy. For simulation we rotated only the pattern to exclude any kind of shape anisotropy. So except for the second and third part, the others remain the same for comparison as a function of angle. We simplify Eq. 5.4 as follows.

$$H_K(\theta) = \frac{2}{\mu_0 M_S}\left[K_I \sin^2\theta + \sum_n K_n \cos^2(n.2\theta)\right]$$

Equation 5.5

We generalise a possible directional symmetry where n = β/α; α is a number representing a minimum geometrical symmetry (i.e. 4 for square, 3 for equilateral triangular/hexagon) and β is a positive integer. K_n denotes the anisotropy constant for the corresponding symmetries. In nanomodulated films the magnetization follows a wave-like path due to modulation geometry [98] and creates two types of magnetic charge dipoles. Since magnetic induction $\mathbf{B}=\mu_0$ ($\mathbf{H}+\mathbf{M}$) don't have divergence, the points where lines of magnetization originate or terminate can be considered as magnetic charge poles with opposite polarity. Looking through the cross section the magnetization directions are opposite to each other at two sides of an element which creates an out-of-plane dipoles (Fig. 5.5-a-b). In the case of in-plane view magnetization directions at reverse sides of an element are of opposite polarity in an external magnetic field direction, which gives in-plane dipoles (Fig. 5-c). These dipoles can interact with each other strongly only when there is a chain of elements in the applied field directions, creating an anisotropic magnetization throughout whole film. We consider all types of magnetic interaction in different region and by using sum rules given by Yafet, et. Al [99] the total magnetostatic energy is given by,

$$E_{mag} = E_{mag}^{x} + E_{mag}^{y} + E_{mag}^{z} = \left(\frac{1}{2}\right)4\pi M_S{}^2 VA \qquad \text{Equation 5.6}$$

where

M_S is the saturation magnetization,

V is the volume

and A is modulation amplitude.

Since by symmetry in a square struture;

$$\mathbf{E_{mag}^{x}} = \mathbf{E_{mag}^{y}} = \mathbf{E_{mag}^{\parallel}} \qquad \text{Equation 5.7}$$

magnetostatic energy becomes,

$$E_{mag} = E_{mag}^{\perp} + \mathbf{2E_{mag}^{\parallel}} = \left(\frac{\mathbf{1}}{\mathbf{2}}\right)\mathbf{4\pi M_S^2 VA} \, . \qquad \text{Equation 5.8}$$

For an externally applied field H the magnetostatic energy can be written as

$$\mathbf{E_{mag}} = \int -\frac{1}{2}\vec{\mathbf{M}}.\vec{\mathbf{H}}\mathbf{dv}$$. We can consider two different layers of the pattern with magnetic

and nonmagnetic regions in each layer. The magnetization can be written as

$\mathbf{M} = \mathbf{M_1^U} + \mathbf{M_2^U} + \mathbf{M_1^L} + \mathbf{M_2^L}$ for an applied field $\mathbf{H} = \mathbf{H_1^U} + \mathbf{H_2^U} + \mathbf{H_1^L} + \mathbf{H_2^L}$ (U ~ Upper

layer, L ~ Lower Layer, 1 is magnetic region and 2 is nonmagnetic region) for 4 different

cases. Then we can write magnetostatic energy in following way for patterned structure,

$$E_{mag} = \sum_{n,m} \int -\frac{1}{2}\vec{M}_i^j \ .\vec{H}_{n,m}dv \qquad\qquad \text{Equation 5.9}$$

Where the distribution of magnetization can be expanded in Fourier series as follows,

And the field correspond to each magnetization will be, $\mathrm{div}H_i^j = -4\pi\mathrm{div}M_i^j$

The inter-layer interaction gives perpendicular anisotropy and the remaining effects give

in-plane anisotropy. M. Rewienski [101] found magnetic anisotropy of ferromagnetic thin-

films due to surface roughness. Using the same principle we have calculated the anisotropy

energy due to each single element as $\mathbf{E_{mag}^{\parallel}} = \mathbf{C_i}\left(\dfrac{\mathbf{1}}{\mathbf{2}}\right)\mathbf{M_s^2}\left(\dfrac{\mathbf{1}}{\mathbf{4}}\right)\left[\mathbf{A}\left\{\mathbf{1} - \mathbf{f(2\pi\dfrac{A}{D}}\right\}\right]$

and $\mathbf{E_{mag}^{\perp}} = \mathbf{C_i}\left(\dfrac{\mathbf{1}}{\mathbf{2}}\right)\mathbf{M_s^2}\left(\dfrac{\mathbf{1}}{\mathbf{2}}\right)\left[-\mathbf{A}\left\{\mathbf{1} - \mathbf{f(2\pi\dfrac{A}{D}}\right\}\right]$ where C_i is a constant which

depends on pattern geometry and aspect ratio. The function [101] f is 0 at A/D=1 and 1 at

A/D=0 (Fig. 5-f inset). The dipolar anisotropy is given by $\mathbf{E_{da}} = \mathbf{E_{mag}^{\parallel}} - \mathbf{E_{mag}^{\perp}} \neq \mathbf{0}$ which

gives a finite dipolar anisotropy energy depending upon the modulation geometry.

Considering up to second-order harmonics, we can rewrite the dipolar anisotropy for

anisotropy energy as $K^S = C_i.\left(\dfrac{1}{2}\right)4\pi M_s^2\left(\dfrac{3}{4}\right)A\left[1 - f\left\{2\pi\dfrac{A}{D}\right\}\right]$, where A is the amplitude of

modulation and D is the diameter of the element. The magnetostatic interaction strength

depends on the density of elements in a particular direction. So we add another term sin

(90°/β) for patterned induced magnetic anisotropy where β is a positive integer.

Using the expression for K^S we can then rewrite Eq. 5.2

$$H_K(\theta) = \frac{2}{\mu_0 M_S}\sum_n .C \bullet A\left[1 - f\left\{2\pi\frac{A}{D}\right\}\right]\left\{\sin\left(\frac{90°}{\beta}\right)\right\}\cos^2\left(\beta \bullet \frac{2\theta}{\alpha}\right). \qquad \text{Equation 5.10}$$

Where, n = β/α, α is a number representing a minimum geometrical symmetry (i.e., four for square, three for equilateral triangular/hexagonal), the constant C depends upon single element geometry and diameter/separation (D/S). This equation describes the possibility of anisotropy variation by nanomodulation geometry for different ferromagnetic materials. The magnetostatic energy due to the dipolar configuration can be expressed as follows. For this model we assumed that each pattern has a single domain magnetic dipole, circularly shaped, they can be rotated across the center of dipole moment and the

$$M(x,y) = \sum_{n=0}^{+\infty} \sum_{m=0}^{+\infty} M_i^j \, \sin(k_n x)\sin(k_m y)$$

Equation 5.11

neighboring spins are not exchanged coupled. The system energy includes magnetostatic energy and the Zeeman energy while exchange coupling is neglected.

$$\mathbf{E_{Total} = E_{dipole} + E_{xternal}}$$

Equation 5.12

And

Where g is the gyromagnetic factor and μB is the Bohr magneton.

The total dipolar energy in the infinite array can be expressed as

$$\mathbf{E_{dipole}} = \frac{1}{2}g^2\mu_B{}^2\sum_{R_i}\sum_{R_i}\left[\frac{M_i.M_j}{R_{ij}{}^3} - 3\frac{(\vec{M}_i.\vec{R}_{ij})(\vec{M}_j.\vec{R}_{ij})}{R_{ij}{}^5}\right]$$

Equation 5.13

$$\mathbf{E_{external}} = H_{external}\cdot\sum_i M_i$$

Equation 5.14

Where g is the gyromagnetic factor and μB is the Bohr magneton.

The total magnetostatic energy is the sum of surface and volume energy generated due the in plane and out of plane dipole formation and inter dipole interaction at the volume and surface of nanomodulated thin film.

$$E_{Total} = E_{volume} + E_{surface}$$

Equation 5.15

The total dipolar energy in the infinite array can be expressed as

$$E_{Total}\Big|_{-\infty}^{+\infty} = -\int_{\substack{Sample\\Volume}} \nabla.M_S\hat{m}_i(R_i)\frac{\vec{R}_{ij}}{\left|R_{ij}\right|^3}dV + \int_{\substack{Sample\\Surfacee}} n_s.M_S\hat{m}_i(R_i)\frac{\vec{R}_{ij}}{\left|R_{ij}\right|^3}dS$$

Equation 5.16

Where $M_S m_i$ is magnetization for each dipole.

The static dipolar energy depends upon the dipole interaction. Thus the geometry of the patterned structure plays an important role.
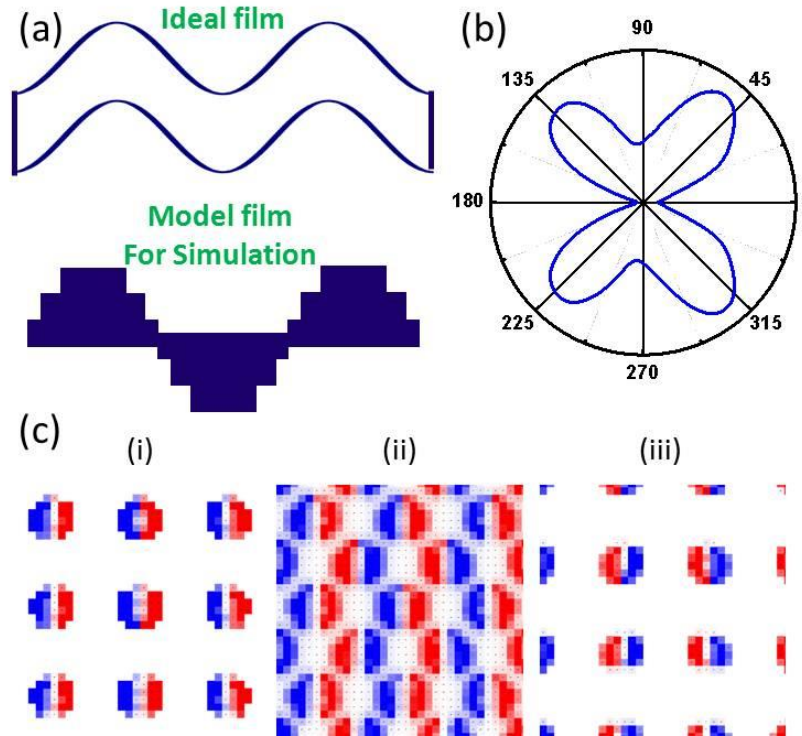
Fig. 5.13. (a) Ideal film and model film for OOMMF simulation. (b) Angle dependent remanant magnetization (M_r vs. θ) measured from 3D nanomodulated film with 400nm. (c) OOMMF simulation shows dipoles exist all over the film.

Static magnetic properties of 7x7 ordered array of magnetic pattern have been examined by solving Landau-Lifshitz-Gilbartz equation in OOMMF package. [79] An external field is applied in the plane of array in <10> direction. All spins are aligned along the field direction by applying a sufficiently large field at the initial stage of each simulation (Fig. 5.13). The simulation shows the anisotropy symmetry due to three dimensional continuous patterned structures. The dipole configuration exists all over the sample configured by

pattern geometry (Fig. 5.13.c). The rotation of the field rotates the magnetic dipole. The strength of dipolar energy varies depending upon array symmetry and magnetostatic energy varies accordingly.

5.6. Summary

In this chapter, the variation of magnetic anisotropy is investigated through the formation of magnetic dipoles in continuous ferromagnetic thin-films due to a unique nanomodulation. Experimental evidence of well-ordered dipoles with metastable state have been detected by means of variation of magnetic anisotropy, step hysteresis and MFM imaging. The novel 3D modulation generates both in plane and out of plane dipoles, where the competition between in-plane and out of plane dipoles creates metastable state giving opportunity to manipulate anisotropy. The anisotropy model, based on collective dipolar interaction was used to demonstrate the ability to control anisotropy in continuous ferromagnetic thin-films by minimizing magnetostatic energy through nanomodulation. The change of diameter/separation ratio (D/S) in nanomodulation can switch the anisotropy direction due to the transformation of the modulation wave from one layer to another layer. The generalised model helps us to find out possible anisotropy based on material property and geometrical arrangement of nanopattern. By varying amplitude/diameter (A/D) ratio and geometrical arrangement (α) one can achieve desired anisotropy. Thicknesses close to the modulation amplitude provide more control over the anisotropy. Additionally, the formation of a metastable single domain resists vortex formation in nanopatterned ferromagnetic thin-films which is essential for realizing devices such as volatile memory, magnetically frustrated patterned media [90], highly integrated nanoscale magnetic devices [101, 102] etc. Fourier analysis of magnetostatic energy for this nanomodulated film supports the existence of magnetic diploes ($E_{da} \neq 0$). The derived generalised mathematical expression based on magnetic dipolar interaction is found to be in good agreement with our results, which can help to estimate and understand the anisotropy in other pattern media also. The method described in this work is much simpler and can be demonstrated at a larger scale. In this unique three dimensional continuous ferromagnetic film the magnetostatic energy is tuned by magnetic interaction among the magnetic dipoles in

patterned array with in-plane external magnetic field. A strong out of plane dipoles are generated by in-plane magnetic field and the competition between in-plane and out-of-plane magnetic dipole resists vortex formation in nanostructure thin ferromagnetic film which can be a key factor in high density storage media. The micromagnetic simulation shows a qualitative agreement with the experimental results.

6 Chapter – Giant exchange anisotropy in Bismuth ferrite (BFO) nanocomposite

6.1. Introduction

In a period spanning more than five decades now, exchange anisotropyor exchange bias effect has been observed in a multitude of magnetic heterostructures: (i) ferromagnet-antiferromagnet [18], (ii) ferromagnet-spin glass [104], (iii) ferrimagnet-antiferromagnet [105], (iv) ferrimagnet-ferromagnet [106], (v) ferromagnet spin glass-antiferromagnet [107], etc. Conventionally, the exchange bias—measured by the shift of the magnetic hysteresis loop along the field axis—requires pre-biasing of the interface moment via a field cooling protocol from above the magnetic transition point [108]. This pre-biasing sets the unidirectional anisotropy by breaking the symmetry of the interface moment. Exchange bias has also been observed, spontaneously, when even in the absence of pre-biasing, unidirectional anisotropy sets in under the first field of loop evaluation [109, 110], where the sample is cooled down from above the transition point under zero field. The spontaneous exchange bias (SEB), where the unidirectional anisotropy (UA) sets in spontaneously under the application of the first field of a hysteresis loop even in an unmagnetized state, is a consequence, primarily, of biaxial symmetry in the antiferromagnetic (AFM) structure of ferromagnetic (FM)-AFM interface [111-113]. In a spin glass (SG)-FM structure, on the other hand, the anisotropy sets in under field cooling via oscillatory Ruderman-Kittel-Kasuya-Yosida (RKKY) interaction [114]. However, we demonstrate in this chapter that glassy moments at the interface, in fact, introduce an additional magnetic degree of freedom in between the exchange coupled FM and AFM grains and breaks the symmetry truly spontaneously even before the application of the first field of a loop to set the UA in an unmagnetized state. As discussed later, the consequence of this is an asymmetry in the SEB depending on the path followed in tracing the hysteresis loop—positive or negative. In a nanocomposite of $BiFeO_3$ (~94%)-$Bi_2Fe_4O_9$ (~6%),we observed (i) a large SEB (~300–600 Oe) across 5–300 K, (ii) asymmetry in SEB depending on the path followed in tracing the hysteresis loop—positive or negative, and (iii) a

nonmonotonic variation of SEB with temperature. The magnitude of the SEB itself is far higher than what has so far been observed in all the bulk or thin film based composites of $BiFeO_3$ [115–118] even under magnetic annealing. We have also observed the conventional magnetic-annealing-dependent exchange bias (CEB) with all its regular features such as dependence on annealing field, rate, and training. The random field generated by the glassy moments at the shell appears to be influencing the indirect exchange bias coupling called ''superinteraction bias coupling'' between the FM core [120] of finer $Bi_2Fe_4O_9$ and local moments of AFM order in coarser $BiFeO_3$ and inducing the SEB, its path dependence, and its nonmonotonicity in variation with temperature. This has been investigated in nanocomposite of ~112 nm $BiFeO_3$ and ~19 nm $Bi_2Fe_4O_9$.

6.2. $BiFeO_3$-$Bi_2Fe_4O_9$ nano-composite

6.2.1. Sample preparation

The nanocomposite of $BiFeO_3$-$Bi_2Fe_4O_9$ has been synthesized at Central Glass and Ceramic Research Institute (CGCRI) - India by sonochemical route where coprecipitation from aqueous solution of mixed metal nitrates takes place in presence of ultrasonic vibration. The precipitate thus formed is collected in a centrifuge running at 12000 rpm. The powder is finally washed, dried and calcined at 350-550°C for 4-5h in air. The pH of the medium of coprecipitation, ultrasonic vibration energy, heat-treatment temperature, and time etc. can be controlled to yield nano-sized particles of either pure $BiFeO_3$ or a nanocomposite of $BiFeO_3$-$Bi_2Fe_4O_9$ of varying concentration ratio of the component phases. Three type of nanocomposite was prepared: BFO-A with 112 nm $BiFeO_3$ (~94%)- 19 nm $Bi_2Fe_4O_9$ (~6%),BFO-B 57 nm $BiFeO_3$ (~90%)- 13 nm $Bi_2Fe_4O_9$ (~10%) and BFO-C (pure $BiFeO_3$).

6.2.2. Structural analysis

The particle morphology and the crystallographic details have been studied by transmission electron microscopy (TEM), selected area electron diffraction (SAED), and high resolution

transmission electron microscopy (HRTEM). The Rietveld refinement of the high resolution powder x-ray diffraction pattern too offers information about the crystallographic details of the component phases in addition to the crystallite sizes and volume fraction of each phase.The crystallite sizes for the $BiFeO_3$ and $Bi_2Fe_4O_9$ phases turn out to be ~112 and ~19 nm for sample A, 57 and 13 nm for sample B, respectively, for this nanocomposites. The estimation from the x-ray diffraction data (Table 4) matches closely with what has been observed in TEM. Therefore, it appears that finer particles of $Bi_2Fe_4O_9$ are dispersed within the matrix of coarser $BiFeO_3$ particles.
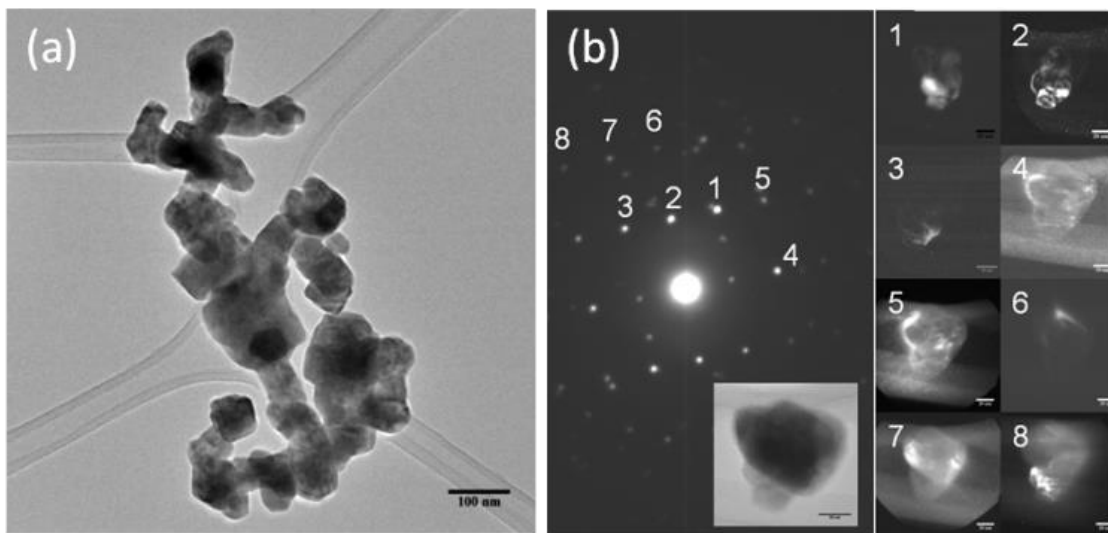
Fig. 6.1. (a) A representative bright-field TEM image of the nanocomposite (b) the SAED patterns showing diffraction spots from both the phases; the dark-field

In Fig.6.1a, we show a representative bright field TEM image of the nanocomposite while in Figs. b and c, the representative dark field (DF) - bright field (BF) images of the individual particles and corresponding SAED and HRTEM (Fig. 6.1 a) images are shown. A large number of HRTEM (Fig. 6.1 a), BF-DF TEM (Fig. 6.1 b & 6.2 a) and SAED (Fig. 6.2 b) images have been taken across different regions of the nanocomposite and analyzed in order to determine the concentration of the interfaces. The SAED patterns showing diffraction spots from both the phases; the dark-field images (marked by numbers) in the side panel (Fig.6.1b) shows the regions of the particles corresponding to the diffraction spots; inset shows the bright-field image of the region; the bright-field/dark-field images

together with electron diffraction patterns from the regions show the dispersion of the phases and the interfaces in the nanocomposite. It is interesting to observe that the finer $Bi_2Fe_4O_9$ particles are nearly evenly dispersed within the matrix of coarser $BiFeO_3$ particles thus maximizing the interface density. The SAED spots from the single crystalline $BiFeO_3$ and $Bi_2Fe_4O_9$ particles have been identified and indexed accurately using the interplanar spacing (d) and angle (ø) data of the BiFeO3 (space group R3c, hexagonal unit cell) and $Bi_2Fe_4O_9$ (space group Pbam, orthorhombic unit cell) phases (Fig. 6.1). In the case of those spots which could be identified to be corresponding to a particular single crystal with a well-defined zone axis, the accuracy of indexing has been verified from the Weiss zone law as well. Determination of the zone axes for the crystals of $BiFeO_3$ and $Bi_2Fe_4O_9$ yields the tilt across an interface as ~19° for a test case. However, since the particles are nano-sized and are oriented in different directions with respect to the beam direction, it is difficult to determine the zone axes for all such particles and find out the entire distribution pattern of orientation across the interfaces.
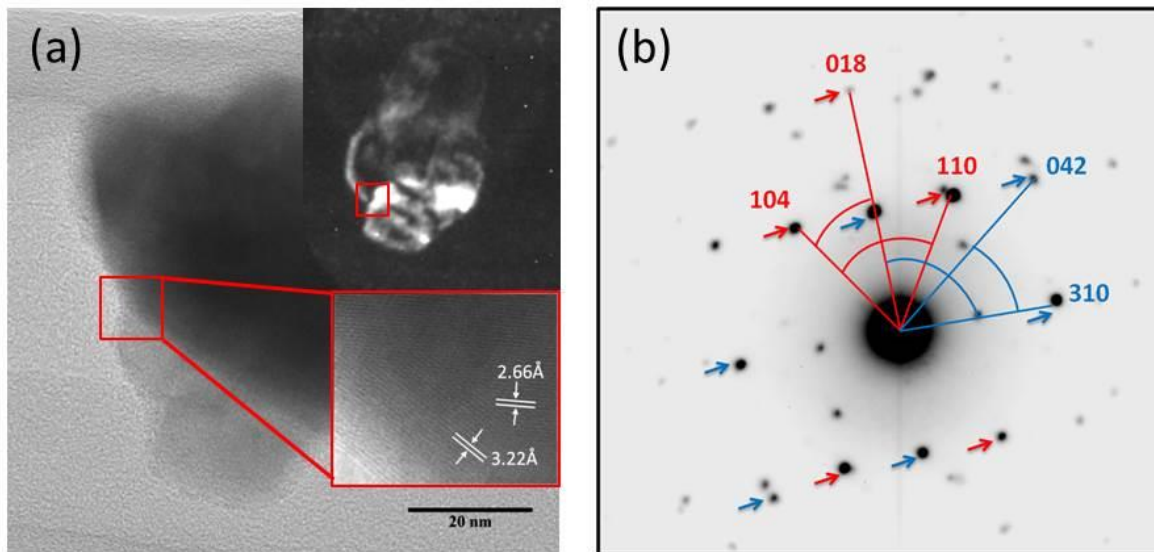
Fig.6.2. (a) a representative bright-field TEM image of an interface; top inset shows the dark-field image of the region while the bottom inset shows the HRTEM image of different orientation of the lattice fringes at the interface; (b) electron diffraction spots with their indexing corresponding to the pattern shown ; red and blue colors indicate the BiFeO3 and Bi2Fe4O9 phases, respectively.

Table 5

Structural details of the phases in the nanocomposite from FullProf refinement of x-ray diffraction data (done by S Goswami at CGCRI, Kolkata, India).

Phase	Lattice Parameters (Å)	Ions	Wycoff Positions	x	y	z	Bonds	Length (Å)	Bonds	Angle (°)	Crystallite Size	Vol. Frac.
$BiFeO_3$ (R3c)	a=5.579(5)	Bi	6a	0.0	0.0	0.0	Bi-O	2.282(3)	Fe-O-Fe	152.19(7)	111.9	93.89
	c=13.863(7)	Fe	6a	0.0	0.0	0.2251(5)	Bi-O	2.499(5)	O-Bi-O	72.36(4)		
		O	18b	0.4392(3)	0.01530(6)	-0.0482(4)	Fe-O	1.918(5)				
							Fe-O	2.165(3)				
$Bi_2Fe_4O_9$ (Pbam)	a=7.976(6)	Bi	4g	0.1624(3)	0.1597	0.0	Bi-O	2.461(3)	Fe-O-Fe	129.79(5)	19.3	6.11
	b=8.479(9)	Fe1	4f	0.5	0.0	0.2669(3)	Bi-O	2.295(2)	O-Bi-O	65.72(3)		
	c=6.008(3)	Fe2	8i	0.3682(5)	0.3356(7)	0.5	Bi-O	2.438(3)				
		O1	2b	0.0	0.0	0.5	Fe-O	2.092(4)				
		O2	8i	0.3722(7)	0.2147	0.2425(6)	Fe-O	1.545(7)				
		O3	4f	0.1337(4)	0.4039(2)	0.5	Fe-O	2.016(4)				
		O4	4g	0.1534(6)	0.4303(6)	0.0						

6.3. Magnetic measurements of exchange anisotropy/exchange bias

The magnetic measurements have been carried out in a SQUID magnetometer (MPMS, Quantum Design) across5-300 K under a maximum field H_m of 50 kOe. In order to ensure that there is no trapped flux both in the superconducting coil of MPMS and in the sample we followeda well-designed protocol to demagnetize them. An oscillating field with varying amplitude, where the amplitude reduces from maximum to zero has typically been applied. For example, for a demagnetizing field 1000Oe, the amplitude is brought down to zero in the following sequence: (+1000) - (-900) - (+800) - (-700) ... (+50) - (-40) ... (+5) - (-4) - (+3) - (-2) - (+1) - (0). The superconducting coils of MPMS are normally discharged from high field (50 kOe) in oscillation mode; the amount of trapped flux is typically ~10 Oe. Before starting a new batch of experiments, the superconducting coil was warmed to room temperature which is above the critical point. In addition, prior to the measurement of SEB, the sample itself was demagnetized with oscillating field using an appropriate protocol in order to ensure that there is no trapped flux in the sample.We have also measured the SEB at 300 K for a maximum field of 18 kOe following zero-field cooling (ZFC) from a high temperature (~700 K) - which is even above the magnetic transition point T_N (~590 K) of the AFM component - in a vibrating sample magnetometer for a test case. We obtain an SEB of ~81 Oe at 300 K which is consistent with the SEB for different Hm across 10-50 kOe measured in SQUID. This shows that the demagnetization protocol used in SQUID was appropriate in ensuring unmagnetized state of the sample prior to the measurement. We report here mainly the results obtained in a nanocomposite of ~6% $Bi_2Fe_4O_9$ and ~94% $BiFeO_3$ (sample-A) which exhibits maximum SEB and CEB. In Fig. 6.3, the results from the magnetic measurements are shown. In Fig. 6.3 a, we show the hysteresis loops which yield the SEB at several temperatures across 5-300 K. The region near the origin is blown up to show the extent of EB clearly. We used a field step size of 100 Oe near the origin of hysteresis loop in order to measure the exchange bias accurately. The field span of 10 kOe under such a protocol is covered typically within ~3h (~10^4s) which gives the time scale of each of the measurements. In each case, the presence of a large shift in the loop along the field axis is conspicuous. This shift cannot result from relaxation of coercivity of the FM component as the tensorial nature of the

magnetocrystalline anisotropy cannot contribute to the unidirectional anisotropy. The EB (H_E) is given by (H_{C1} + H_{C2})/2 while the coercivity H_C is given by (H_{C1} - H_{C2})/2; H_{C1} and H_{C2} are the fields corresponding to the points in forward and reverse branches of the hysteresis loop at which the magnetization reaches zero.
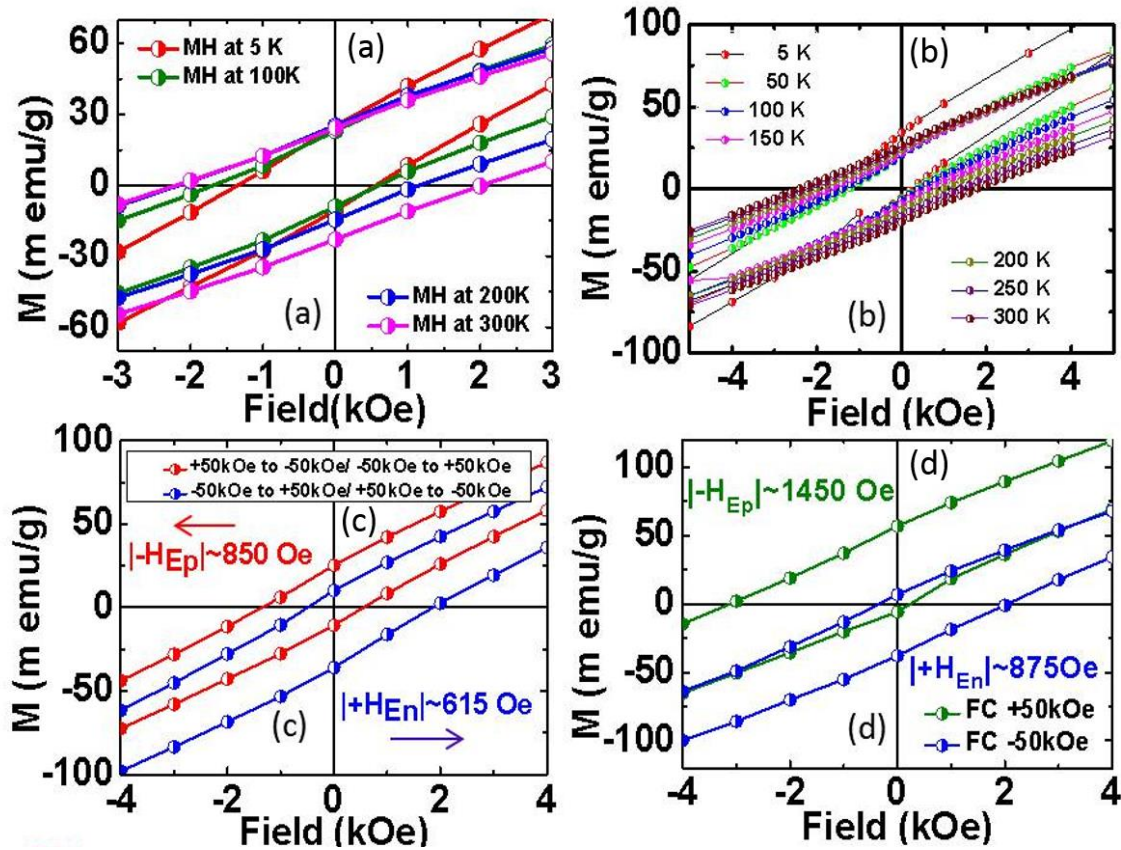
Fig. 6.3. **(a) The hysteresis loop shift, signifying SEB at different temperatures across 5-300 K, measured under 50 kOe following zero-field cooling; the region near origin of the loop is blown up to show the extent of exchange bias clearly; (b) shows the CEB at different temperatures across 5-300 K measured under a field cooling with +10 kOe; (c) shows the switch in sign and change in magnitude of the loop shift at 5 K signalling asymmetry and tunability of the SEB depending on the sign of the starting field (+50 kOe/-50 kOe) of hysteresis loop measurement; (d) switch in sign and change in magnitude of the CEB at 5 K measured following field cooling under +50 kOe/-50 kOe.**
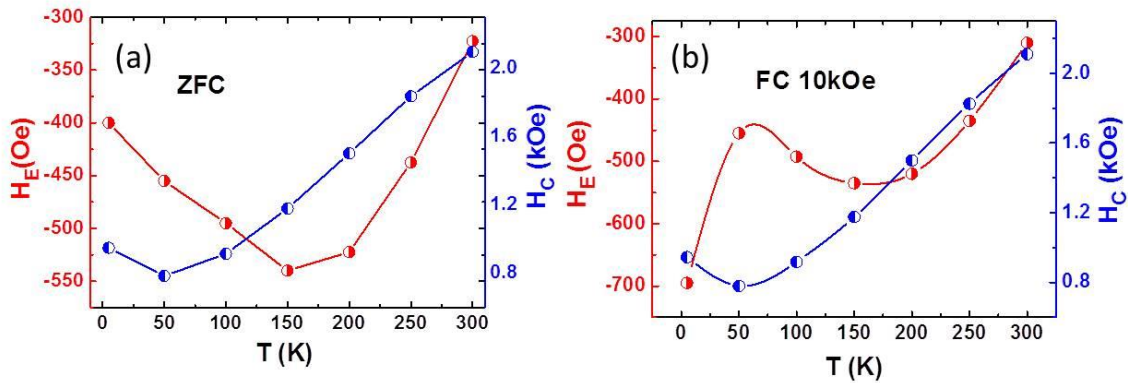
Fig. 6.4. (a) The variation of SEB and corresponding H$_C$ with temperature; and (b) the variation of CEB - measured following field cooling under +10 kOe - andcorresponding H$_C$ with temperature (lines are guide to the eyes).

6.4. Result and discussion

The extent of SEB observed here right across 5-300 K is quite large and comparable to what has been reported by Wang et al. [112] in Ni-Mn-In bulk alloys at 10K. While ramping the temperature from one point to another a constant ramp rate of 2.5 K/min has been used. The observation of SEB iteslf in BiFeO$_3$ based bilayer or composite system has not been reported so far, and, for the first time, we are reporting it in the nanocomposite of BiFeO$_3$-Bi$_2$Fe$_4$O$_9$. In Fig. 6.3c, the asymmetry and hence the tunability of the SEB at 5 K has been demonstrated. Depending on the sign of the starting field +50 kOe (-50 kOe), the sign of the SEB is negative (positive) as well as |-H$_{Ep}$| > |+H$_{En}$|. This is also remarkable and has not yet been observed in any other system exhibiting SEB [104]. Fig. 6.3 b shows the CEB measured after a magnetic annealing treatment with 10 kOe. In this case a field of 10 kOe has been applied at room temperature and then the temperature was ramped down to the given point at a cooling rate of 2.5 K/min. Like SEB, the CEB too turns out to be negative i.e., annealing under positive (negative) field yields hysteresis loop shift in negative (positive) direction along the field axis. Even more interesting is that, in this case too, the exchange bias H$_E$ for positive (negative) annealing field is asymmetric with |-H$_{Ep}$| > |+H$_{En}$|. This has been demonstrated clearly in Fig. 6.3d which shows the asymmetry in the shift of the loop along the field axis at 5 K depending on whether the sample has been

field-cooled under +50 kOe or -50 kOe. This asymmetry was observed for SEB as well (Fig.6.3c). In Figs. 6.4a and 6.4b, respectively, we show the H_E and H_C
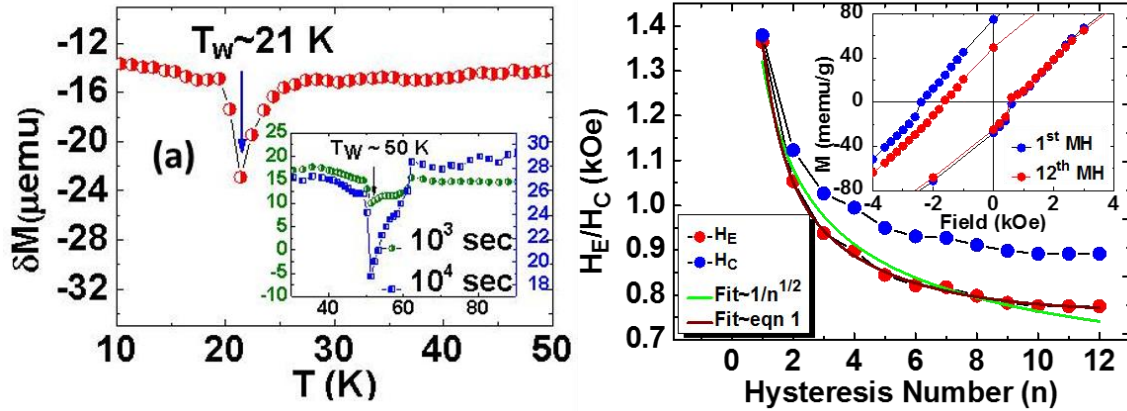
Fig. 6.5. **(a) The characteristic dip at ~21 K in the differential between two ZFC magnetization versus temperature patterns recorded under two different protocols - asimple ZFC and a ZFC with "stop-and-wait" approach; inset shows a similar dip even at 50 K; it appears to become sharper and more prominent with the increase in wait time; (b) The impact of training effect on CEB for sample-A; the CEB and HC decreases with the increase in number of hys- teresis cycles (n); inset shows a portion of the loop at first and twelfth cycle.**

as a function of temperature (T) for SEB (measured under 50 kOe) and CEB (measured following FC with 10kOe). The H_E and H_C in both of these cases are nearly identical in magnitude and nonmonotonic. While H_E-T plots exhibit valleys at ~150 K for both SEB and CEB, the H_C-T plots exhibit valleys at ~50 K. In addition, the H_E-T plot exhibits a peak at ~50 K for CEB (Fig. 6.4b). The nearly identical magnitude of H_E and H_C signifies nearly identical uniaxial anisotropy (UA) at the interface and domain pinning under ZFC and FC with 10 kOe. H_E, however, is large at 5 K, possibly, because of large magnetization at low temperature which could increase further under field cooling. In order to trace the origin of all these features, we investigated the spin structure both in the bulk of the $BiFeO_3$ and $Bi_2Fe_4O_9$ particles as well as at their interfaces from well-designed protocol dependent magnetic memory and training effect measurements.
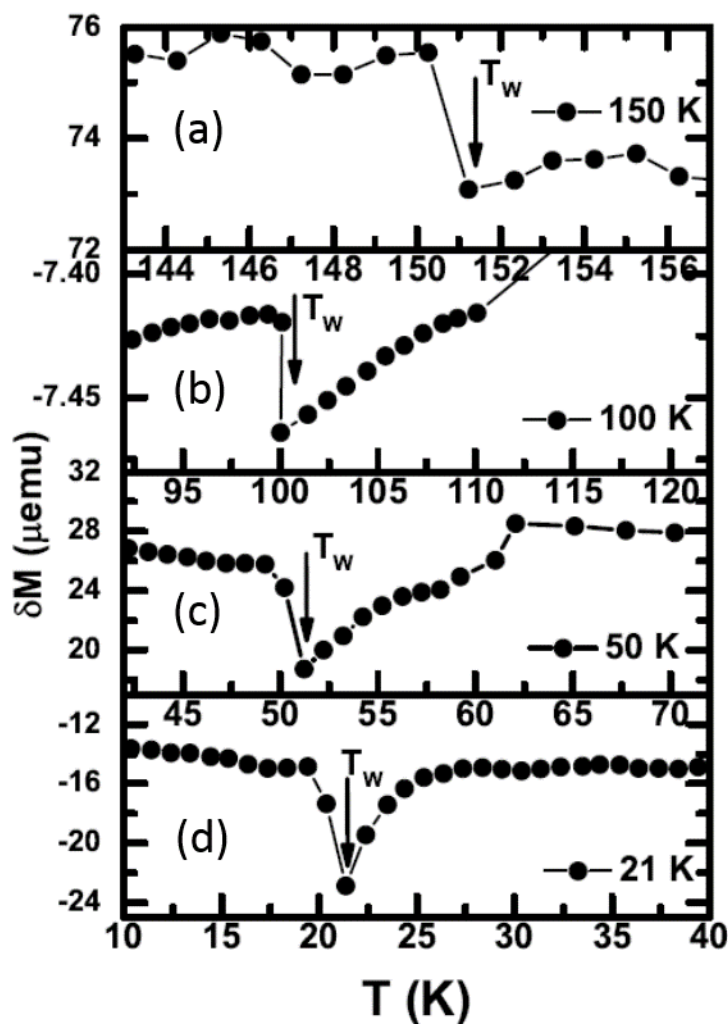
Fig. 6.6. The memory effect observed at 21 K, 50 K, 100 K, and 150 K under 'stop-and-wait' protocol of magnetic moment versus temperature measurement. This effect proves the presence of superspin glass moments in the nanocomposite. The effect becomes more prominent as the temperature decreases.

We obtained a profound signature of the presence of superspin glass (SSG) moments in the memory effect measurement for sample-A. We used a 'stop-and-wait' protocol to measure the memory effect which is an unequivocal signature of the presence of SSG [121, 122]. In 'stop and wait' protocol the ZFC measurement is interrupted at a given temperature below blocking temperature (T_B) or glass transition temperature (T_g). The system is maintained at this temperature for a certain time or long wait (for example 10^4 sec) and

then the cooling process again continue down to the possible lowest temperature (2K in this case). When the magnetization is measured as a function of temperature during warming up, lower values of the magnetization with respect to the values of the reference curve, measured in the ZFC process without interruption are observed in the temperature region where the previous ZFC cooling process was stopped or at the wait point (T_w). The sample was first cooled down to 2 K from room temperature under zero field and an M(T) pattern (which acts as reference line) was measured under 200 Oe.
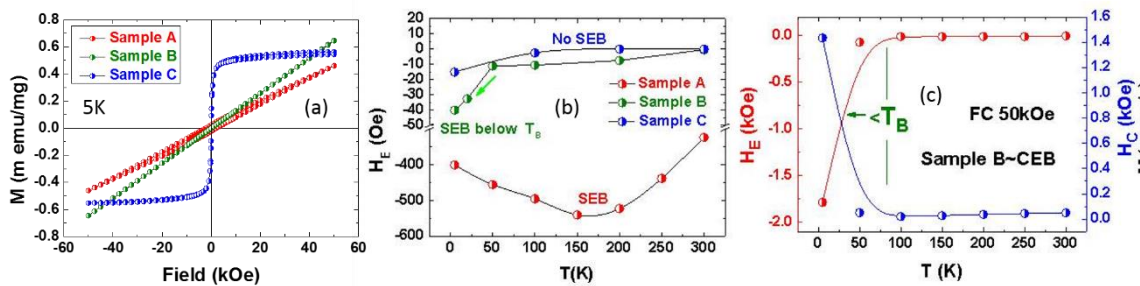
Fig. 6.7. (a) Hysteresis loops measured for three samples at 5K temperature. No exchange bias was found in Sample C which is pure $BiFeO_3$. (b) The SEB for all the three samples with different volume fractions of the $Bi_2Fe_4O_9$ phase. (c) The CEB and H_C versus temperature plot for sample B. Large CEB (measured following field cooling under 50 kOe) could be observed at only below T_B.

After the sample temperature reaches 300 K, it was again brought back to 2 K under zero field. The M(T) measurement was then repeated but with a 'stop-and-wait' protocol. As the temperature reaches at Tw ~21 K, the measurement was stopped and waited at that temperature for ~10^4s. The difference between the two patterns ~M(T) is shown in Fig.6.5a main frame. The memory effect is shown as a dip at ~21 K which confirms the presence of SSG phase in the nanocomposite. The entire measurement has been repeated for T_w~50 K (Fig. 6.5a inset). The memory effect could be observed even at other temperatures as well. We further measured the wait-time dependence of the memory effect (Fig. 6.5a inset). It appears that the effect becomes sharper and more prominent with the increase in wait time across 10^3-10^4s. The SSG moments develop due to interaction among the frozen superparamagnetic domains - possibly present at the shell of the finer $Bi_2Fe_4O_9$ particles of core-shell structure with FM core - at finite interparticle distance below the blocking temperature (T_B> 350 K for sample-A) [123]. With the rise in exchange coupling strength,

the superparamagnetic particles form SSG, initially, and then even superferromagnetic phase. Fig. 6.6, we show the signature of the memory effect at different temperatures – measured using a 'stop-and-wait' protocol - within a range below the blocking temperature (T_B>350 K) of the system. The dips at different T_w are the signature of memory effect at different temperatures. It has been shown earlier that this memory effect is an unequivocal signature of the presence of SSG moments in the system. However, the dip broadens and the memory effect weakens as thetemperature is raised. This is because of enhanced thermal effect on the spin structure of the system.
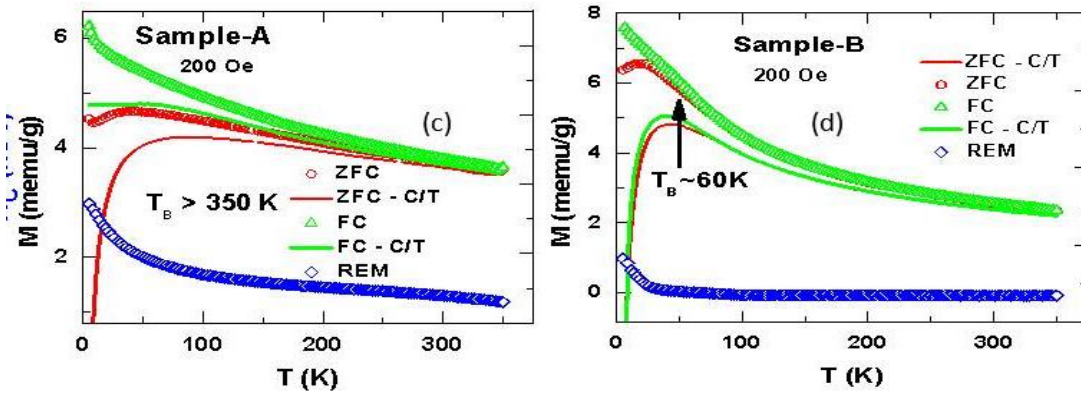
Fig. 6.8. The zero-field cooled (ZFC), field cooled (FC), and remanent magnetization versus temperature plots for (a) sample-A and (b) sample-B; the solid lines show the ZFC and FC magnetizations after subtraction of the contribution of paramagnetic C/T component in both the cases; T_B turns out to be >350 K for sample-A and ~60 K for sample-B.

The thermal energy induces randomness in the spin structure which, in turn, weakens the memory effect. Interestingly, the memory effect is completely absent above T_B. This observation reflects that, as expected, presence of SSG moments and consequent memory effect is conspicuous at only below the T_B. From the detailed analyses of the microstructure and crystallographic data of the nanocomposite, [107] it has been found out that the $BiFeO_3$ particles are bigger (~112 nm) while the $Bi_2Fe_4O_9$ particles are finer (~19 nm). It has already been reported by others that finer $Bi_2Fe_4O_9$ particles exhibit FM order. The $BiFeO_3$ particles are antiferromagnetic with uncompensated local spins. It has also been observed that there are superparamagnetic domains with a blocking temperature T_B>350 K. The

memory effect, on the other hand, signifies the presence of superspin glass moments. As the interparticle distance reduces and the exchange interaction increases, the superparamagnetic domains give way, initially, to superspin glass phase and then even superferromagnetic phase as well. Therefore, the spin structure in the $BiFeO_3$-$Bi_2Fe_4O_9$ composite appears to be consisting of a FM core and SSG shell interacting with the local moments of the AFM structure of coarser $BiFeO_3$ particles. The exchange interaction among the FM cores of different finer particles is considered to have developed a net FM moment across the entire composite. The AFM structures, on the other hand, could be of various types including ones with biaxiality with respect to the axis of application of the field or exchange-coupled pairs [111]. This, in turn, yields partially hysteretic, fully hysteretic, and non-hysteretic grains. The symmetry of the interface moment, with respect to the direction of applied field, within the ensemble of coupled grains is spontaneously broken *even in the absence of first field of hysteresis loop tracing* via an indirect exchange bias coupling interaction between FM core of $Bi_2Fe_4O_9$ and AFM moments of $BiFeO_3$ through the intermediate SSG moments at the interface.

The dynamics of the spin structure at the interface has been probed for sample-A by studying the training effect on CEB at 5 K for 12 repeating cycles. The dependence of H_E and H_C on the number of repeating cycles (n) is shown in Fig. 6.5b. The CEB obtained under a field H_m of 50 kOe following FC with 50 kOe is shown here. Both the parameters are found to be decreasing monotonically with the increase in n indicating spin rearrangement at the interface. It appears that the empirical law [124] for purely AFM spin rearrangement at the interface $H_E^n = H_E^\infty + k.n^{-1/2}$ with k = 505 Oe and $H_E^\infty = 813$ Oe cannot describe our data well (green line in Fig. 6.5b). Instead,a model [125] which considers a mixed scenario of two different relaxation rates for frozen and rotate-able uncompensated spin components at the interface $H_E^n = H_E^\infty + A_f \exp(-n/P_f) + A_r \exp(-n/P_r)$ (Eqn. 1) (where f and r denote the frozen and rotate-able spin components) fits the data perfectly well (brown line in Fig. 6.5b) and yields the fitting parameters as $H_E^\infty = 761$Oe, $A_f = 1394$ Oe, $P_f = 0.61$, $A_r = 451$ Oe, and $P_r = 3$. The ratio $P_r/P_f = 5$ indicates that the rotateable spins rearrange nearly 5 times faster than the frozenspins. Thus while the 'memory effect' signifies the presence of SSG moments in the nanocomposite, the 'training effect' on CEB shows that the SSG moments reside at the interfaces between FM $Bi_2Fe_4O_9$ and AFM

BiFeO$_3$ particles and influence the SEB and CEB significantly. It is important to mention here that the SEB exhibits negligible training effect within the laboratory time scale (~10^{4}s). This could be because it originates from a stable state under zero field and zero magnetization through spontaneous symmetry breaking.

We further examined the SEB in two other samples with higher (~10%) and lower (<3%) volume fraction of Bi$_2$Fe$_4$O$_9$ (sample-B and C, respectively). The corresponding full hysteresis loops have been shown in Figure 6.7a. The T$_N$ of the AFM component for sample-B and C are ~490 K and ~450 K, respectively. In Fig. 6.7a, comparison of the hysteresis loops among all the three samples (A, B, and C) and in Fig.6.7b SEB are shown.The SEB is found to follow a rather nonmonotonic pattern with the variation in the volume fraction of Bi$_2$Fe$_4$O$_9$ phase. It decreases both with the increase and decrease in the volume fraction of the Bi$_2$Fe$_4$O$_9$ phase. The SEB in all these cases could be observed at only below the respective T$_B$. The T$_B$ decreases down to ~60 K in sample-B because of finer Bi$_2$Fe$_4$O$_9$ particles (~8 nm). The T$_B$, however, could
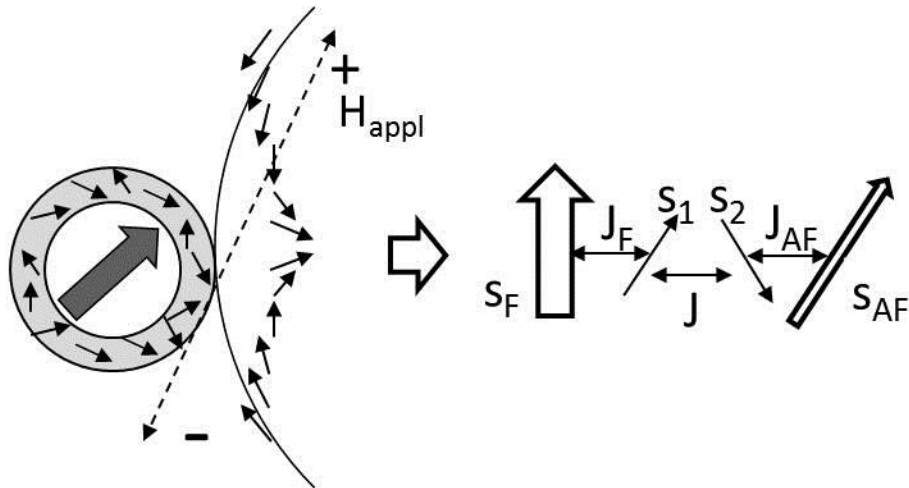
Fig. 6.9. Schematic of the ferromagnetic and antiferromagnetic spin interaction via superspin glass moments at the interface; left part shows the ferromagnetic core of finer Bi$_2$Fe$_4$O$_9$ particle and superspin glass moments at the shell interacting with the local moments of spiral spin spin structure of bigger BiFeO$_3$; right part shows the spin configuration and interaction energies.

not be located within the range 5-300 K for sample-C and, therefore, no exchange bias could be observed in this sample within the same temperature range. The CEB and H_C for sample-B are also found to be finite (Fig. 6.7 c) only at below the T_B (~60K). And as expected, the memory effect too has been observed in sample-B at below T_B. The memory effect, observed both in sample-A and B, implies presence of SSG phase and its influence on the exchange bias. Since superparamagnetic and SSG phases coexist at below T_B in both the samples, one can estimate the relative volume fraction of the SSG phase by calculating the ZFC and FC magnetic moment versus temperature pattern after subtracting the contribution of Curie paramagnetic component C/T (C = Curie constant) from the experimental result (Figs 6.8 a and b) and noting the flatness of the FC moment versus temperature pattern [125] at below T_B. The calculated patterns (solid lines) for both the samples A and B are shown in Figs. 6.8 a & b, respectively. It appears that the volume fraction of SSG phase is higher in sample-A than in sample-B. The SEB too is higher in sample-A than in sample-B. Clear correlation between the volume fraction of the SSG phase and the extent of SEB shows that the SSG phase plays a major role in inducing SEB. We show that all these results could be qualitatively understood by considering a model of "superinteraction bias coupling" between the superspin of superparamagnetic core of finer $Bi_2Fe_4O_9$ and local uncompensated moments of the AFM order in coarser $BiFeO_3$ particles via SSG shell at the interface. The model is shown schematically in Fig. 6.9 and draws essentially from the model proposed in Ref. 112. The dotted line marks the direction of the applied field. The shell SSG moments s_1 and s_2 are coupled to the FM moment S_F by a coupling parameter J_F and to the AFM moment S_{AF} by J_{AF} while the coupling between s1 and s2 is J. The net coupling parameter b will depend on J_{AF}, J_F, and J and, finally, H_E / b [114]. It has been shown [114] that the random fields generated by spin glass moments at the core can act on the saturated FM moment and set the UA via RKKY interaction. The model that we are proposing in the present case is the following. The random field from frozen SSG moments appears to be inducing a variation in the anisotropy of the AFM moments including biaxiality with respect to the direction of the applied field. Thus depending on the orientation of the principal easy axes of AFM grains with respect to the direction of the applied field, the AFM grains can experience either no torque or large torque. Accodingly AFM grains set the UA, primarily, in a direction opposite to that of the

applied field. The SEB, then, becomes negative - i.e., depending on the sign of the starting field for loop tracing, positive (negative), the SEB turns out to be negative (positive). Application of the first field for tracing the loop breaks the symmetry among the AFM grains and sets the UA. The FM moments are assumed to be saturated under the applied field. However, the most interesting aspect is that there is a spontaneous symmetry breaking as well, driven by the random field of the SSG moments at the interface which yields global minima in the energy landscape and sets the UA universally along the negative field direction even in absence of first field of loop tracing. These grains are thus always partially hysteretic along the negative direction of the applied field. The grains which set the UA in a direction opposite to that of applied field are partially hysteretic for both the directions of applied field. But the ones mentioned above are partially hysteretic only with respect to the negative field direction. This aspect, in fact, gives rise to the observed asymmetry in both SEB and CEB with $|-H_{Ep}| > |+H_{En}|$ and has not been reported by others so far in the context of either SEB or The role of SSG moments, therefore, appears to be crucial in inducing this spontaneous symmetry breaking and setting the UA universally along the negative field direction. Alternatively, similar effect could be observed due to even finer fraction of $Bi_2Fe_4O_9$ particles, because of a distribution in the size, which form super- ferromagnetic (SFM) domains via stronger interparticle exchange interaction [101]. The SSG mediated SFM-AFM exchange interaction within an ensemble of grains with finer fraction of $Bi_2Fe_4O_9$ particles, in that case, could actually give rise to the spontaneous symmetry breaking and set the UA universally along the negative field direction even in absence of first field of loop tracing. Only those grains, then, are responsible for giving rise to the observed asymmetry in SEB and CEB. The temperature dependence of SEB is nonmonotonic as at well below T_B, the increase in temperature increases the interaction between SSG and AFM moments which, in turn, induces the energy landscape necessary to set the UA in the system. The bias as well as the asymmetry, therefore, increases. However, as the T_B is approached, the number of grains turning superparamagnetic increases which, in turn, reduces the bias. The nonmonotonic variation in SEB with the volume fraction of $Bi_2Fe_4O_9$ phase, likewise, can be explained by considering nonmonotonic variation in the volume fraction of the SSG phase.

The tunable spontaneous exchange bias of ~300-600 Oe across 5-300 K in nanocomposite of $BiFeO_3$ (~94%) - $Bi_2Fe_4O_9$ (~6%)(Sample A) originates from a superinteraction bias coupling between ferromagnetic core of finer $Bi_2Fe_4O_9$ (~19 nm)
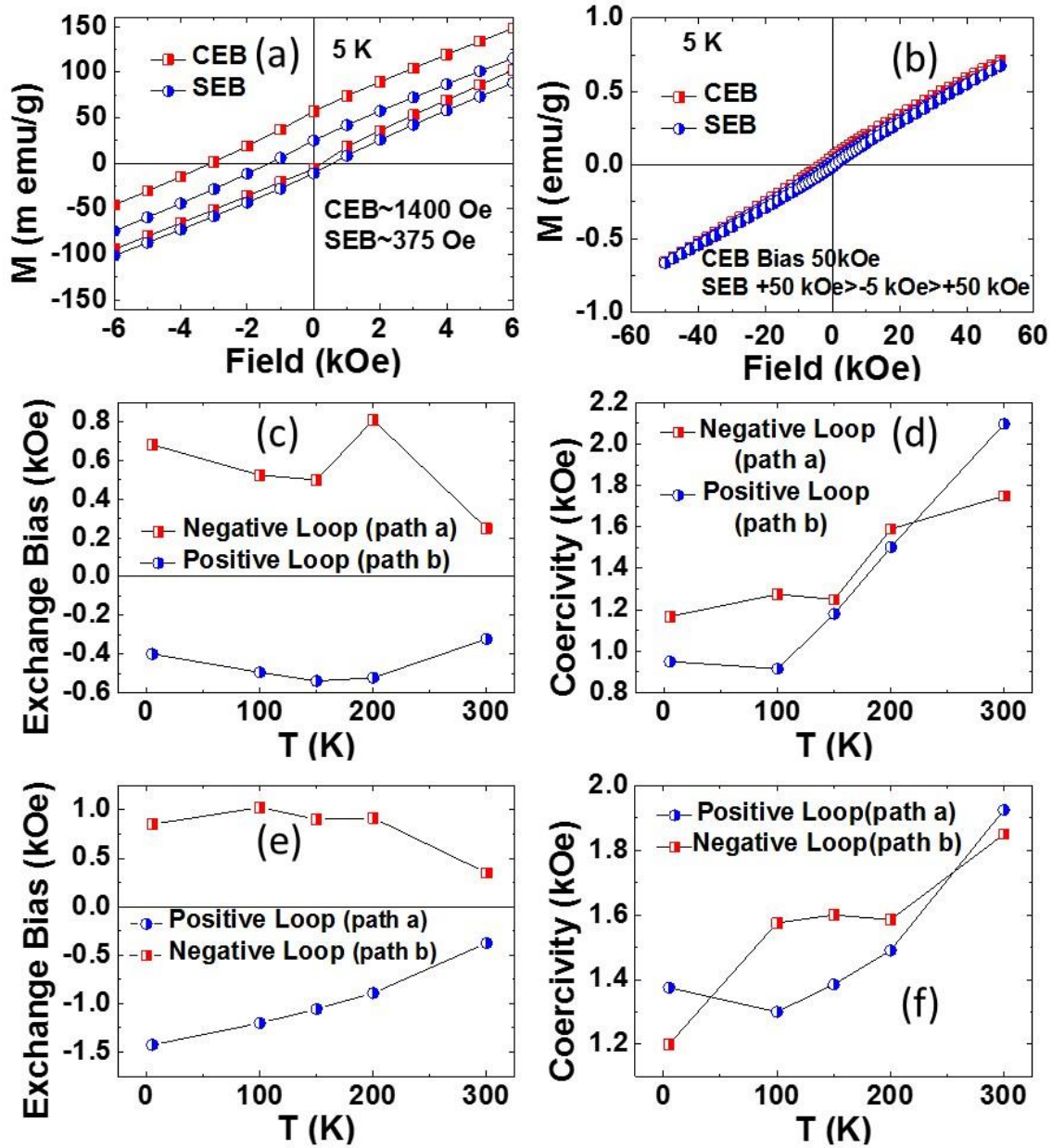
Fig. 6.10. The path dependency of (a) spontaneous exchange bias and (b) corresponding coercivity as a function of temperature; the path dependency of (c) conventional exchange bias and (d) corresponding coercivity as a function of temperature.

particles and antiferromagnetic moment in coarser (~112 nm) BiFeO3 particles via superspin glass moments at the interface. Since it induces a variety of coupling across the interfaces and thus develops a complicated interaction energy landscape among the FM/AFM grains by breaking the symmetry spontaneously even in the absence of first field of loop tracing, the presence of superspin glass moments turns out to be crucial. This giant and tunable (i.e., path dependent) exchange bias can be utilized for an enormous improvement in the efficiency of switching the magnetic anisotropy in a ferromagnetic system electrically via "exchange coupling mediated multiferroicity" in such a nanocomposite and/or a multilayer thin film systems.

While the conventional exchange bias (CEB) is observed under field cooling which sets the unidirectional anisotropy across a ferromagnet (FM) – antiferromagnet (AFM) interface prior to the measurement of the hysteresis loop, the spontaneous one is observed even in an unmagnetized state following zero-field cooling. It results from a symmetry breaking across the FM-AFM interfaces and setting of the unidirectional anisotropy (UA) under the first field of the hysteresis loop tracing. In recent times, the spontaneous exchange bias (SEB) has been reported for different alloy and nanoparticle composite systems [111]. The origin of this appears to be lying in the biaxiality of AFM grains and variation in the FM-AFM bias coupling among an ensemble of grains. We have observed an even more interesting feature of the SEB - variation in the magnitude of the bias depending on the path followed in tracing the hysteresis loop - in a nanocomposite of $BiFeO_3$-$Bi_2Fe_4O_9$. The hysteresis loop has been traced following two paths - +H*max*→-H*max* →+H*max* (path a) and -H*max* →+H*max* →-H*max* (path b); H*max* is the maximum field applied for tracing the loop. This *asymmetry* in the SEB offers an additional tunability apart from the magnitude of the maximum field itself and has not been reported for any other composite or multilayer system exhibiting exchange bias. We have also measured the CEB and found that CEB too, exhibits such a path dependency. The asymmetry in the SEB and CEB - ΔH*SEB* and ΔH*CEB* – is found to be temperature dependent; while ΔH*SEB* decreases with temperature nonmonotonically the ΔH*CEB* decreases rather monotonically. We have found that the SEB, CEB and their path dependency are originating from a spontaneous breaking of the symmetry of interface magnetic moment and setting of UA among an ensemble of FM and AFM particles *even in the absence* of first field of hysteresis as a result of superspin

glass (SSG) mediated exchange bias coupling interaction. The presence of SSG moment is revealed by a significant memory effect in a stop-and-wait protocol of measurement. The memory effect turns out to be dependent on the temperature. The $BiFeO_3$-$Bi_2Fe_4O_9$ nanocomposite has been prepared by a solution chemistry route. The volume fraction of the $Bi_2Fe_4O_9$ phase has been varied from <3% to ~10%. The exchange bias is maximum for a composite of <6 vol% $Bi_2Fe_4O_9$. It decreases both with the increase and decrease in the volume fraction of the $Bi_2Fe_4O_9$ phase.
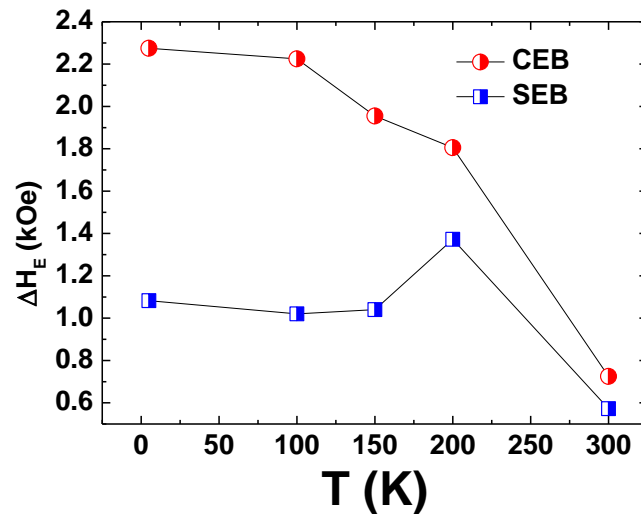
Fig. 6.11. The asymmetry in SEB and CEB -ΔH_{SEB} and ΔH_{CEB}- as a function of temperature; ΔH_{SEB} exhibits a peak around 200 K while ΔH_{CEB} is rather monotonic across 5-300 K.

We have also measured the SEB following a thermal cycling under zero field through ~800 K which is far above the magnetic transition point T_N(~590 K) of the composite, in the VSM system for confirming the unbiased state of the sample in MPMS. Further we discuss here the results obtained for the nanocomposite with <6 vol% $Bi_2Fe_4O_9$ which exhibits maximum exchange bias. Spontaneous and conventional exchange bias areobserved across a temperature range 5-300 K. We discuss the path dependency of the SEB and CEB and its temperature dependence. In Fig. 6.10a, we show the SEB and CEB by blowing up the portion of the loop near origin. The corresponding full loops are shown in Fig. 6.10b. Figs. 6.10c,d,e, and f show the SEB and CEB for a maximum field of 5T measured following two different paths of tracing the loop - path a and path b (Fig. 6.10 b). Quite clearly both

the exchange bias H_E and the coercivity H_C appear to be depending on the path of loop tracing and temperature (Fig. 6.10). The sign of the H_E is negative (positive) for positive (negative) starting field. In Fig. 6.11, we show the asymmetry in the SEB and CEB - ΔH_{SEB} and ΔH_{CEB}- as a function of temperature across 5-300 K. The ΔH_{SEB} exhibits a nonmonotonic pattern with a peak around 200 K. The ΔH_{CEB}, of course, decreases with the increase in temperature rather monotonically. We have also measured the CEB using different maximum field Hm. In Fig. 6.12, we show the Hm and temperature dependence of CEB and corresponding H_C. Interestingly, while H_{CEB} decreases monotonically with the increase in temperature for different Hm 1, 3, 5T, the corresponding H_C exhibits a rise
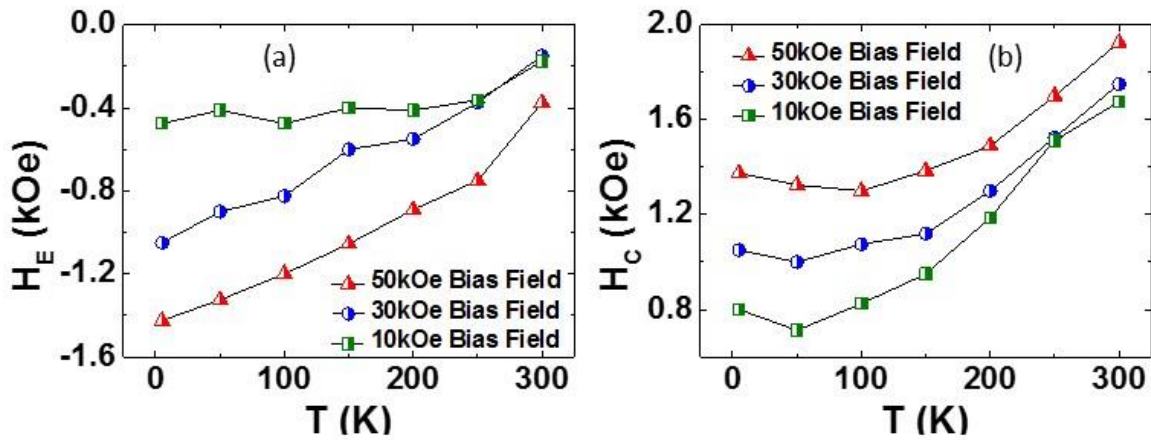
Fig. 6.12. The temperature dependence of (a) conventional exchange bias and (b) corresponding coercivity; there is an anticorrelation between H$_{CEB}$ and H$_C$ throughout the entire range of Hm and temperature; while H$_{CEB}$ decreases with the increase in temperature, H$_C$ increases.

with temperature from above ~50 K. Therefore, there appears to be an anticorrelation between H_{CEB} and H_C. This anticorrelation signifies an anticorrelation between the UA of the exchange coupled structure and the magnetocrystalline anisotropy of the FM component. The magnetocrystalline anisotropy appears to be increasing with the increase in temperature under field cooling. Yet its tensorial nature does not influence the UA of the system. To understand further we investigate second sample BFO-B with blocking temperature (T_B~70K) below room temperature. Figure 6.13(a) shows the zero-field cooled and field cooled (ZFC and FC) magnetization (M) versus temperature (T) plots for Sample-B. Inset shows the dM/dT versus T plots, which help in identifying the blocking temperature T_B. The change in slope of the dM/dT versus T plots below 10 K signifies

weak ferromagnetism [116,117]. Figure 6.13 (b) shows the hysteresis loops measured across 2–100 K. The portion near the origin is blown up to show the asymmetric shift of the loops along the field axis. The exchange bias (H_E) observed in this case is conventional as the measurement has been carried out following field cooling under +50 and −50 kOe. Importantly, the extent of exchange bias turns out the system to be dependent on the sign of the field applied during field cooling
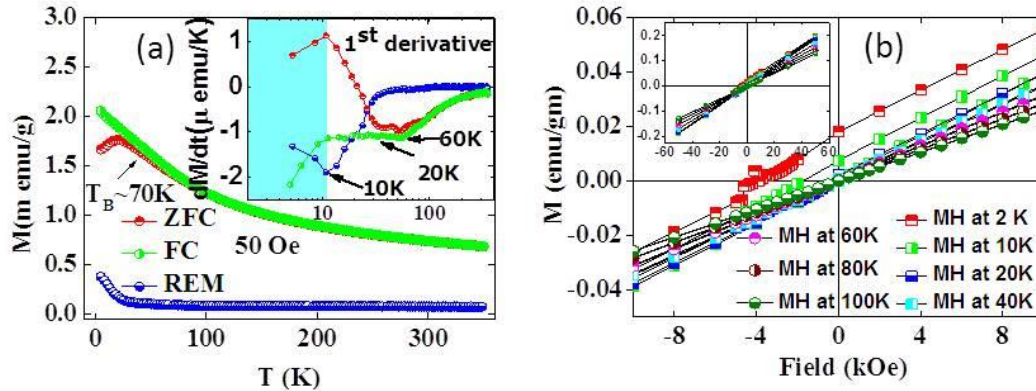
Fig.6.13. (a) The zero-field cooled, field-cooled, and remanent magnetization versus temperature plots; inset shows the dM/dT vs T plots; (b) the hysteresis loop shifts at different temperatures showing the exchange bias; the portion near the origin is blown up; inset shows the full loops.

and also on the path followed in tracing the loop: +50 kOe→0→−50 kOe→0→+50 kOe (positive) or −50 kOe→0→+50 kOe→0→−50 kOe (negative). In Fig. 6.14 (a), we show the asymmetric or path-dependent exchange bias (H_E: H_{Ep}-positive, H_{En}-negative) and coercivity (H_C: H_{Cp}-positive, H_{Cn}-negative) as a function of temperature. The exchange bias is given by $H_E = (H_{c1} + H_{c2})/2$ and the coercivity is given by $H_C = (H_{c1} − H_{c2})/2$, where H_{c1} and H_{c2} are the fields at which the magnetization reaches zero during the tracing of forward and reverse branches of the hysteresis loop.

Further analysis of the hysteresis loops also reveals a vertical shift along the magnetization axis. The vertical shift was earlier observed [118] to be associated with the exchange bias and was resulting from induced net moment. While ferromagnetic coupling across the interface yields a positive shift, antiferromagnetic coupling results in a negative shift. Consistent with the earlier observation [118], the positive shift here is associated with negative exchange bias. However, the asymmetry in the vertical shift was not observed
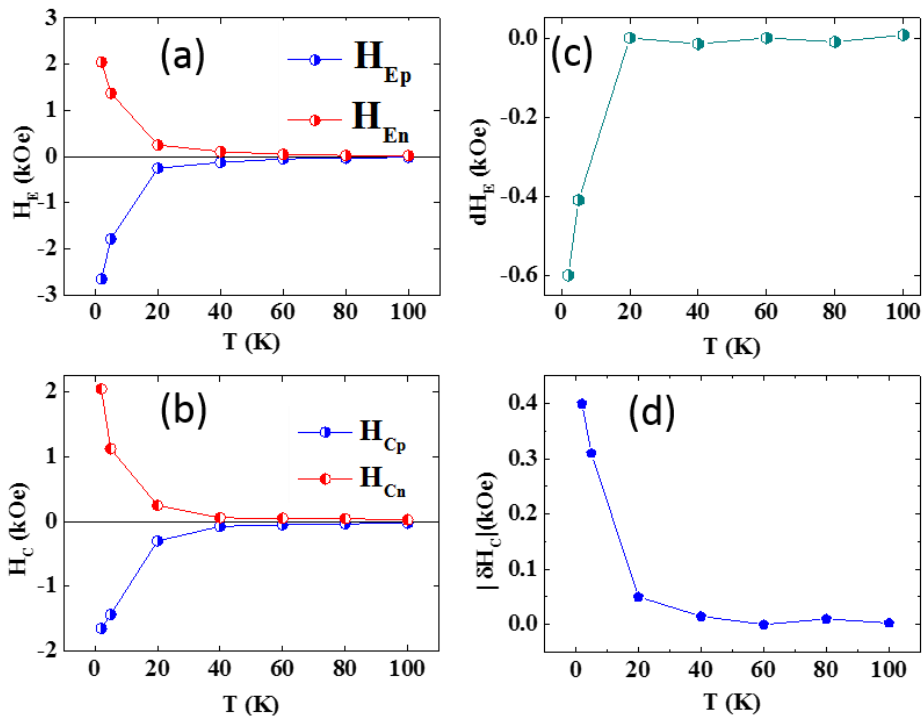
Fig. 6.14. The temperature dependence of (a) exchange bias and (b) coercivity and the asymmetry of (c-d) exchange bias and coercivity across 5–100 K.

between the loops traced via positive and negative paths at 2 K after cooling with +/− 5-T bias field. Finally, the temperature dependencies of the net exchange bias (ΔH_E) and coercivity (ΔH_C) are shown in Figs. 6.14(c) and (d), respectively.
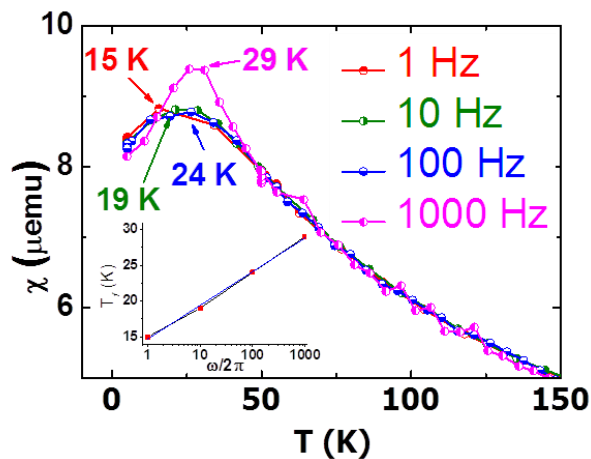
Fig. 6.15. The complex ac susceptibility vs temperature plot at different frequencies; inset shows the shift in the peak temperature with the frequency.

Interestingly, both the H_E and ΔH_E (and likewise H_C and ΔH_C) increase sharply with the decrease in temperature below 20 K. The T_B, however, is 60 K. In between 20 and 60K, exchange bias, coercivity, and their asymmetry are small and exhibit rather weak temperature dependence. In order to probe this observation further, we have carried out ac susceptibility measurements as well. In Fig. 6.15, we show the complex AC susceptibility versus temperature plots for different frequencies. It appears that a distinct
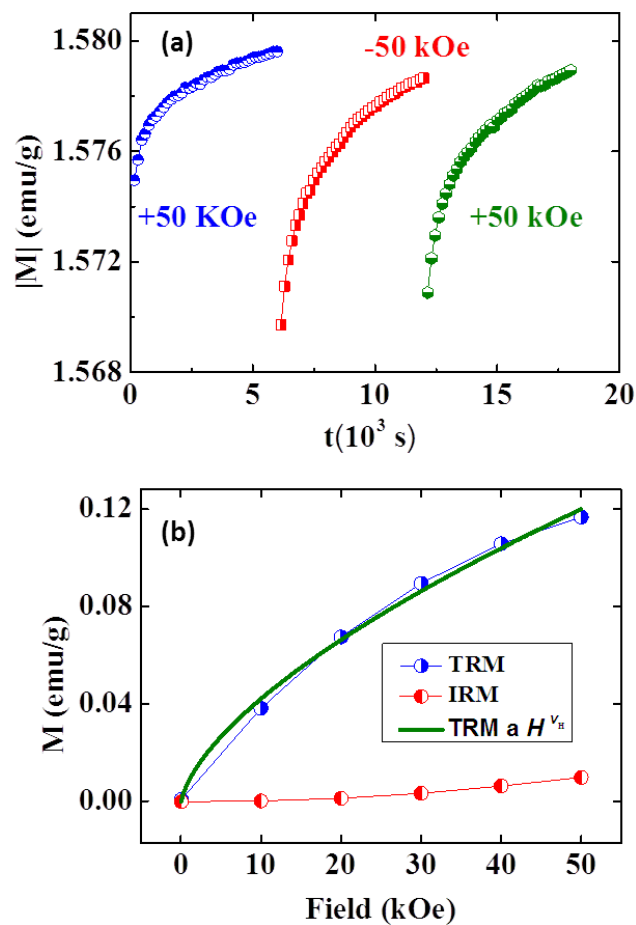
Fig. 6.16. (a) The relaxation of the magnetization measured alternatively under +50 and −50 kOe at 5 K; (b) field dependence of the thermo- and isothermal remanence at 5K.

spin freezing transition takes place around 20 K. The peak temperature $T_f(w)$ shifts towards higher temperature and linearly increases with ln$w$ with the increase of frequencies (inset

Fig. 10), which is a clear signature of spin glass behavior [119]. The frequency sensitivity K of T_f (w) has been calculated to be 4.7. This frequency dependence of T_f (w) is described as conventional slowing down of spin dynamics, which results in the irreversibility in the spin glass [120]. The frequency dependence (inset of Fig. 6.15) of the peak temperature follows the Vogel-Fulcher pattern (Vogel-Fulcher freezing temperature at 29.4 K for $BiFeO_3$) [121]. Previous reports suggest that at low-temperature BFO possess low-temperature spin glass ordering, which leads to the increase of H_B and H_C at low temperature [121]. This result shows that the onset of spin-freezing transition has a strong bearing upon the exchange bias and its asymmetry. In order to probe the spin morphology of the system, we have carried out detailed magnetometry across 2–300 K.

We have studied the relaxation of the moment at 2 K over a time span of 3600 s under both +50 and −50 kOe. The sample was first cooled down from 350 to 2 K under zero field and then +50 kOe was applied and the time dependence of the moment was measured for 3600 s. After that, the field was ramped down to50 kOe and the magnetizationwas measured for 3600 s. Again, the field was ramped back to +50 kOe and the measurement was repeated for 3600 s. The results of these three measurements are plotted in Fig. 6.16(a). They clearly show an upward creep signifying incoherent rotation of the ferromagnetic moment because of the presence of superspin glass (SSG) at the interface [129, 133]. Additionally, in this high field relaxation process, we observed that the amount of variation in magnitude of moments (M) in 3600 sec relaxation time is almost same for alternative fields. It indicates the uniaxiality (UA) of ferromagnetic grains. Thus the asymmetry in exchange bias does not come from the FM part of the composite. The possible reason of asymmetry could be the existence of random anisotropy at the interface of $BiFeO_3$- $Bi_2Fe_4O_9$ and interactions with uniaxial anisotropy of very small size of the ferromagnetic domains through a nontrivial interface spin structure where the exchange bias coupling freezes below the Vogel-Fulcher freezing temperature. The presence of super spin glass was also investigated in memory effect on ZFC magnetization measured by well-designed stop and wait protocol. The characteristic peak in the differential moment versus temperature plot at a temperature at which the measurement was stopped and waited for 10^4 s signifies presence of SSG in the system. We further carried out isothermal remanence and thermoremanence measurements at 5 K. For the thermoremanence measurement, the sample was cooled down

from room temperature to 5 K under a specific field and then the field was removed. The remanent moment was measured immediately. The isothermal remanence was measured following zero field cooling. In this case, the sample was brought down to 5 K from room temperature under zero field and momentarily a field was applied at 5 K.
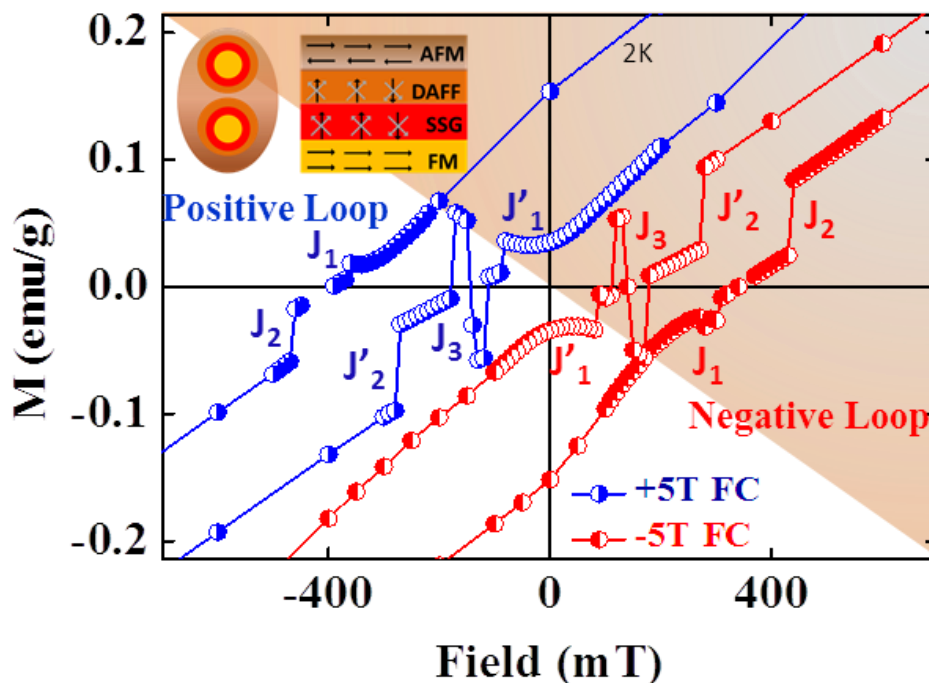
Fig.6.17. The hysteresis loops measured at 2 K following different protocols starting with +50 kOe (blue line) and −50 kOe (red line); anomalous jump structures could be seen in different branches of the loops; inset shows the spin structure.

Then the field was removed and the magnetization was measured. The field dependence of both the thermo- and isothermal remanence at 5 K is shown in Fig. 6.16(b). Very interestingly, the patterns follow closely those expected for a two-dimensional dilute antiferromagnet in a field (DAFF) [134]. While the isothermal remanence exhibits a weak field dependence, the thermoremanence follows $\propto H^{vH}$ pattern where $vH = 0.64$. In the case of spin glass [128], the isothermal remanence curve increases with field relatively sharply and exhibits a peak at an intermediate field and meets the thermoremanence curve and then both saturate at higher field. For superparamagnetic system [129], the thermoremanence curve increases with field quite rapidly. For the present case, the results of thermoand isothermal remanence measurements indicate presence of two-dimensional DAFF. The

high-field relaxation process and memory effect on ZFC magnetization, on the other hand, signify simultaneous presence of SSG. The overall spin morphology, therefore, appears to be consisting of four components: ferromagnetic (FM) and antiferromagnetic (AFM) cores and interfaces vitiated by SSG and DAFF shells.

Finally, we have measured the hysteresis loops with higher resolution at 2 K starting from +50 kOe and from −50 kOe. The loops, especially the portion near the origin, are shown in Fig. 6.17. Quite conspicuous are the sharp jumps in the loops. Such jumps have earlier been observed in systems containing inhomogeneities and thus random anisotropy [130-132]. In fact, both by experimental and theoretical work, it has been shown that depending on the strength of the random anisotropy with respect to the exchange coupling, several jumps might be seen in hysteresis loops at low temperature. Because of thermal perturbation, they smear off at higher temperature. In the present case too, loops measured at higher temperature (5 K) exhibit lesser number of jumps and complete smearing off eventually at temperature higher than that. However, there is an interesting distinction between the jumps observed in a ferromagnetic system containing purely random anisotropy because of inhomogeneities and the jumps observed here. The number of jumps observed, in the present case are different in two different branches of a particular loop. The inversion symmetry, normally observed in systems containing purely random anisotropy [131], is broken here. While lesser jumps (J_1, J_2) could be seen in the forward branch, more jumps(J_1, J_2, J_3) are conspicuous in the reverse branch (Fig. 6.15). This is true for both the loops—whether the loop has been traced starting from+50 or−50 kOe. There is, however, conspicuous inversion symmetry in the jump structure in between two forward and two reverse branches of the loops traced starting from +50 and −50 kOe. It is possible to notice that the branch on the extreme left (blue line) is a mirror image of the branch on the extreme right (red line) of Fig. 6.17. Likewise, the inner blue and red branches are also mirror images of each other. Such an asymmetric pattern of jumps for a particular loop yet a symmetric one between the loops traced via two different protocols is remarkable and has not been reported earlier. This observation clearly points out that there could be a correlation between this symmetry of the jump pattern and the protocol dependency of the exchange bias. It has been argued below that these results from a local topological spin texture at the interface which, in turn, gives rise to a strong universal unidirectional

anisotropy of the interface moment along negative field direction. It has been shown that random anisotropy due to inhomogeneities leads to jumps in the hysteresis loop at a very low temperature (100–500 mK) as a result of avalanches in domain flipping.[132] The random anisotropy field competes with the applied field and as and when the spins are aligned with the local anisotropy, the avalanche takes place. The role of local anisotropy has been addressed both by site-centric local random field model [130] as well as cluster model [132]. The Hamiltonian considers the exchange coupling among the spins, local random field due to anisotropy, and the applied field.

In the case of the present system, exhibiting exchange bias, exchange coupling interaction across the interface between the $BiFeO_3$ and $Bi_2Fe_4O_9$ particles should also be considered. This is strongly influenced by the SSG and DAFF layers at the interface. While $BiFeO_3$ crystallizes in rhombohedral structure with R3c space group, $Bi_2Fe_4O_9$ crystallizes in orthorhombic structure with Pbam space group. The interface, therefore, creates a certain topology that induces, at least, a local spin texture even though globally the salient features of the SSG and DAFF are retained. Therefore, in presence of such local spin texture, both random and textured anisotropy fields compete with the applied field and the exchange coupling interaction across the interface. The domain flipping and avalanche along two different pathways is not identically influenced. The textured anisotropy creates a self-generating interfacial moment, which acts upon the exchange coupling interaction in between $BiFeO_3$ and $Bi_2Fe_4O_9$ and sets the universal unidirectional anisotropy along the negative direction of the applied field. This loss of randomness and preferred orientation of the local anisotropy breaks the inversion symmetry of the jump structure in the hysteresis loop. The net interface moment from this textured anisotropy and development of unidirectional anisotropy of the interface moment toward negative direction of the applied field as a consequence lies at the heart of the path dependency of exchange bias. In fact, this asymmetric jump structure in the hysteresis loop at 2 K is the first clear proof of the presence of textured pattern of anisotropy at the interface between ferromagnetic and antiferromagnetic cores which appears to generate the self-generating interface moment along a preferred direction with respect to the direction of the applied field. Topological spin texture in the form of magnetic vortices carrying an electric charge (skyrmion) could earlier be identified in chiral lattice system [133]. The random as well as the textured

anisotropy is strong enough as their influence on the hysteresis loop could be seen at a temperature as high as 2 K. In other ferromagnetic systems with local inhomogeneity [132], influence of random anisotropy could be seen at even lower temperature (100–500 mK). It is also important to mention here that the influence of this local spin texture in inducing a net interface moment is observable only below the spin freezing temperature, i.e., the Vogel-Fulcher freezing temperature at 29.4 K for $BiFeO_3$. The spin structure at the interface needs to be frozen in order to create strong local field. As the temperature is raised toward~29.4 K from below, influence of the interface spin morphology as well as the net interface moment weaken and so the exchange bias and its path dependency.

This spontaneous setting of UA along the negative direction of applied field (or universal UA) even under zero field is the origin of the path dependency for both SEB and CEB. The volume fraction of the partially hysteretic grains V_{fg}^{UUA} with universal UA (UUA) along the negative direction of the applied field governs the magnitude of exchange bias as well as its path dependency. The volume fraction of the partially hysteretic grains V_{fg}^{UA} with UA set by the first field of the loop tracing, on the other hand, governs the magnitude of exchange bias but not the path dependency. The temperature dependences of V_{fg}^{UUA}(T) and V_{fg}^{UA}(T) and their subtle interplay influence the temperature dependence of ΔHSEB and HSEB. The nonmonotonicity in both H$_{SEB}$ and ΔH$_{SEB}$ possibly results from an initial increase in V_{fg}^{UUA} and V_{fg}^{UA} with temperature due to an increase in SSG mediated indirect exchange bias coupling amongthe grains. As the temperature increases, the frozenmoments of SSG at the shell in between FM and AFM grains are thermally activated to interact strongly withthe FM and AFM moments. This strong interaction, inturn, makes the spontaneous symmetry breaking moreeffective and gives rise to enhanced path dependencyin SEB. With further rise in temperature, the V_{fg}^{UUA} eventually decreases as enhanced thermal randomization of the spin structure itself results in weakening of bias coupling interaction. This anomalous influence of temperature is not conspicuous in the case of CEB as in this case both the UUA and UA are further influenced by field cooling from higher temperature. The impactof field cooling masks the subtle role of temperatureon SSG induced spontaneous setting of UA. In fact, as shown in Fig. 6.10, apart from its path dependency, the CEB itself does not exhibit any nonmonotonicity across 5-300 K.The ΔH$_{SEB}$ and ΔH$_{CEB}$ offer an

additional tenability to the exchange bias. Using a combination of maximumfield of loop tracing (H*m*) as well as the path followed intracing the loop - positive or negative - it is possible totune the magnitude of the exchange bias. This tunability, in turn, can increase the functionality in electrically switching the magnetic anisotropy of a ferromagnetic systemin a $BiFeO_3$-ferromagnetic composite like the present one via multiferroic coupling between ferroelectric polarization and magnetization in $BiFeO_3$.

6.5. Summary

In summary, we report that in a nanocomposite of (~94 vol %) $BiFeO_3$-(~6 vol%) $Bi_2Fe_4O_9$ with finer and ferromagnetic $Bi_2Fe_4O_9$ particles and coarser and antiferromagnetic BiFeO3, one observes a large and path-dependent spontaneous exchange bias (~30-60 mT) across 5-300 K. The conventional exchange bias too is found to be path dependent. This path dependency offers an additional tunability in the effect of electrical switching of magnetic anisotropy in a $BiFeO_3$-ferromagnetic composite via multiferroic coupling and is expected to improve the functionality of such a device enormously. The net interface moment from textured anisotropy and consequent path dependency of the exchange bias is quite an attractive proposition as it offers tunability to the exchange bias depending on the path followed in tracing the hysteresis loop. Since $BiFeO_3$ is a well-known room temperature multiferroic, it is possible to switch the magnetic anisotropy of the ferromagnetic component by applying electric field. Tunable exchange bias then helps in tuning the extent of switching and thus increases the functionality manyfold. In summary, we show that a textured pattern of magnetic anisotropy forms at the interface between ferromagnetic $Bi_2Fe_4O_9$ and antiferromagnetic $BiFeO_3$ nanoparticles from shells of superspin glass and dilute antiferromagnet in a field. The local field from this texture generates net interface moment to set the unidirectional anisotropy along a preferred direction with respect to the direction of the applied field. Such a spontaneous onset of nonswitchable unidirectional anisotropy under field appears to be the origin of the path dependency of the exchange bias. The textured anisotropy at the interface also yields an asymmetric pattern of sharp jumps in the hysteresis loop at low temperature. Thus a direct correlation could be established between the asymmetric jump structure in the hysteresis loop at low temperature and the

path dependency of the exchange bias. Instead of a "clean" interface between ferromagnetic and antiferromagnetic grains, an interface with coexisting local spin texture and random anisotropy emerging out of superspin glass and dilute antiferromagnet in a field, therefore, offers a rare tunability to the exchange bias via its path dependency and, thereby, increases its utility for device applications many fold.

7. Chapter - Tunable inverted hysterisis loop

7.1. Introduction:

In magnetism the shift of hysteresis loop, so called exchange bias (EB) was first observed by Meiklejohn and Bean [18] in ferromagnetic (FM) Co particle encapsulated with antiferromagnetic (AFM) CoO. For more than a half century this phenomena has been studied due to its potential applications in giant magneto resistance (GMR) [134], spin valve [135], high density storage media [136] etc. as well as for fundamental studies. The conventional way to induce exchange anisotropy, named exchange bias (EB) is to cool down a magnetically uncompensated AFM-FM interface below *Neél* Temperature (T_N) of AMF and Curie Temperature (T_C) of FM where $T_N < T_C$. A unidirectional shift of hysterics or exchange bias should be observed in exchanges coupled FM-AFM interface. In most cases the exchange bias is observed in the direction of cooling field, which is called positive EB. Due to the AFM-FM interaction, the FM spins intend to point in the direction of the cooling field at low temperatures below T_N. In some cases due to the large unidirectional anisotropy of AFM, the AFM-FM interfacial interaction biases FM spins to the opposite direction of cooling field and causes a loop shift in opposite direction causing negative exchange bias. In addition an enhancement of coercivity is also observed [21-24]. However, for large cooling field the same sample provide positive exchange bias where this large cooling field is required to reverse the magnetically easy direction of the unidirectional anisotropy to produce positive exchange bias in pure metal or metal-fluoride materials. [22] Later, it was found that ferromagnetic/ferromagnetic transition-metal rare earth alloy thin films can exhibit both positive and negative exchange bias based on their composition, most importantly charge distribution at the interface. [138,139]. Then the biasing process entirely depends on the competition between Zeeman energy of surface spins at the interface and antiferromagnetic exchange interaction strength between FM and AFM spins.

A common characteristic in a hysteresis loop is that the magnetization does not decrease to zero but remains positive while the applied field is decreased from its value at positive saturation to zero [140]. The abnormal hysteresis behavior of ferromagnetic (FM) materials

was first observed by Esho in 1976 in amorphous Gd-Co films which showed a negative remanence and inverted hysteresis loop behaviour [141]. This means that instead of traversing anti-clockwise the hysteresis loops progress in a clockwise direction and display a negative remanence and coercivity. This anomalous hysteresis behavior is called inverse hysteresis loop (IHL) which also was observed in many other systems. This phenomenon has commonly been observed in inhomogeneous systems, such as exchange-coupled multilayers and soft/hard magnetized materials, [142-146] even in a simple homogeneous system like epitaxial Fe films [147] and a single domain particle with two competing anisotropies. [148, 149] The origin of the IHL has been explained through several proposed mechanisms based on coupling effects such as magnetostatic interaction, the antiferromagnetic coupling, and the competition of two anisotropies. [142-144,146-149]

In this chapter we describe direct observation of counter-clockwise or normal hysteresis loop and clock wise or inverted hysteresis loop formation in the Ni,Fe solid solution with very low coercivity and large positive exchange bias. These two opposite (counter-clockwise/clockwise) hysteresis loop formation manifest depending upon the field range of hysteresis loop measurement. Like most of the positive exchange bias systems $Ni_{50}Fe_{50}$ shows positive shift at the field direction when the loop tracing field range is small (just above the saturation field) and the loop is counter-clockwise. Furthermore, when the film is measured with a higher loop tracing field range, we measure a typical clockwise hysteresis loop with no exchange bias. We found that the origin of this interesting phenomenon of dual type of hysteresis loop (counter-clockwise/clockwise) observation by hysteresis loop measurement protocol with different field ranges depends on the microstructure of $Ni_{50}Fe_{50}$. To investigate the origin of this unique and interesting IHL phenomenon we have performed a detailed microstructure and composition analysis along with thorough magnetic measurements in SQUID magnetometry. The Ni,Fe solid solution behaves like admixture of antiferromagnetic (AFM) phase and $Ni_{50}Fe_{50}$ naturally behaves as ferromagnetic (FM) material. At low field measurement range the interface acts like typical FM-AFM interface and permits positive exchange bias. This AFM coupling at interface can be overcome with a large field and AFM spins can be aligned like FM spin. Thus the AFM-FM system behaves like FM at high field where all spins are aligned in the field direction.

7.2. Sample preparation

Soft ferromagnetic alloy $Ni_{50}Fe_{50}$ thin film was prepared by an electrodeposition process. A seed layer consisting of titanium and copper (Ti/Cu) of thickness 20/100 nm wasfirst sputtered on to the silicon substrate. The electrodeposition was carried out using the same composition of the bath as described by Park and Allen [150]. The bath was composed of 168 gL^{-1} of $NiSO_4$, $6H_2O$, 81 gL^{-1} of $FeSO_4$, $7H_2O$, 135 gL^{-1} of $NiCl_2$, $6H_2O$, 50 gL^{-1} of Saccharin and 3 gL^{-1} of Boric Acid. Saccharin was added to reduce the internal stress in the grown thin film. The film was dc electrodeposited at constant temperature of $57^{o}C$ and at a uniform current density of $30mA/cm^2$, while pH of the electrolytic bath was maintained at 3.7 during one hour of deposition process. Pt mesh with nickel balls inside was used as the anode and 2×1 cm^2 Ti/Cu sputtered diced Si piece was used as cathode, while no air agitation was applied during the deposition process. The thickness of the deposited film is nearly 10 μm as found from the SEM analysis and the composition of the electroplated alloy was measured by energy dispersion spectroscopy (EDS). The composition of the film was found to be Ni 53.5%, Fe 46.5%. Figure 7.1 shows the XRD pattern of the $Ni_{50}Fe_{50}$ thin film sample where θ is the Bragg's angle. Phase analysis shows that the structure is dominated by $FeNi_3$<111> and <200> phases respectively. The grain size of the diffracting sample was calculated using the Scherrer formula [151] $d = K\lambda/\beta\cos\theta$, where d is the grain size, β is an angular width in terms of 2θ and θ is the Bragg angle, and λ is the wavelength of the radiation used and K is the shape factor which is normally 0.94 for crystalline material. The grain size was found to be 78.43 nm. For comparison a $Ni_{45}Fe_{55}$ sample was also prepared at room temperature using the electrolytic bath composed of 0.7M of $NiCl_2,6H_2O$, 0.05M of $FeCl_2$, $4H_2O$, 0.45M of Boric Acid, 0.03M of Saccharin, 4.5 gL^{-1} of 1, 3, 6 - Naphatalene Trisulphonic acid, 5.5 gL^{-1} of Sulfosalycylic acid, 0.5 gL^{-1} of Triton X-100. The film was dc electrodeposited for an hour at room temperature and at a uniform current density of 5 mA/cm^2, while pH of the electrolytic bath was maintained at 2.5. In this case, Pt mesh was used as anode while similar diced Si piece was used as the cathode; also air agitation of 550 rpm was conducted during the entire deposition process. The thickness of the deposited film was found to be 6 μm using SEM analysis and the composition of the alloy was measured to be Ni 47.92% and Fe 52.08% by EDS method.

A comparison of electrolytic bath and deposition conditions of the two alloys has been tabulated in Table 5.

Table 6: Comparison of electroplating conditions for two different alloys

Conditions	$Ni_{50}Fe_{50}$	$Ni_{45}Fe_{55}$
Electrolytic Bath Composition	168 gL^{-1} of $NiSO_4$, $6H_2O$, 81 gL^{-1} of $FeSO_4$, $7H_2O$, 135 gL^{-1} of $NiCl_2$, $6H_2O$, 50 gL^{-1} of Saccharin and 3 gL^{-1} of Boric Acid	0.7M of $NiCl_2,6H_2O$, 0.05M of $FeCl_2$, $4H_2O$, 0.45M of Boric Acid, 0.03M of Saccharin, 4.5 gL^{-1} of 1, 3, 6 - Naphatalene Trisulphonic acid, 5.5 gL^{-1} of Sulfosalycylic acid, 0.5 gL^{-1} of Triton X-100
Current Density	30 mA/cm^2	5 mA/cm^2
pH	3.7	2.5
Temperature	57°C	Room Temperature
Anode	Pt mesh with nickel balls inside	Pt mesh
Method of electroplating	DC	DC
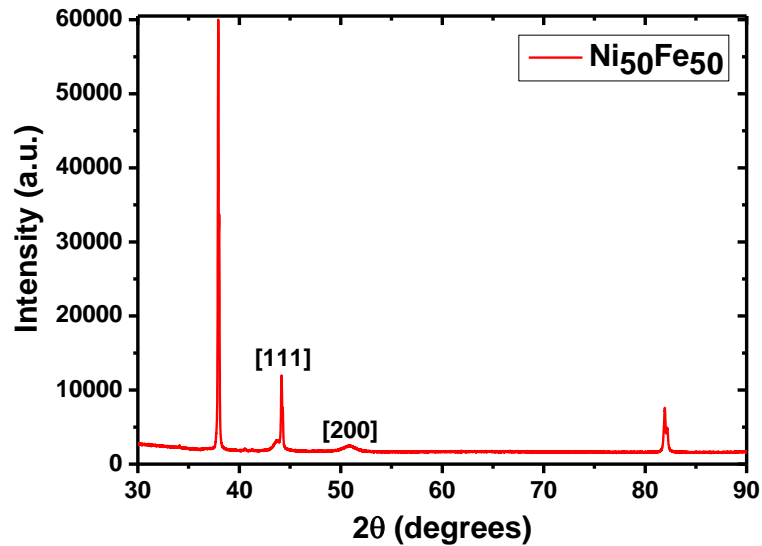
Fig. 7.1. XRD pattern of the $Ni_{50}Fe_{50}$ thin film sample

7.3. Structural anlysis

The microstructure of the film has been investigated by HRTEM. Cross sections were prepared using a Dual Beam Focused Ion Beam (FIB) FEI Helios NanoLab 600i. A 300
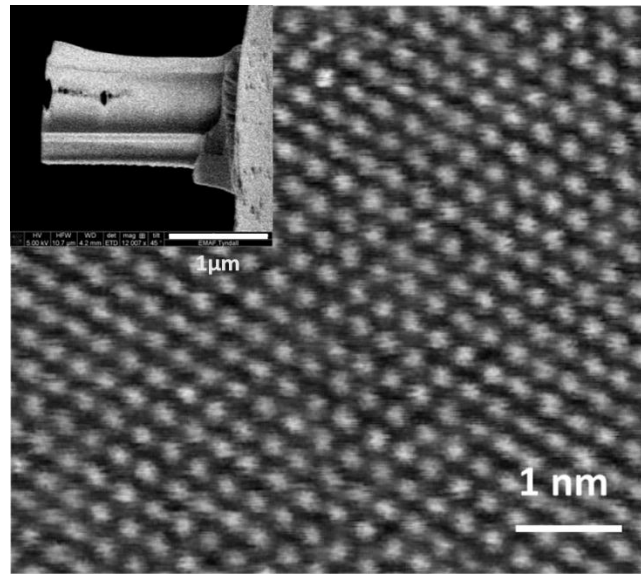
Fig.7.2. Atomic resolution HRTEM image of Ni$_{50}$Fe$_{50}$ thin film. Inset shows thin lamella prepared by Focused Ion Beam (FIB).
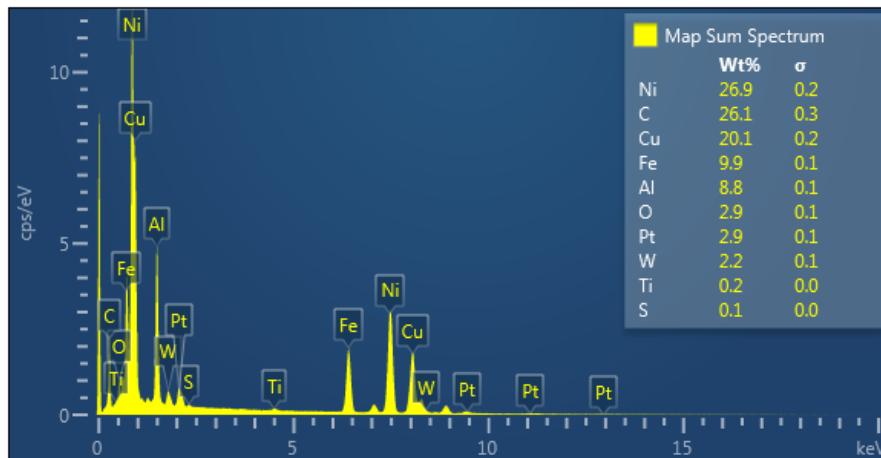
Fig.7.3. EDX elemental analysis of NiFe film at Ni rich region.

nm Pt layer was deposited within the DualBeam FIB by electron beam induced deposition and 2 µm thick Pt layer with ion beam induced deposition. These two layers have been

grown for protection before the milling process. The lamellas were prepared and thinned down for the TEM analysis. Wedge like lamellas were obtained with approximately less than 200 nm thicknesses at the base going to 0 nm at the top edge. The thinning at 30 kV was finished by polishing at 5 kV and 2 kV to reduce the ion-beam
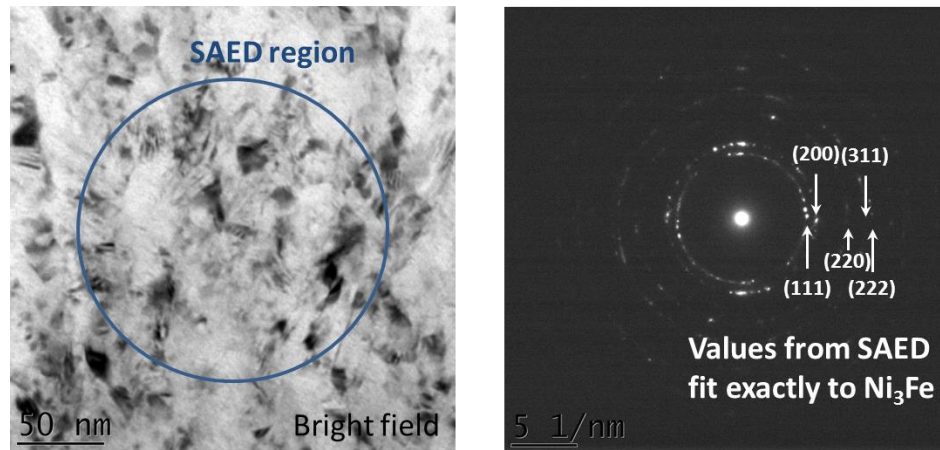
Fig.7.4. Selected area electron diffraction (SADE) image shows exsistance of Ni₃Fe populated region in Ni₅₀Fe₅₀ thin film.

induced damage to a less than 2 nm thin layer on both sides. Both samples show a broad grain size distribution which is in the range from 0 to 30 nm for the $Ni_{50}Fe_{50}$ and 0 to 10 nm for the $Ni_{45}Fe_{55}$. The existence of antiferromagnetic $Ni_{50}Fe_{50}$ solid solution structure with in the matrix of ferromagnetic NiFe has been observed in few places which have been confirmed by TEM-EDS, EELS and SAED analysis (Fig. 7.2, 7.4 &7.3).

7.4.   Magnetic Measurement

It was found that ferromagnetic/ferromagnetic transition-metal rare earth alloy thin films can exhibit both positive and negative exchange bias based on their composition, most importantly charge distribution at the interface. Then the biasing process entirely depends on the competition between Zeeman energy of surface spins at the interface and antiferromagnetically exchange interaction strength between FM and AFM spins. In this present work we have observed counter-clockwise and clock wise hysteresis loop formation in the $Ni_{50}Fe_{50}$ with very low coercivity and large positive exchange bias. No

exchange bias or inverse hysteresis loop was found in $Ni_{45}Fe_{55}$. These two opposite (counter-clockwise/clockwise) hysteresis loop formation in $Ni_{50}Fe_{50}$ thin film depends upon the field range of hysteresis loop measurement. Like most of the positive exchange bias system $Ni_{50}Fe_{50}$ also shows positive exchange bias shift at field direction when the loop tracing field range is small (just above the saturation field) and the loop is also counter-clockwise. When the film is measured with a higher loop tracing field range, it was observed that the hysteresis loop follows reverse path with no exchange bias. We found that the origin of this interesting phenomenon of dual type of hysteresis loop (counter-clockwise/clockwise) observation with different field range hysteresis loop measurement protocol depends on the microstructure of $Ni_{50}Fe_{50}$. To investigate the origin of this unique and interesting phenomenon we have performed a detail microstructure and composition analysis. The Ni,Fe solution behaves like admixture of antiferromagnetic (AFM) phase and $Ni_{50}Fe_{50}$ naturally acts as ferromagnetic (FM). At low field range measurement the interface behaves like typical FM-AFM interface and permits positive exchange bias. This AFM coupling at interface can be overcome with a large field and AFM spins can be aligned like FM spin. Thus the AFM-FM system behaves like FM at high field where all spins are aligned at field direction.

Typical hysteresis loops of NiFe thin film after field cooled (FC) from 350K to room temperature (300K) and low temperature 5K are shown in Fig. 7.5. A bias field of 1000 Oe was applied and it shows positive exchange bias in NiFe system. ±200 Oe field range was used to measured full hysteresis. When the same protocol was followed but with a different field range of ±50,000 Oe a completely different result was observed. Normally a hysteresis loop measurement shows an anti-clock wise MH loop, let call it as counter-clockwise hysteresis. When we measured the same sample after FC with higher field range the MH loop follows a clock wise path (Fig. 7.6-a). Both coercive field (H_C) and remanence magnetization (M_R) are obtained reverse directions. Throughout the discussion we will call it negative hysteresis. No step hysteresis has been found in ±50,000 Oe field range (Fig. 7.6-b). Thus it is clear that the negative coersivity does not come from twisted hysteresis [152]. The positive hysteresis loops measured after +5T and -5T FC at 5K lay exactly on the right and left sides of inverse hysteresis loop (5K) respectively. A range of shaped hysteresis loops with various fields range were measured right after field cooled (FC) with

1000 Oe field at temperature 5K. Hysteresis loops measured with high field range shows negative hysteresis (Fig.7.6-a) whereas low field range shows counter-clockwise s (Fig.7.6-b). The field range dependence of $H_c = (H_{c1} - H_{c2})/2$ and $H_{ex} = (H_{c1} + H_{c2})/2$ of the film are shown in Fig.7.6-c and Fig.7.6-d respectively. The coercivity of the film becomes zero at 688 Oe (Inset figure of Fig.7.6). Thus 688 Oe field is the critical field to switch the hysteresis from counter-clockwise to clockwise. With high field, it is likely that the FM-AFM coupled spins at the interface are broken by field higher than 688 Oe. A field, more than this critical field is able to switch the anisotropy direction of exchange bias coupling (Figure 7.7a). The right half of the inverse hysteresis loop is the part of exchange bias loop where positive starting field works as a bias field and the other half results from the reverse
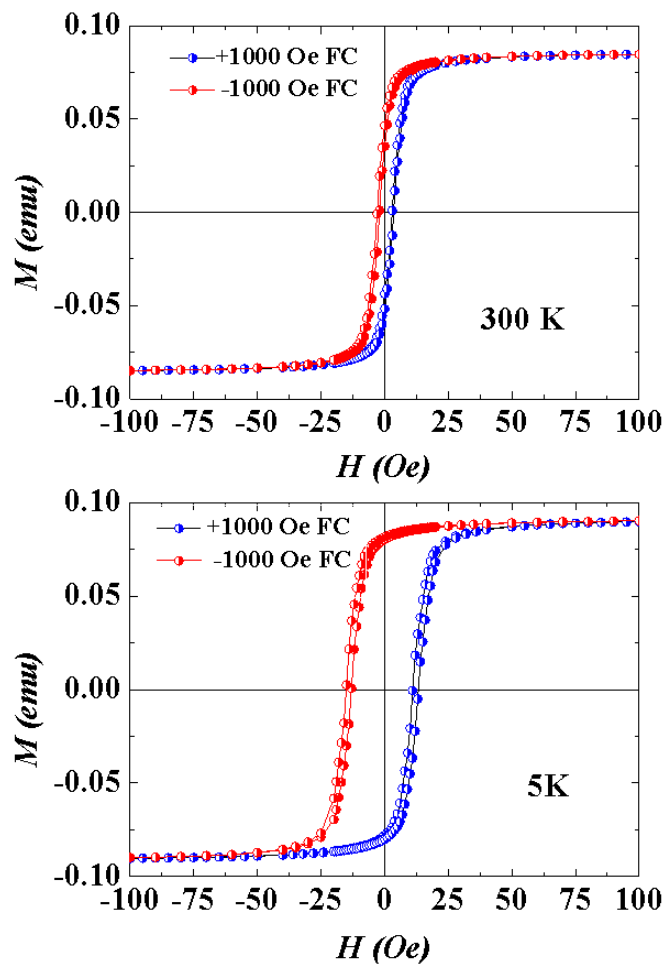
Fig.7.5. Exchange bias at 300 K and 5 K
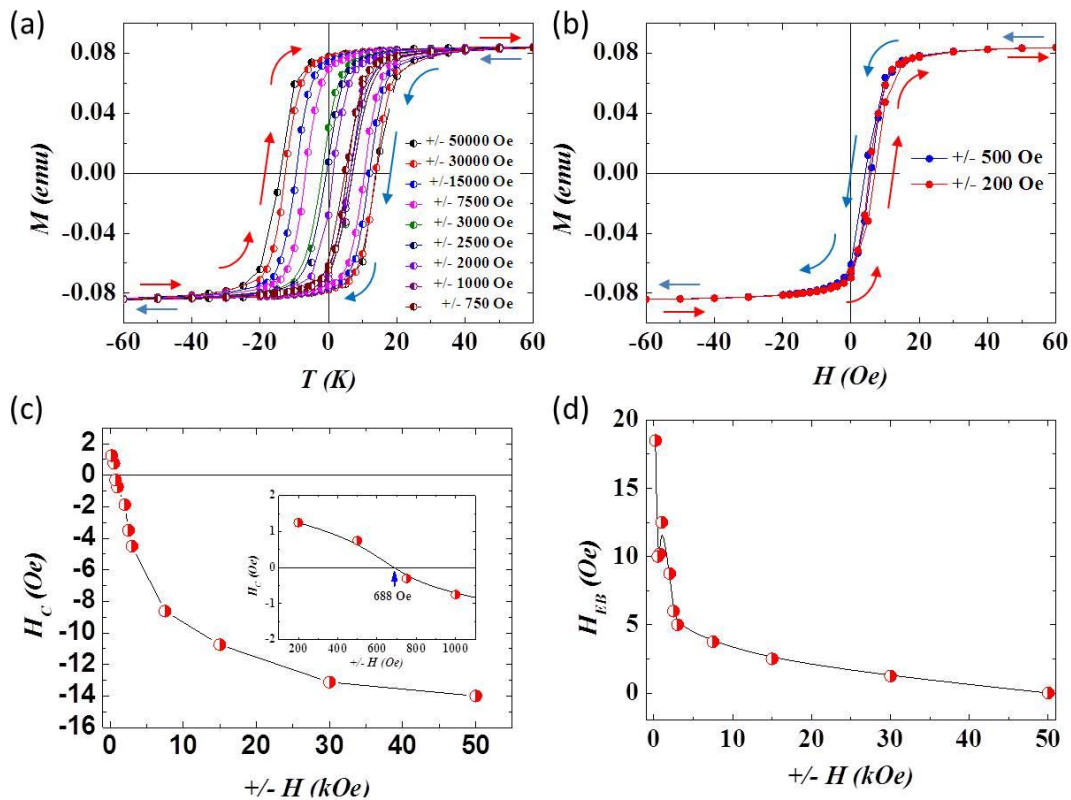
Fig.7.6. Clockwise (a) and counter-clockwise (b) hysteresis loop formation. The switching from counter-clockwise and clockwise ative hysteresis loop is at 688 Oe. (c) The amount of exchange bias decreases with increase of field range and reaches zero at 50 kOe

negative starting field (Fig. 7.7c). No step in hysteresis loop measurements was found (Fig.7.7 b). The ascending and descending branches of inverse hysteresis loop measured at 5K coincide with exchange bias loop shift (counter-clockwisee loops) in positive and negative direction measured at 5K (Fig.7.7 c). The *dM/dH* curve shows half magnitude of negative hysteresis compared to counter-clockwise hysteresis.
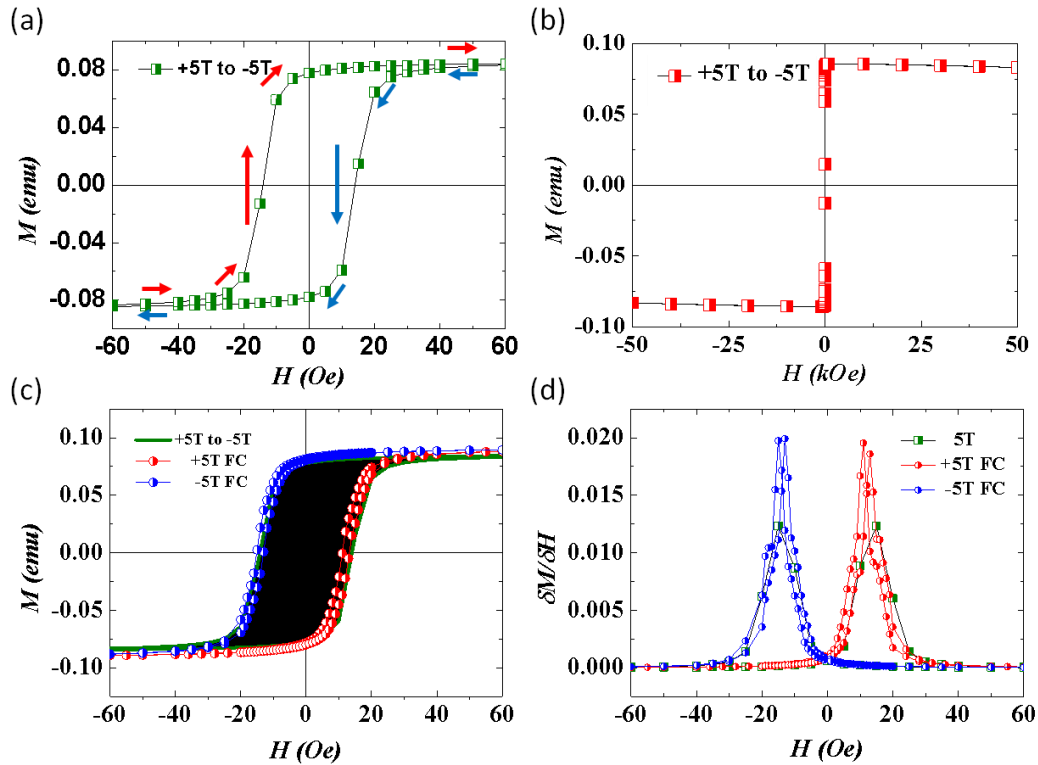
Fig.7.7. (a) Inverse hysteresis loop observation at 2K temperature. (b) No step has not been observed throughout 50 kOe loop range. (c) The hysteresis loop observed at 2 K with 50 kOe coincides with low field (200 Oe) measurements. (d) δM/δH has been plotted for both positive and negative hysteresis loops

7.5.   Result and Discussion

The hysteresis loop shift after the sample was cooled down under a bias field of positive (negative) 1000 Oe was in positive (negative) direction. Thus the type of exchange bias is positive. The amount of exchange bias is 5 Oe at room temperature and it increases at 2k up to 23 Oe. The coercivity of the sample is ~2 Oe. The saturation magnetization field was ~50 Oe. 100 Oe was the lowest starting field used for hysteresis loop tracing to ensure the saturation of the sample. Later the starting field was gradually increased and it was found that the amount of coercivity was decreased monotonously and path of hysteresis loop became reversed after ~700 Oe field. The amount of exchange bias was also gradually decreased and became zero at 50 kOe starting field measurement. In order to qualitative interpret the counter-clockwise to clockwise hysteresis loop in the NiFe thin film we did detail HRTEM analysis. Exchange bias phenomenon depends on the interface coupling

between two different phases. The crystallographic relation between FM and AF phases are identified in the film by structures mapped onto HRTEM image pattern. From precise subnanoscale characterization and correlating these crystallographic structures with known magnetic structures by neutron diffraction of similar material [152] as shown in Fig. 7.4 its clear that in the matrix of ferromagnetic $Ni_{50}Fe_{50}$ there is tiny particles of Ni,Fe solid solution which antiferromagnetic (AFM) in nature. It was observed that the amount of exchange shift (H_E) is much greater than the coercivity (H_C) of the sample. From the detail microstructural analysis with nanoscale resolution we ascertain that the Ni,Fe solid solution is an admixture of AFM and FM phases and the interface to the $Ni_{50}Fe_{50}$ is effectively provides a local exchange coupling which permits a positive exchange bias. This exchange coupling at the interface can be developed and broken with large applied field. When a positive high field (+50 kOe) is applied positive exchange coupling is generated at the interface of the antiferromagnetic Ni_3Fe and ferromagnetic $Ni_{50}Fe_{50}$. Hence first half of hysteresis loop (descending branch) is generated in the positive quadrant and a high negative field (-50 kOe) is applied at the end. This negative high field (-50 kOe) breaks the exchange coupling and generates negative exchange bias coupling at the interface. While measuring the second half of the hysteresis loop (ascending brunch) the curve follows exchange shift loop path in negative field direction. Hence an inverse hysteresis loop is generated. Negative coercivity has been earlier found in many multilayer thin film systems due to helical or step like hysteresis loop formation. The sum of the magnitudes of exchange shift in both directions ($|+H_{EB}|+|-H_{EB}|$) measured at 2K is equal to the coercivity (H_C) of the inverse hysteresis loop. The loop tracing range was gradually increased from $\pm$ 200 Oe to $\pm$ 50 kOe. The amount of exchange bias decreases and coercivity increases. Due to the increase of gradual loop tracing field the exchange coupling generated at the interface by bias field is broken by opposite high field in reverse direction. Hence the amount of exchange bias and coercivity are decreased. After certain field the loop switches to other direction and coercivity starts increasing. The Lowest exchange bias (0 Oe) and highest coercivity is obtained with the loop tracing range of $\pm$50 kOe.

7.6. Summary

In summary, we report that counter-clockwise and clockwise hysteresis loop formation with very low coercivity and large positive exchange bias is observed in the Ni,Fe solid solution. These two opposite (counter-clockwise to clockwise) hysteresis loop formation depends upon the field range of hysteresis loop measurement. $Ni_{50}Fe_{50}$ thin film shows positive exchange bias when the loop tracing field range is small (just above the saturation field) and the loop is positive. If the film is measured with a higher range of loop tracing field, a typical negative hysteresis loop with no exchange bias is observed. The origin of this interesting phenomenon of dual type of hysteresis loop (positive and negative) observation due to different range of field hysteresis loop measurement protocol depends on the microstructure of $Ni_{50}Fe_{50}$. Admixture of antiferromagnetic NiFe and ferromagnetic $Ni_{50}Fe_{50}$ acts like typical FM-AFM interface and permits positive exchange bias with very low coersivity. This AFM coupling at interface can be overcome with the application of a large field and AFM spins can be aligned like FM spin which leads to the formation of negative hysteresis loop. Thus the AFM-FM system behaves like FM at high field where all spins are aligned in the field direction.

8. Chapter - Conclusions

In this work we have investigated different nanostructured magnetic materials which have potential device applications. The main focus of the research was to investigate possibilities of controlling and enhancing magnetic anisotropy by different nanostructures. We have investigated the properties of samples through magnetic measurements and micromagnetic simulation, playing particular attention to the shape and exchange anisotropy where a particular type of nanostructure has huge influence on the hysteresis loop and magnetic microstructure. A detail literature review was carried out to delineate the recent development in the field. Various nanostructures such as lines, dots, anti-dots, etc. were reported to control the anisotropy.

A new model to achieve controllable magnetic anisotropy through the formation of magnetic dipoles in continuous ferromagnetic thin films due to a unique nanomodulation has been discussed in the thesis. Experimental evidence of well-ordered dipoles with metastable state has been detected by means of variation of magnetic anisotropy, step hysteresis, and MFM imaging. The anisotropy model, based on collective dipolar interaction, is used to demonstrate the ability to control anisotropy in continuous ferromagnetic thin films by minimizing magnetostatic energy through nanomodulation. The generalized model helps us to find out possible anisotropy based on material property and geometrical arrangement of nanopattern. Additionally, the formation of a metastable single domain resists vortex formation in nanopatterned ferromagnetic thin films, which are essential for realizing devices, such as volatile memory, magnetically frustrated patterned media, highly integrated nanoscale magnetic devices, etc.

If the patterned frequency is comparable to the frequency of magnetic wave then one can assume the effect of pattern on the propagation of magnetic wave. The frequency of any wave is inversely proportional to the wavelength.

$$\omega = 2\pi f = \frac{C}{\lambda}$$

The frequency of a wave in free space can be written as

$$f = \frac{\sqrt{\varepsilon_0 \mu_0}}{\lambda}$$

But for a magnetic material this is written as

$$f = \frac{\sqrt{\varepsilon\ \mu}}{\lambda}$$
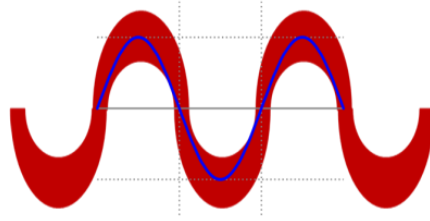
Fig.8.1: EM wave inside pattered media

If the pattern has a wave-like structure at certain dimensions one can calculate a resonance frequency for a particular material. This can be defined as

$$f_r = \frac{\sqrt{\varepsilon_r\mu_r}}{\lambda}$$

Where f_r is the resonance frequency, ε_r and μ_r are respective permittivity and permeability at the resonance frequency. The frequency of the wave in the magnetic material can be expressed in another way as

$$\omega_r = 2\pi\frac{\sqrt{\varepsilon_r\mu_r}}{\lambda_r} = \frac{\vartheta(t,M)}{\lambda_r}$$

Here v (t,M) is the velocity of the wave inside the material. The velocity of EM wave depends upon the material and thickness in nano scale. We would like to investigate the effect of the structure and anisotropy of the patterned magnetic media on the propagation of the EM wave inside the material.

Exchange anisotropy or exchange bias is a complex phenomenon which has not been well understood yet after 60 years of its invention. In the present work the exchange bias at the interface of composite $BiFeO_3$-$Bi_2Fe_4O_9$ nanostructures has been investigated. The exchange bias effect is quite remarkable here for several reasons. Due to exchange coupling ordinary ferromagnetic meterials have not one but two equally favoured stable magnetic

directions. These directions are collinear and lie along the easy magtization directions so-called "easy axis". Due to asymmetric exchange coupling two stable magnetization directions have slightly different energy. Hence different magnitude of an external field is required to rotate the magnetization by 180° from one easy direction to the other. Hence the magnetization loop is therefore asymmetric about zero field. However, in second approach in NiFe the ferromagnetic hysteresis loop is symmetric, indicating two equivalent easy directions. On the other hand, due to exchange coupling between NiFe solid solution and $Ni_{50}Fe_{50}$ the coercivity is less compared to conventional AFM-FM system. The exchange bias in such case is switchable via field.

Historically, the main problem in establishing a realistic model of exchange bias lies in the lack of information on the spin structure near the interface and the difficulty of experimentally determining the magnetic structure at the interface. Hence the proper explanation of exchange bias remains unsolved for nearly 60 years. While even in our observation new aspects of this phenomenon FM-DAFF-SSG-AMF based exchange bias and asymmetric exchange bias in BFO nano-composite or positive-negative hysteresis loop formation are still not well understood. Over the last few years x-ray dichroism spectroscopy and microscopy measurements have made key contributions to the solution of this long-standing problem where direct information on the magnetic structure at the interface are invested. Further the interfacial spin structure and the FM-AFM link at interface can be investigated in our systems and a realistic model of exchange bias can be proposed. The microstructure of electrodeposited $Ni_{50}Fe_{50}$ thin film needs to be investigated to understand the formation of inverted hysteresis loop in such systems. It is envisaged that EELS analysis at atomic resolution will help to understand atomic level interaction. Furthermore, the optimization of magnetic parameters such as pattern geometry, film thickness, interfacial exchange coupling is required to obtain controllable exchange bias in a thin film. In those films the magnetization of the ferromagnetic layer is locally pinned differently at the interface by the antiferromagnetic layer implying that the complete film will adopt the resultant lateral varying magnetization. Thus an optimized nanostructure and material choice is essential to manipulate overall magnetic properties of the films which can be further investigated (Fig. 8.2). The patterned thin film can show a unique range of magnetic properties, particularly in the GHz frequency range used in RF

communications. If the patterned frequency is comparable to the frequency of magnetic wave then one can assume the effect of pattern on the propagation of magnetic wave.

NiFe Composite film

NiFe Composite patterned film

Multilayer film

Multilayer patterned film

Ni$_3$Fe   Ni$_{80}$Fe$_{20}$ PMMA

Ni$_{45}$Fe$_{55}$ Si Substrate
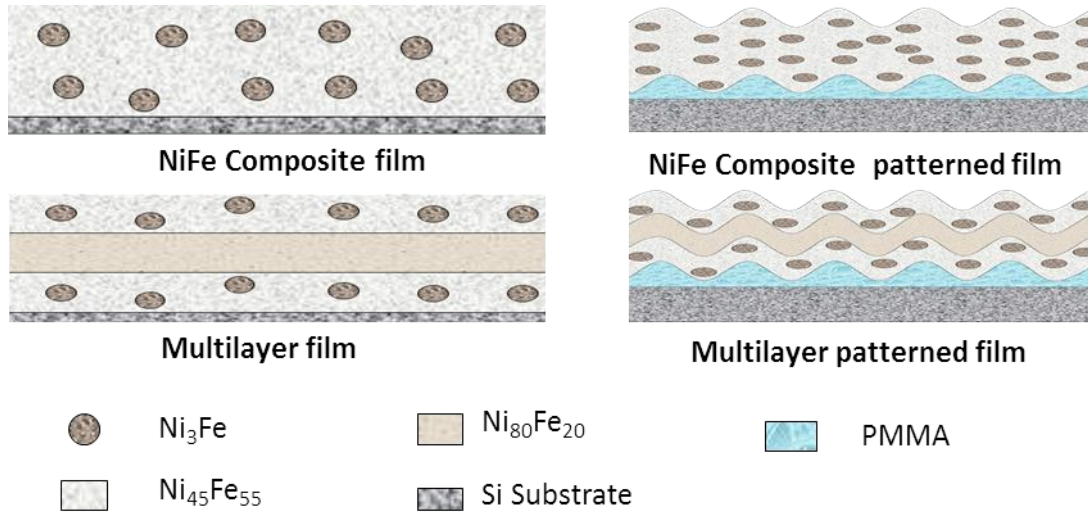
Fig.8.2. Single and multilayer nanomodulated film

The impact of this work will be reflected on size reduction of magnetic components with better performance for miniaturized ICT devices and development of cost effective process. We have chosen modulated PR electrodeposition/ dc-rf-sputtering combined with nanoimprint lithography, a novel approach, for sample preparation. We believe that the work will result in novel nanomodulaed/multilater thin film of composite material, which would delineate novel physical insights in the new magnetic 'multi- nano- layer-structures' with a technological impact in ICT industry. The principal significance of this work will stem from the cost effective and compatible manufacturing process for the next generation high frequency micromagnetic devices for various applications e.g. telecommunication industry, storage media, magnetic component based electronics, etc.

Appendix

A. Micromagnetic Input Format File (MIF)

This MIF file was used to simulate the nanopatterned structure to understand the anisotropy variation.

MIF 2.1
Description: This MIF file was updated by Tuhin Miaty on 08/04/20011.
#
This file will simulate a 3D patterned surface.

```
set pi [expr 4*atan(1.0)]
set mu0 [expr 4*$pi*1e-7]


Specify Oxs_MultiAtlas:atlas {

        atlas { Oxs_ImageAtlas {
        xrange {0 8000e-9}
        yrange {0 8000e-9}
        zrange {0 100e-9}
        viewplane "xy"
        image R0.bmp
        colormap {
        white nonmagnetic
        black magnetic
        }
        matcherror .1
        }
        }

        atlas { Oxs_ImageAtlas {
        xrange {0 8000e-9}
        yrange {0 8000e-9}
        zrange {100e-9 200e-9}
        viewplane "xy"
        image R0I.bmp
        colormap {
        white nonmagnetic
        black magnetic
        }
        matcherror .1
```

```
            }
            }

            }
```

```
Specify Oxs_RectangularMesh:mesh {
cellsize {50e-9 50e-9 50e-9}
atlas :atlas
}
```

#The anisotropy energy is the energy stored in a ferromagnetic crystal by virtue of the work done in rotating the magnetisation away from the direction of the
#easy axis. The specify block takes two parameters, the crystalline anisotropy constant K1 (J/m^3) and the anisotropy direction axis.
#the calculated value of K1 is 600.

```
Specify Oxs_UniaxialAnisotropy {
        K1 600
        axis { Oxs_UniformVectorField {
norm 1
comment {this direction uses the standard x,y,z coordinate system}
vector {1 0 0}
} }   }
```

#Specifies the exchange coupling constant in J/m.
#A is the exchange constant.
#A is also known as the exchange stiffness.

```
Specify Oxs_UniformExchange:NiFe {A  6.47e-12}
```

The Zeeman energy is the interaction between an atomic or molecular magnetic moment and an applied magnetic field.
this multiplier is optional, the fields specified in the range entry are normally in A/m, but these values are multiplied by a multiplier
this effectively changes their units, the number 795.77472 converts from milliTesla to A/m.

#{the 7th term give the number of steps, so one means go from the first field to the last field with no fields in between}
```
Specify Oxs_UZeeman {
multiplier 795.77472
```

Hrange {

    {0 0 0 400 0 0 10}

}
}

this is a standard specify term which is put into every mif file. It is built on the assumption that the demagnetisation field is constant in each cell and computers the average
demagnetisation field through the cell.
Specify Oxs_Demag {}

Minimisation evolver.

Specify Oxs_CGEvolve {}

Specify Oxs_MinDriver {

evolver Oxs_CGEvolve

mesh :mesh

comment {this value is in A/m, the oommf manual says that it is usually not possible to obtain a value of mxHxm below about 0.01}
 stopping_mxHxm 1

Ms {
        Oxs_AtlasScalarField {
        atlas :atlas
        default_value 0
        values {
        nonmagnetic 0
        magnetic 1.2e6

    }
}}

comment {mo gives the initial configuration of the magnetisation unit spins}
 m0 {0.017452406437283376 0.99984769515639127 0.0}

}
This MIF file was used to simulate MH curve for the nanopatterned structure

MIF 2.1
Description: This MIF file was updated by Tuhin Miaty on 26/03/20011.
#
This file will simulate a 3D patterned surface.

set pi [expr 4*atan(1.0)]
set mu0 [expr 4*$pi*1e-7]

Specify Oxs_MultiAtlas:atlas {

        atlas { Oxs_ImageAtlas {
        xrange {0 4000e-9}
        yrange {0 4000e-9}
        zrange {0 400e-9}
        viewplane "xy"
        image Circula_SquarePattern_DistanceRatio1_Rotation00.bmp
        colormap {
        white magnetic
        black magnetic
        }
        matcherror .1
        }
        }

        atlas { Oxs_ImageAtlas {
        xrange {0 4000e-9}
        yrange {0 4000e-9}
        zrange {400e-9 800e-9}
        viewplane "xy"
        image Circula_SquarePattern_DistanceRatio1_Rotation00_Inverse.bmp
        colormap {
        white magnetic
        black magnetic
        }
        matcherror .1
        }
        }

        }

#A mesh size of 50 nm will give 30000 cells
Specify Oxs_RectangularMesh:mesh {
cellsize {50e-9 50e-9 50e-9}
atlas :atlas
}

#The anisotropy energy is the energy stored in a ferromagnetic crystal by virtue of the
work done in rotating the magnetisation away from the direction of the
#easy axis. The specify block takes two parameters, the crystalline anisotropy constant
K1 (J/m^3) and the anisotropy direction axis.
#the calculated value of K1 is 600.

Specify Oxs_UniaxialAnisotropy {
        K1 600
        axis { Oxs_UniformVectorField {
norm 1
comment {this direction uses the standard x,y,z coordinate system}
vector {1 0 0}
} }   }

#Specifies the exchange coupling constant in J/m.
#A is the exchange constant.
#A is also known as the exchange stiffness.

Specify Oxs_UniformExchange:NiFe {A 6.47e-12}

The Zeeman energy is the interaction between an atomic or molecular magnetic
moment and an applied magnetic field.
this multiplier is optional, the fields specified in the range entry are normally in A/m,
but these values are multiplied by a multiplier
this effectively changes their units, the number 795.77472 converts from milliTesla to
A/m.

#{the 7th term give the number of steps, so one means go from the first field to the last
field with no fields in between}
Specify Oxs_UZeeman {
multiplier 795.77472
  Hrange {

    {1000 0 0 0 0 0 100}
    {0 0 0 -1000 0 0 100}
    {-1000 0 0 0 0 0 100}

{0 0 0 1000 0 0 100}

}
}

demagnetisation field through the cell.
Specify Oxs_Demag {}

Minimisation evolver.

Specify Oxs_CGEvolve {}

Specify Oxs_MinDriver {

evolver Oxs_CGEvolve

mesh :mesh

comment {this value is in A/m, the oommf manual says that it is usually not possible to obtain a value of mxHxm below about 0.01}
 stopping_mxHxm 1

Ms {
        Oxs_AtlasScalarField {
        atlas :atlas
        default_value 0
        values {
        magnetic 1.2e6

    }
 }}

comment {mo gives the initial configuration of the magnetisation unit spins}
 m0 {0.017452406437283376 0.99984769515639127 0.0}

}

B. Example of sequence file used for SQUID magnetic measurement

MT & MH measurement

Set Cal Factor: Temp: Tolerance 0.050
Set Temperature 350.000K at 10.000K/min.
Waitfor Temp:Stable Delay:1secs
Run Sequence: C:\SQUID_DATA\Tuhin\Sequence\Tyndall\Ashish\Demag.seq
Set Magnetic Field 50000.00 Oe, Oscillate, Hi Res Enabled
Waitfor Field:Stable Delay:1secs
Set Temperature 2.000K at 10.000K/min.
Set Datafile: [**INVALID PATH**]
C:\SQUID_DATA\Tuhin\Data\CGCRI\BFO_B\2013_New\BFO_B_Positive_5T_MH_2
K_20130206
Run Sequence:
C:\SQUID_DATA\Tuhin\Sequence\Tyndall\CGCRI\BFO\MH_5T_Positive.seq
Set Magnetic Field 0.00 Oe, No Overshoot, Hi Res Enabled
Waitfor Field:Stable Delay:1secs
Set Temperature 350.000K at 10.000K/min.
Waitfor Temp:Stable Delay:1secs
Run Sequence: C:\SQUID_DATA\Tuhin\Sequence\Tyndall\Demag.seq
Set Magnetic Field -50000.00 Oe, Oscillate, Hi Res Enabled
Waitfor Field:Stable Delay:1secs
Set Temperature 2.000K at 10.000K/min.
Set Datafile: [**INVALID PATH**]
C:\SQUID_DATA\Tuhin\Data\CGCRI\BFO_B\2013_New\BFO_B_Negaitive_5T_MH_
2K_20130206
Run Sequence:
C:\SQUID_DATA\Tuhin\Sequence\Tyndall\CGCRI\BFO\MH_5T_Positive.seq
Set Magnetic Field 0.00 Oe, Oscillate, Hi Res Enabled
Waitfor Field:Stable Delay:1secs

ZFC Sequence
Scan Temp from 2.000K to 99.00K at 1.000K/min in 1K increments (98 steps) Sweep
   Measure DC: 4.00 cm, 28 pts, 2 scans, AutoRng, Long, Iterative Reg., track:No,
raw:Yes, diag:Yes
End Scan
Scan Temp from 100.0K to 350.0K at 2.500K/min in 2.5K increments (101 steps) Sweep
   Measure DC: 4.00 cm, 28 pts, 2 scans, AutoRng, Long, Iterative Reg., track:No,
raw:Yes, diag:Yes
End Scan

AC ZFC sequence

Scan Temp from 5.000K to 350.0K at 2.500K/min in 2.5K increments (139 steps) Sweep
   Measure AC: 2.0000 Oe, 99.947 Hz, 2 meas, 2 blks, 1E-005 Null, x 1, 1 s, AutoRng,
track:No, diag:Yes, raw:Yes
End Scan

FC Sequence

Scan Temp from 350.0K to 100.0K at 2.500K/min in -2.5K increments (101 steps) Sweep
   Measure DC: 4.00 cm, 28 pts, 2 scans, AutoRng, Long, Iterative Reg., track:No,
raw:Yes, diag:Yes
End Scan
Scan Temp from 99.00K to 2.000K at 1.000K/min in -1K increments (98 steps) Sweep
   Measure DC: 4.00 cm, 28 pts, 2 scans, AutoRng, Long, Iterative Reg., track:No,
raw:Yes, diag:Yes
End Scan

AC FC sequence

Scan Temp from 350.000K to 5.0K at 2.500K/min in 2.5K increments (139 steps) Sweep
   Measure AC: 2.0000 Oe, 99.947 Hz, 2 meas, 2 blks, 1E-005 Null, x 1, 1 s, AutoRng,
track:No, diag:Yes, raw:Yes
End Scan

Positive MH curve Sequence

Scan Field from 50000.00Oe to 10000.00 Oe in -20000.00 Oe increments (3 steps), No
Overshoot, Hi Res Enabled
   Measure DC: 4.00 cm, 28 pts, 2 scans, AutoRng, Long, Iterative Reg., track:No,
raw:Yes, diag:Yes
End Scan
Scan Field from 8000.00Oe to -2000.00 Oe in -2000.00 Oe increments (6 steps), No
Overshoot, Hi Res Enabled
   Measure DC: 4.00 cm, 28 pts, 2 scans, AutoRng, Long, Iterative Reg., track:No,
raw:Yes, diag:Yes
End Scan
Scan Field from -2500.00Oe to -5000.00 Oe in -500.00 Oe increments (6 steps), No
Overshoot, Hi Res Enabled
   Measure DC: 4.00 cm, 28 pts, 3 scans, AutoRng, Long, Iterative Reg., track:No,
raw:Yes, diag:Yes
End Scan
Scan Field from -6000.00Oe to -8000.00 Oe in -2000.00 Oe increments (2 steps), No
Overshoot, Hi Res Enabled
   Measure DC: 4.00 cm, 28 pts, 2 scans, AutoRng, Long, Iterative Reg., track:No,
raw:Yes, diag:Yes
End Scan

Scan Field from -10000.00Oe to -50000.00 Oe in -20000.00 Oe increments (3 steps), No Overshoot, Hi Res Enabled
    Measure DC: 4.00 cm, 28 pts, 2 scans, AutoRng, Long, Iterative Reg., track:No, raw:Yes, diag:Yes
End Scan
Scan Field from -30000.00Oe to -10000.00 Oe in 20000.00 Oe increments (2 steps), No Overshoot, Hi Res Enabled
    Measure DC: 4.00 cm, 28 pts, 2 scans, AutoRng, Long, Iterative Reg., track:No, raw:Yes, diag:Yes
End Scan
Scan Field from -8000.00Oe to -4000.00 Oe in 2000.00 Oe increments (3 steps), No Overshoot, Hi Res Enabled
    Measure DC: 4.00 cm, 28 pts, 2 scans, AutoRng, Long, Iterative Reg., track:No, raw:Yes, diag:Yes
End Scan
Scan Field from -3000.00Oe to 2000.00 Oe in 500.00 Oe increments (11 steps), No Overshoot, Hi Res Enabled
    Measure DC: 4.00 cm, 28 pts, 2 scans, AutoRng, Long, Iterative Reg., track:No, raw:Yes, diag:Yes
End Scan
Scan Field from 3000.00Oe to 9000.00 Oe in 2000.00 Oe increments (4 steps), No Overshoot, Hi Res Enabled
    Measure DC: 4.00 cm, 28 pts, 2 scans, AutoRng, Long, Iterative Reg., track:No, raw:Yes, diag:Yes
End Scan
Scan Field from 10000.00Oe to 50000.00 Oe in 20000.00 Oe increments (3 steps), No Overshoot, Hi Res Enabled
    Measure DC: 4.00 cm, 28 pts, 2 scans, AutoRng, Long, Iterative Reg., track:No, raw:Yes, diag:Yes
End Scan

Negative MH curve sequence

Scan Field from -50000.00Oe to -10000.00 Oe in 20000.00 Oe increments (3 steps), No Overshoot, Hi Res Enabled
    Measure DC: 4.00 cm, 28 pts, 2 scans, AutoRng, Long, Iterative Reg., track:No, raw:Yes, diag:Yes
End Scan
Scan Field from -8000.00Oe to -2000.00 Oe in 2000.00 Oe increments (4 steps), No Overshoot, Hi Res Enabled
    Measure DC: 4.00 cm, 28 pts, 2 scans, AutoRng, Long, Iterative Reg., track:No, raw:Yes, diag:Yes
End Scan
Scan Field from -1000.00Oe to 1000.00 Oe in 500.00 Oe increments (5 steps), No Overshoot, Hi Res Enabled

Measure DC: 4.00 cm, 28 pts, 2 scans, AutoRng, Long, Iterative Reg., track:No, raw:Yes, diag:Yes
End Scan
Scan Field from 1500.00Oe to 5500.00 Oe in 500.00 Oe increments (9 steps), No Overshoot, Hi Res Enabled
Measure DC: 4.00 cm, 28 pts, 2 scans, AutoRng, Long, Iterative Reg., track:No, raw:Yes, diag:Yes
End Scan
Scan Field from 6000.00Oe to 8000.00 Oe in 2000.00 Oe increments (2 steps), No Overshoot, Hi Res Enabled
Measure DC: 4.00 cm, 28 pts, 2 scans, AutoRng, Long, Iterative Reg., track:No, raw:Yes, diag:Yes
End Scan
Scan Field from 10000.00Oe to 50000.00 Oe in 20000.00 Oe increments (3 steps), No Overshoot, Hi Res Enabled
Measure DC: 4.00 cm, 28 pts, 2 scans, AutoRng, Long, Iterative Reg., track:No, raw:Yes, diag:Yes
End Scan
Scan Field from 30000.00Oe to 10000.00 Oe in -20000.00 Oe increments (2 steps), No Overshoot, Hi Res Enabled
Measure DC: 4.00 cm, 28 pts, 2 scans, AutoRng, Long, Iterative Reg., track:No, raw:Yes, diag:Yes
End Scan
Scan Field from 8000.00Oe to 4000.00 Oe in -2000.00 Oe increments (3 steps), No Overshoot, Hi Res Enabled
Measure DC: 4.00 cm, 28 pts, 2 scans, AutoRng, Long, Iterative Reg., track:No, raw:Yes, diag:Yes
End Scan
Scan Field from 3000.00Oe to -1000.00 Oe in -500.00 Oe increments (9 steps), No Overshoot, Hi Res Enabled
Measure DC: 4.00 cm, 28 pts, 2 scans, AutoRng, Long, Iterative Reg., track:No, raw:Yes, diag:Yes
End Scan
Scan Field from -1500.00Oe to -4000.00 Oe in -500.00 Oe increments (6 steps), No Overshoot, Hi Res Enabled
Measure DC: 4.00 cm, 28 pts, 2 scans, AutoRng, Long, Iterative Reg., track:No, raw:Yes, diag:Yes
End Scan
Scan Field from -5000.00Oe to -9000.00 Oe in -2000.00 Oe increments (3 steps), No Overshoot, Hi Res Enabled
Measure DC: 4.00 cm, 28 pts, 2 scans, AutoRng, Long, Iterative Reg., track:No, raw:Yes, diag:Yes
End Scan
Scan Field from -10000.00Oe to -50000.00 Oe in -20000.00 Oe increments (3 steps), No Overshoot, Hi Res Enabled

Measure DC: 4.00 cm, 28 pts, 2 scans, AutoRng, Long, Iterative Reg., track:No, raw:Yes, diag:Yes
End Scan

IRM & TRM sequence

Set Cal Factor: Temp: Tolerance 0.050
Set Temperature 300.000K at 10.000K/min.
Waitfor Temp:Stable Delay:60secs
Run Sequence: C:\SQUID_DATA\Tuhin\Sequence\Tyndall\FeO\Demag.seq
Set Datafile: [**INVALID PATH**]
C:\SQUID_DATA\Tuhin\Data\CGCRI\BFO_A\BFO_A_IRM
Set Temperature 5.000K at 10.000K/min.
Waitfor Temp:Stable Delay:60secs
Set Magnetic Field 50.00 Oe, No Overshoot, Hi Res Enabled
Waitfor Field:Stable Delay:60secs
Set Magnetic Field 0.00 Oe, No Overshoot, Hi Res Enabled
Waitfor Field:Stable Delay:60secs
Measure DC: 4.00 cm, 28 pts, 2 scans, AutoRng, Long, Iterative Reg., track:No, raw:Yes, diag:Yes
Set Magnetic Field 10000.00 Oe, No Overshoot, Hi Res Enabled
Waitfor Field:Stable Delay:60secs
Set Magnetic Field 0.00 Oe, No Overshoot, Hi Res Enabled
Waitfor Field:Stable Delay:60secs
Measure DC: 4.00 cm, 28 pts, 2 scans, AutoRng, Long, Iterative Reg., track:No, raw:Yes, diag:Yes
Set Magnetic Field 20000.00 Oe, No Overshoot, Hi Res Enabled
Waitfor Field:Stable Delay:60secs
Set Magnetic Field 0.00 Oe, No Overshoot, Hi Res Enabled
Waitfor Field:Stable Delay:60secs
Measure DC: 4.00 cm, 28 pts, 2 scans, AutoRng, Long, Iterative Reg., track:No, raw:Yes, diag:Yes
Set Magnetic Field 30000.00 Oe, No Overshoot, Hi Res Enabled
Waitfor Field:Stable Delay:60secs
Set Magnetic Field 0.00 Oe, No Overshoot, Hi Res Enabled
Waitfor Field:Stable Delay:60secs
Measure DC: 4.00 cm, 28 pts, 2 scans, AutoRng, Long, Iterative Reg., track:No, raw:Yes, diag:Yes
Set Magnetic Field 40000.00 Oe, No Overshoot, Hi Res Enabled
Waitfor Field:Stable Delay:60secs
Set Magnetic Field 0.00 Oe, No Overshoot, Hi Res Enabled
Waitfor Field:Stable Delay:60secs
Measure DC: 4.00 cm, 28 pts, 2 scans, AutoRng, Long, Iterative Reg., track:No, raw:Yes, diag:Yes
Set Magnetic Field 50000.00 Oe, No Overshoot, Hi Res Enabled
Waitfor Field:Stable Delay:60secs

Set Magnetic Field 0.00 Oe, No Overshoot, Hi Res Enabled
Waitfor Field:Stable Delay:60secs
Measure DC: 4.00 cm, 28 pts, 2 scans, AutoRng, Long, Iterative Reg., track:No, raw:Yes, diag:Yes
Set Temperature 300.000K at 10.000K/min.
Waitfor Temp:Stable Delay:60secs
Run Sequence: C:\SQUID_DATA\Tuhin\Sequence\Tyndall\FeO\Demag.seq
Set Datafile: [**INVALID PATH**]
C:\SQUID_DATA\Tuhin\Data\CGCRI\BFO_A\BFO_A_TRM
Set Magnetic Field 50000.00 Oe, No Overshoot, Hi Res Enabled
Waitfor Field:Stable Delay:60secs
Set Temperature 5.000K at 10.000K/min.
Waitfor Temp:Stable Delay:60secs
Set Magnetic Field 0.00 Oe, No Overshoot, Hi Res Enabled
Waitfor Field:Stable Delay:60secs
Measure DC: 4.00 cm, 28 pts, 2 scans, AutoRng, Long, Iterative Reg., track:No, raw:Yes, diag:Yes
Set Temperature 300.000K at 10.000K/min.
Waitfor Temp:Stable Delay:60secs
Run Sequence: C:\SQUID_DATA\Tuhin\Sequence\Tyndall\FeO\Demag.seq
Set Magnetic Field 40000.00 Oe, No Overshoot, Hi Res Enabled
Waitfor Field:Stable Delay:60secs
Set Temperature 5.000K at 10.000K/min.
Waitfor Temp:Stable Delay:60secs
Set Magnetic Field 0.00 Oe, No Overshoot, Hi Res Enabled
Waitfor Field:Stable Delay:60secs
Measure DC: 4.00 cm, 28 pts, 2 scans, AutoRng, Long, Iterative Reg., track:No, raw:Yes, diag:Yes
Set Temperature 300.000K at 10.000K/min.
Waitfor Temp:Stable Delay:60secs
Run Sequence: C:\SQUID_DATA\Tuhin\Sequence\Tyndall\FeO\Demag.seq
Set Magnetic Field 30000.00 Oe, No Overshoot, Hi Res Enabled
Waitfor Field:Stable Delay:60secs
Set Temperature 5.000K at 10.000K/min.
Waitfor Temp:Stable Delay:60secs
Set Magnetic Field 0.00 Oe, No Overshoot, Hi Res Enabled
Waitfor Field:Stable Delay:60secs
Measure DC: 4.00 cm, 28 pts, 2 scans, AutoRng, Long, Iterative Reg., track:No, raw:Yes, diag:Yes
Set Temperature 300.000K at 10.000K/min.
Waitfor Temp:Stable Delay:60secs
Run Sequence: C:\SQUID_DATA\Tuhin\Sequence\Tyndall\FeO\Demag.seq
Set Magnetic Field 20000.00 Oe, No Overshoot, Hi Res Enabled
Waitfor Field:Stable Delay:60secs
Set Temperature 5.000K at 10.000K/min.
Waitfor Temp:Stable Delay:60secs

Set Magnetic Field 0.00 Oe, No Overshoot, Hi Res Enabled
Waitfor Field:Stable Delay:60secs
Measure DC: 4.00 cm, 28 pts, 2 scans, AutoRng, Long, Iterative Reg., track:No, raw:No, diag:Yes
Set Temperature 300.000K at 10.000K/min.
Waitfor Temp:Stable Delay:60secs
Run Sequence: C:\SQUID_DATA\Tuhin\Sequence\Tyndall\FeO\Demag.seq
Set Magnetic Field 10000.00 Oe, No Overshoot, Hi Res Enabled
Waitfor Field:Stable Delay:60secs
Set Temperature 5.000K at 10.000K/min.
Waitfor Temp:Stable Delay:60secs
Set Magnetic Field 0.00 Oe, No Overshoot, Hi Res Enabled
Waitfor Field:Stable Delay:60secs
Measure DC: 4.00 cm, 28 pts, 2 scans, AutoRng, Long, Iterative Reg., track:No, raw:Yes, diag:Yes
Set Temperature 300.000K at 10.000K/min.
Waitfor Temp:Stable Delay:60secs
Run Sequence: C:\SQUID_DATA\Tuhin\Sequence\Tyndall\FeO\Demag.seq
Set Magnetic Field 50.00 Oe, No Overshoot, Hi Res Enabled
Waitfor Field:Stable Delay:60secs
Set Temperature 5.000K at 10.000K/min.
Waitfor Temp:Stable Delay:60secs
Set Magnetic Field 0.00 Oe, No Overshoot, Hi Res Enabled
Waitfor Field:Stable Delay:60secs
Measure DC: 4.00 cm, 28 pts, 2 scans, AutoRng, Long, Iterative Reg., track:No, raw:Yes, diag:Yes
Set Temperature 2.000K at 10.000K/min.
Waitfor Temp:Stable Delay:60secs
Set Magnetic Field 0.00 Oe, No Overshoot, Hi Res Enabled
Waitfor Field:Stable Delay:60secs

Bibliography:

1.   Richard J. Harrison1 and Joshua M. Feinberg (ElEmEnts, Vol. 5, pp. 209–215, 2009)

2.   Introduction to the theory of Ferromagnetism. Oxford Science Publications, 2nd edition (2000)

3.   J. Briones, F. Montaigne, D. Lacour, G. Lengaigne, S. Girod, and M. Hehn, Appl. Phys. Express, **vol.3**, pp.073002, 2010.

4.   O'Handley RC.:Modern Magnetic Materials: Principles and Applications. John Wiley and Sons, Inc. (1999).

5.   S. P. Li, D. Peyrade, M. Natali, A. Lebib, Y. Chen, U. Ebels, L. D. Buda, and K. Ounadjela, Phys. Rev. Lett. **86**, 1102 (2001).

6.   R. P. Cowburn, D. K. Koltsov, A. O. Adeyeye, M. E. Welland, and D. M. Tricker, Phys. Rev. Lett. **83**, 1042 (1999).

7.   S. P. Li, Jeffrey F. Godsell, and Saibal Roy, Journal of Applied Physics **108**, 093915 (2010)

8.   C. Chappert, H. Bernas, J. Ferre, V. Kottler, J. P. Jamet, Y. Chen, E. Cambril, T. Devolder, F. Rousseaux, V. Mathet, and H. Launois, Science **280**, 1919 (1998)

9.   S. Tehrani, E. Chen, M. Durlam, M. DeHerrera, J. M. Slaughter, J. Shi, and G. Kerszykowski, J. Appl. Phys. **85**, 5822 (1999)

10.   F. Nguyen-Van-Dau, M. Sussiau, A. Schuhl, and P. Galtier, J. Appl. Phys.**81**, 4482 (1997).

11.   R. P. Cowburn, D. K. Koltsov, A. O. Adeyeye, and M. E. Welland, J. Appl. Phys. **87**, 7082 (2000).

12.   M. Hehn, K. Ounadjela, R. Ferre´, W. Gramge, and F. Rousseaux, Appl. Phys. Lett. **71**, 2833 (1997)

13.   D. J. Twisselmann, P. G. Chambers, C. A. Ross, G. Khanna, and B. M. Clemens, J. Appl. Phys. **92**, 3223 (2002)

14.   W. Oepts, M. A. M. Gijs, A. Reinders, R. M. Jungblut, R. M. J. vanGansewinkel, and W. J. M. deJonge, Phys. Rev. B **53**, 14024 (1996).

15.   G. Gubbiotti, S. Tacchi, G. Carlotti, P. Vavassori, N. Singh, S. Goolaup, A. O. Adeyeye, A. Stashkevich, and M. Kostylev. Phys. Rev. B **72**, 224413 (2005)

16. A. V. Goncharov, A. A. Zhukov1, V. V. Metlushko, G. Bordignon, H. Fangohr, G. Karapetrov, B. Ilic and P. A. J. de Groot; J. Appl. Phys. **99**, 08Q508 (2006)

17. R. F. Wang, C. Nisoli, R. S. Freitas, J. Li, W. McConville, B. J. Cooley, M. S. Lund, N. Samarth, C. Leighton, V. H. Crespi1 & P. Schiffer; Nature 439, 303-306 (2006)

18. W. Meiklejohn and C. P. Bean, Phys. Rev. **105**, 904 (1957).

19. M.N. Baibich, J.M. Broto, A. Fert, F. Nguyen Van Dau, F. Petroff, P. Etienne, G. Creuzet, A. Friederich, Phys. Rev. Lett. **61,**2472 (1988)

20. B. Dieny, J. Magn. Magn.Mater.**136**, 335 (1994).

20. Claude Chappert, Albert Fert and Frédéric Nguyen Van Dau; Nature Materials **6** (11) 813–823 (2007)

21. Nogu´es J, Sort J, Langlais V, Skumryev V, Suri˜nach S, Mu˜noz J S and Bar´o M D Phys. Rep. **422** 65 (2005)

22. For a recent review see, J. Nogués and Ivan K. Schuller, J. Magn. Magn.Mater.**192**, 203 (1999).

23. J. Nogue´s, D. Lederman, T. J. Moran, and I. K. Schuller, Phys. Rev. Lett. **76**, 4624 (1996)

24. J. Nogue´s, C. Leighton, and I. K. Schuller, Phys. Rev. B **61**, 1315 (2000)

25. J. Saha and R. H. Victora, Phys. Rev. B **76**, 100405(R) (2007)

26. D. Lebeugle, A. Mougin, M. Viret, D. Colson, and L. Ranno, Phys. Rev. Lett. **103**,257601 (2009).

27. L.W. Martin, Y.-H. Chu, Q. Zhan, R. Ramesh, S.-J. Han, S.X. Wang, M. Warusawithana, and D.G. Schlom, Appl. Phys. Lett. **91**, 172513 (2007).

28. L.W. Martin, Y.-H. Chu, M.B. Holcomb, M. Hujiben, P. Yu, S.-J. Han, D. Lee, S.X. Wang, and R. Ramesh, Nano Lett. **8**, 2050 (2008).

29. See, for example, D.B. Williams and C.B. Carter, Transmission Electron Microscopy, Part 2, Second Edition, (Springer, New York, 2009).

30. R. Mazumder, P.S. Devi, D. Bhattacharya, P. Choudhury, A. Sen, and M. Raja, Appl. Phys. Lett.**91**, 062510 (2007).

31. Z.M. Tian, S.L. Yuan, X.L. Wang, X.F. Zheng, S.Y. Yin, C.H. Wang, and L. Liu, J. Appl. Phys. **106**, 103912 (2009).

32.   J. Mallinson, Magneto-Resistive Heads - Fundamentals and Applications, Academic Press, New York (1996).

33.   Xu L, Jiang L P and Zhu J J; Nanotechnology 20 045605 (2009)

34.   Xu K, Mao C J, Geng J and Zhu J J, Nanotechnology 18 315604 (2007)

35.   S. Choi, S. Kawahito, Y. Matsumo, M. Ishida, and Y. Tadokoro; Sensors and Actuators A, vol. 55, pp. 121-126 (1996).

36.   B. Loechel and A. Maciossek, J. Electrochem.Soc., vo1.143, no. 10, pp. 3343-3348 (1996).

37.   W. O. Freitag and J. S. Mathias; J. Electochem. Soc., vol. 112, no. 1, pp. 64-67 (1965).

38.   Shinoura, "Electrodeposition of Ni-Fe-Mo Multilayered Soft Magnetic Films with High Specific Resistance," Denki Kagaku, vol. 63, no. 6, pp. 473-478 (1995).

39.   Schmid H 1994 Ferroelectrics 162 665

40.   Fiebig M 2005 J. Phys. D: Appl. Phys. 38 R123

41.   EerensteinW, Mathur N D and Scott J F 2006 Nature 442 759

42.   S. V. Kizelev, R. P. Ozerov, and G. S. Zhdanov, Sov. Phys. Dokl. 145,1255 (1962)

43.   Kubel F and Schmid H; Acta Crystallogr. B 46, 698 (1990)

44.   Kiselev S V, Ozerov R P and Zhdanov G S Sov. Phys.—Dokl. 7, 742 (1963)

45.   Teague J R, Gerson R and JamesW J Solid State Commun. 8, 1073 (1963)

46.   P Fischer, M Polomska, I Sosnowska and M Szymanski; J. Phys. C: Solid State Phys. 13, 1931 (1980)

47.   Sosnowska I, Peterlin-Neumaier T and Steichele E J. Phys. C: Solid State Phys. 15, 4835 (1982)

48.   Dzyaloshinskii I E, Sov. Phys.—JETP 5, 1259 (1957)

49.   Moriya T, Phys. Rev. 120 91 (1960)

50.   G Catalan and J.F. Scott, Advanced Materials, 21, 2463 (2009).

51.   H. Bea, M. Bibes, A. Barthelemy, K. Bouzehouane, E. Jacquet, A. Khodan, J. P. Contour, S. Fusil, F. Wyczisk, A. Forget, D. Lebeugle, D. Colson and M. Viret, Applied Physics Letters 87 (7),072508 (2005).

52. Review: H. Schmid, Cobalt 6 (1960) 8.

53. W.H. Meiklejohn, J. Appl. Phys. 29 (1958) 454.

54. M. Ohkoshi, K. Tamari, M. Harada, S. Honda, T. Kusuda, IEEE Transl. J. Magn. Japan 1 (1985) 37.

55. K. Hemmes, T.J.A. Popma, J. Phys. D 21 (1988) 228.

56. K. Tagaya, M. Fukada, J. Phys. Soc. Japan 46 (1979) 53.

57. R. Jungblut, R. Coehoorn, M.T. Johnson, J. aan de Stegge, A. Reinders, J. Appl. Phys. 75 (1994) 6659.

58. J. Nogue«s, D. Lederman, T.J. Moran, I.K. Schuller, K.V. Rao, Appl. Phys. Lett. 68 (1996) 3186.

59. Review Ð Applications Ð GMR: J.C.S. Kools, IEEE Trans. Magn. 32 (1996) 3165.

60. Review Ð Applications: C. Tang, J. Appl. Phys. 55 (1984)2226.

61. C. Tsang, N. Heiman, K. Lee, J. Appl. Phys. 52 (1981) 2471.

62. P.J. van der Zaag, R.M. Wolf, A.R. Ball, C. Bordel, L.F. Feiner, R. Jungblut, J. Magn. Magn.Mater.148 (1995) 346.

63. T. Tokunaga, M. Taguchi, T. Fukami, Y. Nakaki, K. Tsutsumi, J. Appl. Phys. 67 (1990) 4417.

64. W.C. Cain, M.H. Kryder, J. Appl. Phys. 67 (1990) 5722.

Reference Chapter 3

65. Shb Instruments, Inc.19215 Parthenia Street, Suite A, Northridge, CA 91324

66. Quantum Design, Inc., 6325 Lusk Boulevard , San Diego, CA 92121-3733, USA

67. Principles and Applications of Superconducting Quantum Interference Devices By Antonio Barone World Scientific, 1992

68. Asylum Research, 6310 Hollister Ave., Santa Barbara, CA 9311

69. JEOL USA, Inc.

70. Quanta SEM, FEI, Hillsboro, Oregon 97124 USA

71. PANalytical B.V., Spectris ompany

72. Vion Plasma Focused Ion Beam, FEI, Hillsboro, Oregon 97124 USA

73. Exchange interaction , Aharoni, 2000

74. Anisotropy energy, O'Handley, 1999

75. K. Seemann, H. Leiste, V. Bekker, Journal of Magnetism and Magnetic Materials, Volume 278, Issues 1–2 (2004)

76. Seberino, C., and H. N. Bertram, Concise, IEEE Trans. Magn., 37, 1078–1086, 2001

77. kronmüller and Fähnle, Cambridge University Press, Cambridge (2003)

78. Richard Boardman's PhD thesis, University of Southampton

79. M. Donahue and D. G. Porter, OOMMF User's Guide, Version1.0, Interagency Report NISTIR 6376 National Institute of Standard and Technology, Gaithersburg, MD, 1999; http://math.nist.gov/oommf

80. J. Briones, F. Montaigne, D. Lacour, G. Lengaigne, S. Girod, and M. Hehn; Appl. Phys. Express, vol.3, pp.073002, 2010.

81. R. Skomski, H.-P. Oepen, and J. Kirschner, Phys. Rev. B 58, 11138 (1998)

82. S.P. Li, Jeffrey F. Godsell and Saibal Roy; J Appl Phys 108, 093915, (2010)

83. S. P. Li, D. Peyrade, M. Natali, A. Lebib, Y. Chen, U. Ebels, L. D. Buda, and K. Ounadjela, Phys. Rev. Lett. 86, 1102 (2001).

84. R. P. Cowburn, D. K. Koltsov, A. O. Adeyeye, M. E. Welland, and D. M. Tricker, Phys. Rev. Lett. 83, 1042 (1999).

85. C. Chappert, H. Bernas, J. Ferre, V. Kottler, J. P. Jamet, Y. Chen, E. Cambril, T. Devolder, F. Rousseaux, V. Mathet, and H. Launois, Science 280, 1919 (1998)

86. S. Tehrani, E. Chen, M. Durlam, M. DeHerrera, J. M. Slaughter, J. Shi, and G. Kerszykowski, J. Appl. Phys. 85, 5822 (1999)

87. F. Nguyen-Van-Dau, M. Sussiau, A. Schuhl, and P. Galtier, J. Appl. Phys.81, 4482 (1997).

88. R. P. Cowburn, D. K. Koltsov, A. O. Adeyeye, and M. E. Welland, J. Appl. Phys. 87, 7082 (2000).

89. M. Hehn, K. Ounadjela, R. Ferre´, W. Gramge, and F. Rousseaux, Appl. Phys. Lett. 71, 2833 (1997)

90. Yeon Sik Jung, Wonjoon Jung and C. A. Ross; Nano Lett., 2008, 8 (9), pp 2975–2981

91. Elena Mengotti,Laura J. Heyderman, Arantxa Fraile Rodríguez, Frithjof Nolting,Remo V. Hügli, Hans-Benjamin Braun, Nature Physics 7, 68–74 (2011)

92. D. J. Twisselmann, P. G. Chambers, C. A. Ross, G. Khanna, and B. M. Clemens, J. Appl. Phys. 92, 3223 (2002)

93. W. Oepts, M. A. M. Gijs, A. Reinders, R. M. Jungblut, R. M. J. Van Gansewinkel, and W. J. M. deJonge, Phys. Rev. B 53, 14024 (1996).

94. S. Roy, A. Connell, M. Ludwig, N. Wang, T. O'Donnell, M. Brunet, P. McCloskey, C. ÓMathúna, A. Barman, and R.J. Hicken, Journal of Magn. Magn.Mater., vol.290-291. pp.1524-1527, 2005.

95. Y.-P. Zhao, R. M. Gamache, G.-C.Wang, T.-M.Lu, G. Palasantzas, and J.T. M. D. Hosson, J. Appl. Phys. 89, 1325 (2001).

96. Y. P. Zhao, G. Palasantzas, G. C. Wang, and J. T. M. De Hosson, Phys.Rev. B 60, 1216 (1999).

97. K. Y. Guslienko, V. Novosad, Y. Otani, H. Shima, and K. Fukamichi, Phys. Rev. B 65, 024414, 2001.

98. K. Y. Guslienko et al., Phys. Lett. A 278, 293 (2001)

99. Y. Yafet, E. M. Gyorgy, and L.R. Walker, J. Appl. Phy. 60, 4236 (1986)

100. Robert P. G. McNeil, Nano Lett., 2010, 10 (5), pp 1549–1553

101. Acta Phys. Pol. A 88 Supplement,S-69 (1995)

102. Watanabe, H.; Manabe, C.; Shigematsu, T.; Shimizu, M. Appl. Phys. Lett. 2001, 78 (19), 2928–2930.

103. Castano, F. J.; Morecroft, D.; Jung, W.; Ross, C. A. Phys. ReV. Lett. 2005, 95 (13), 137201.

104. M. Ali, P. Adie, C. H. Marrows, D. Greig, B. J. Hickey, and R. L. Stamps, Nat. Mater. 6, 70 (2006).

105. P. J. van der Zaag, R.M.Wolf, A. R. Ball, C. Bordel, L. F. Feiner, and R. Jungblut, J. Magn. Magn.Mater.148, 346 (1995).

106. W. C. Cain and M. H. Kryder, J. Appl. Phys. 67, 5722 (1990).

107. T. Maity, S. Goswami, D. Bhattacharya, and S. Roy, Phys. Rev. Lett.110, 107201 (2013).

108. J. Nogues and I. K. Schuller, J. Magn. Magn.Mater.192, 203 (1999).

109. J. Saha and R. H. Victora, Phys. Rev. B 76, 100405(R) (2007).

110. T. Maity, S. Goswami, D. Bhattacharya, G. C. Das, and S. Roy, J. Appl. Phys. 113, 17D916 (2013).

111. J. Saha and R. H. Victora, Phys. Rev. B 76, 100405(R) (2007).

112. B. M. Wang, Y. Liu, P. Ren, B. Xia, K. B. Ruan, J. B. Yi, J. Ding, X. G. Li, and L. Wang, Phys. Rev. Lett. 106, 077203 (2011).

113. H. Ahmadvand, H. Salamati, P. Kameli, A. Poddar, M. Acet, and K. Zakeri, J. Phys. D 43, 245002 (2010).

114. M. Ali, P. Adie, C. H. Marrows, D. Greig, B. J. Hickey, and R. L. Stamps, Nat. Mater. 6, 70 (2007).

115. S. Goswami, D. Bhattacharya, and P. Choudhury, J. Appl. Phys.109, 07D737 (2011).

116. B. Ramachandran and M. S. Ramachandra Rao, Appl. Phys. Lett. 95, 142505 (2009).

117. S. T. Zhang, M. H. Lu, D. Wu, Y. F. Chen, and N. D. Ming, Appl. Phys. Lett. 87, 262907 (2005).

118. J. Nogues, C. Leighton, and I. K. Schuller, Phys. Rev. B 61, 1315 (2000).

119. J. A. Mydosh, J. Magn. Magn.Mater.157-158, 606 (1996).

120. K. De, M. Thakur, A. Manna, and S. Giri, J. Appl. Phys. 99, 013908 (2006).

121. Manoj K. Singh, W. Prellier, M. P. Singh, Ram S. Katiyar, and J. F. Scott, Phys. Rev. B 77, 144403 (2008).

122. M. Sasaki, P. E. J̈onsson, H. Takayama, and H. Mamiya, Phys. Rev. B 71, 104405 (2005).

123. X. Chen, S. Bedanta, O. Petracic, W. Kleemann, S. Sahoo, S. Cardoso, and P. P. Freitas, Phys. Rev. B 72, 214436(2005).

124. D. Paccard, C. Schlenker, O. Massenet, R. Montmory, and A. Yelon, Phys. Status Solidi 16, 301 (1966).

125. S. K. Mishra, F. Radu, H. A. Durr, andW. Eberhardt, Phys. Rev. Lett. 102, 177208 (2009).

126. R. H. Kodama, A. E. Berkowitz, E. J. McNiff Jr., and S. Foner, Phys. Rev. Lett. 77, 394 (1996).

127. M. J. Benitez, O. Petracic, E. L. Salabas, F. Radu, H. Tuysuz, F. Schuth, andH. Zabel,Phys. Rev. Lett. 101, 097206 (2008).

128. J. L. Tholence and R. Tournier, J. Phys. (Paris) Colloq. 35, C4-229 (1974).

129. P. K. Manna, S. M. Yusuf, R. Shukla, and A. K. Tyagi, Appl. Phys. Lett. 96, 242508 (2010).

130. R. G. Calderon, J. C. G. Sal, and J. R. Iglesias, J. Magn. Magn.Mater.272–276, 701 (2004).

131. N. Marcano, J. C.G´omez Sal, J. I. Espeso, L. Fern´andezBarqu´ın, and C. Paulsen, Phys. Rev. B 76, 224419 (2007).

132. J. R. Iglesias, J. I. Espeso, N. Marcano, and J. C. G´omez Sal, Phys. Rev. B 79, 195128 (2009).

133. S. Seki, X. Z. Yu, S. Ishiwata, and Y. Tokura, Science 336, 198 (2012).

134. M. J. Benitez, O. Petracic, E. L. Salabas, F. Radu,H. Tuysuz, F. Schuth, and H. Zabel, Phys. Rev. Lett. 101, 097206 (2008)

135. B. Dieny, *J. Magn. Magn.Mater.*136, 335 (1994).

136. Nogues, J., Sort, J., Langlais, V., Skumryev, V., Surinach, S., Munoz, J.S., Baro, M.D.: Phys. Rep. 422, 65 (2005)

137. Radu, F., Nefedov, A., Grabis, J., Nowak, G., Bergmann, A.,Zabel, H.: J. Magn. Magn.Mater. 300, 206 (2006)

138. B. Altuncevahir and A. R. Koymen, J. Magn. Magn.Mater.261, 424 (2003).

139. X. Ke, M. S. Rzchowski, L. J. Belenky, and C. Eom, Appl. Phys. Lett. 84, 5458 (2004).

140. S. Chikazumi, Physics of Ferromagnetism: Oxford UniversityPress, New York, 1997.

141. S. Esho, Jpn. J. Appl. Phys., Suppl. 15, 93 (1976)

142. K. Takanashi, H. Kurokawa, and H. Fujimori, Appl. Phys. Lett. 63, 1585(1993)

143. Y. Z. Wu, G. S. Dong, and X. F. Jin, Phys. Rev. B 64, 214406 (2001).

144. S. M. Valvidares, L. M. Alvarez-Prado, J. I. Mart ın, and J. M. Alameda,Phys. Rev. B 64, 134423 (2001).

145. S. Demirtas, M. R. Hossu, M. Arikan, A. R. Koymen, and M. B. Salamon,Phys. Rev. B 76, 214430 (2007).

146. M. Ziese, I. Vrejoiu, and D. Hesse, Appl. Phys. Lett. 97, 052504 (2010).

147. M. C. dos Santos, J. Geshev, J. E. Schmidt, S. R. Teixeira, and L. G.Pereira, Phys. Rev. B 61, 1311 (2000).

148. Y. J. Nam and S. H. Lim, Appl. Phys. Lett. 99, 092503 (2011).

149. J. Geshev, A. D. C. Viegas, and J. E. Schmidt, J. Appl. Phys. 84, 1488(1998).

150. J. Y. Park and M. G. Allen, J. Micromech. Microeng.8:307–316(1998).

151. A. L. Patterson, Phys. Rev. 56:978 (1989).

152. M. J. Carey and A. E. Berkowitz, Appl. Phys. Lett. 60, 3060 (1992)